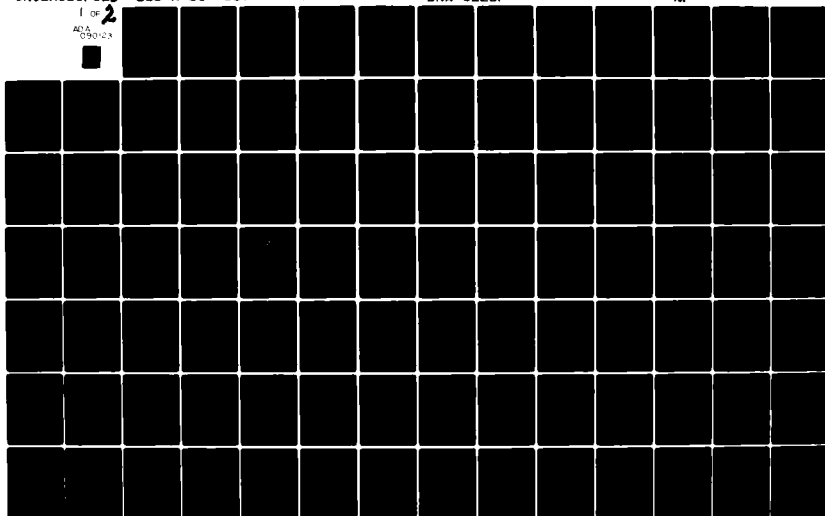AD-A090 123   SYSTEMS SCIENCE AND SOFTWARE LA JOLLA CA   F/G 14/2
                DEVELOPMENT OF AIRBLAST AND SOIL STRENGTH INSTRUMENTATION.(U)
                FEB 80 P L COLEMAN, M A GROETHE   DNA001-78-C-0244
UNCLASSIFIED   SSS-R-80-4367   DNA-5225F   NL

1 OF 2

AD A
090123

DNA 5225F

DEVELOPMENT OF AIRBLAST AND SOIL STRENGTH INSTRUMENTATION

Systems, Science and Software
P.O. Box 1620
La Jolla, California 92038

1 February 1980

Final Report for Period 1 May 1978—1 January 1980

CONTRACT No. DNA 001-78-C-0244

APPROVED FOR PUBLIC RELEASE;
DISTRIBUTION UNLIMITED.

Prepared for
Director
DEFENSE NUCLEAR AGENCY
Washington, D. C. 20305

80 10 10 085

Destroy this report when it is no longer
needed. Do not return to sender.

SECURITY CLASSIFICATION OF THIS PAGE (When Data Entered)

REPORT DOCUMENTATION PAGE	READ INSTRUCTIONS BEFORE COMPLETING FORM

1. REPORT NUMBER	2. GOVT ACCESSION NO.	3. RECIPIENT'S CATALOG NUMBER
DNA 5225F	AD-A090 123	

4. TITLE (and Subtitle)	5. TYPE OF REPORT & PERIOD COVERED
DEVELOPMENT OF AIRBLAST AND SOIL STRENGTH INSTRUMENTATION	Final Report for Period 1 May 78—1 Jan 80
	6. PERFORMING ORG. REPORT NUMBER SSS-R-80-4367

7. AUTHOR(s)	8. CONTRACT OR GRANT NUMBER(s)
P. L. Coleman M. A. Groethe	DNA 001-78-C-0244

9. PERFORMING ORGANIZATION NAME AND ADDRESS	10. PROGRAM ELEMENT, PROJECT, TASK AREA & WORK UNIT NUMBERS
Systems, Science and Software P. O. Box 1620 La Jolla, California 92038	SUBTASK H11CAXSX352-81

11. CONTROLLING OFFICE NAME AND ADDRESS	12. REPORT DATE
Director Defense Nuclear Agency Washington, D. C. 20305	1 February 1980
	13. NUMBER OF PAGES 122

14. MONITORING AGENCY NAME & ADDRESS(If different from Controlling Office)	15. SECURITY CLASS. (of this report)
	UNCLASSIFIED
	15a. DECLASSIFICATION/DOWNGRADING SCHEDULE

16. DISTRIBUTION STATEMENT (of this Report)

Approved for public release; distribution unlimited.

17. DISTRIBUTION STATEMENT (of the abstract entered in Block 20, if different from Report)

18. SUPPLEMENTARY NOTES

This work sponsored by the Defense Nuclear Agency under RDT&E RMSS Code B344078462 H11CAXSX35281 H2590D.

19. KEY WORDS (Continue on reverse side if necessary and identify by block number)

Airblast Instrumentation   stagnation pressure
soil strength gauge   dynamic cone penetrator
drag sphere   shock tube
dynamic pressure gauge   heat flux sensor
bar gauge

20. ABSTRACT (Continue on reverse side if necessary and identify by block number)

The development and testing of airblast and soil strength gauges are presented. The airblast sensors include an accelerometer instrumented drag sphere to measure dynamic pressure and bar gauge probes to measure static, stagnation amd reflected pressures at levels to 10^8 Pa (1 kilobar). The soil strength gauge is a shock hardened dynamic cone penetrator. An analysis of a slug type heat flux sensor is given.

DD FORM 1473   EDITION OF 1 NOV 65 IS OBSOLETE

PREFACE

We appreciate the assistance of Ed Day and Warren Ginn with the design and preparation of the soil strength gauge. L. Prasser, F. Peterson, J. Hofmann and R. Castanos all contributed to successful completion of the gauge development tests.

TABLE OF CONTENTS

LIST OF ILLUSTRATIONS

LIST OF ILLUSTRATIONS (CONT'D)

LIST OF ILLUSTRATIONS (CONT'D)

LIST OF ILLUSTRATIONS (CONT'D)

SUMMARY OF CONVERSION FACTORS   (U.S. to Metric Units)
AND PREFIXES

To convert from	To	Multiply by
mils	millimeters	0.0254
inches	centimeters	2.54
feet	meters	0.3048
miles	kilometers	1.6093
square inches	square centimeters	6.4516
square feet	square meters	0.0929
cubic inches	cubic centimeters	16.38706
cubic feet	cubic meters	0.0283
gallons (U.S.)	liters	3.785
ounces	grams	28.349
pounds	kilograms	0.454
pounds per square inch, psi	newtons per square centimeter	0.6894757
pounds per cubic inch	kilograms per cubic centimeter	27,679.90
pounds per square foot	newtons per square meter	47.88026
inches per second	centimeters per second	2.54
Fahrenheit degrees	Celsius degrees or Kelvins[a]	5/9
kilotons	terajoules (10^{12} Joules)	4.183

[a]To obtain Celsius (C) temperature readings from Fahrenheit (F) readings, use C = (5/9) (F − 32). To obtain Kelvin (K) readings, use K = (5/9)(F − 32) + 273.15.

$1 \text{ Pa} = 1 \frac{N}{m^2}$

$1 \text{ Bar} = 10^5 \text{ Pa} = 14.5 \text{ psi}$

$1 \text{ psi} = 6.9 \text{ RPa}$

$1 \text{ g} = \text{Acceleration of gravity} = 32 \text{ F/S}^2 = 9.8 \text{ m/s}^2$

PREFIXES: $G = 10^9$ = giga $M = 10^6$ = mega

$K = 10^3$ = kilo $c = 10^{-2}$ = centi

$\mu = 10^{-6}$ = micro $n = 10^{-9}$ = nano

SECTION I
INTRODUCTION AND SUMMARY

During 1978 and 1979, Systems, Science and Software (S^3), under contract to the Defense Nuclear Agency (DNA), pursued the analysis, development and testing of several instrument concepts. Our objective was improved measurement systems for underground nuclear tests in cavities and high explosive (HE) cratering experiments.

In Section 2, we describe continued efforts to develop an instrumented drag sphere to measure dynamic pressure in the supersonic flow of an airblast. The HE driven shock tubes used to test the spheres were significantly improved. By the use of a complex internal structure, shock induced oscillations of the sphere can be partially damped and hence the internal accelerometer is not overranged or driven into its resonance.

In Section 3 we describe some new approaches to the measurement of static, stagnation and reflected pressure in a strong blast wave. Initial shock tube experiments identified a number of problems in the gauge designs. There are several possible improvements that could be implemented in the future to give field worthy instruments.

Section 4 is concerned with a technique to measure soil strength during a HE cratering shot. The objective would be to detect changes in strength due to passage of the ground shock but before significant cratering motion appears. A series of small scale HE tests showed that a strength gauge could be constructed and fielded in ground shock environments of roughly 1000 g's (10^4 m/s^2) acceleration and 5 to 10 MPa (50 to 100 bar) peak stress. Additional work is needed to establish the accuracy of the strength data and to refine the design for field use.

8

Finally, in Section 5 we consider improvements in a thermal radiation sensor. Our objective was to find new materials suitable for use in the instrument to simplify its construction and to establish ways to improve the response time for thermal transients.

SECTION II
CONTINUED DEVELOPMENT OF A DYNAMIC PRESSURE SENSOR

2.1 INTRODUCTION

For supersonic flow in a strong airblast, the drag force on a sphere, F_D, is directly proportional to the dynamic pressure, $1/2 \rho_1 u_1^2$, of the flow where ρ_1 is the density of the gas behind the shock front and u_1 is the flow velocity. In a previous report (Kratz, Coleman and Wilson, 1978)[1], we discussed our initial efforts to develop an accelerometer-instrumented sphere as a dynamic pressure gauge. While some encouraging results were achieved, two problems were dominant. First, our test bed for evaluating the spheres was inadequate as a calibration facility, i.e., the true dynamic pressure of the flow was poorly known. Second, the incidence of the shock front on the sphere introduced severe oscillations of the sphere; the acceleration due to the oscillations was comparable to that due to the drag force.

Our work reported below made significant progress in solving these problems. In Section 2.2 we describe the high explosive (HE) driven shock tubes that now provide good quality one-dimensional(1D) planar shocks. In the balance of Section 2 we discuss several different internal designs for the sphere which served to partially damp the shock induced oscillations and to partially isolate the accelerometer from the residual vibrations of the sphere.

2.2 IMPROVEMENTS IN THE TEST BED

The shock tubes (Figure 1) consisted of several meter lengths of 0.305 m diameter "Burke" tube (a heavy cardboard cylinder used for concrete construction forms) buried under a meter or more of soil. At one end was an explosive charge mounted on a heavy (12.7 mm thick) steel plate (to improve confinement of the HE product gases). The other end was open

10

Det Line

12.7mm Thick Steel Plate

C4 Charge

1" Concrete
Backfill
Around
HE and
Tube

Range
From HE

9.7mm Copper Plate
(Tests 2, 3, 4)

1 of 5 Pin Probes (TOA)

305mm Dia. Burke Tube

Buried
Under
1 Meter
of Soil

TOA

Sphere Under Test
1 of 2

1 of 2
Static
Side-Wall
Bar Gauges

TOA

TOA

Air at Ambient

TOA
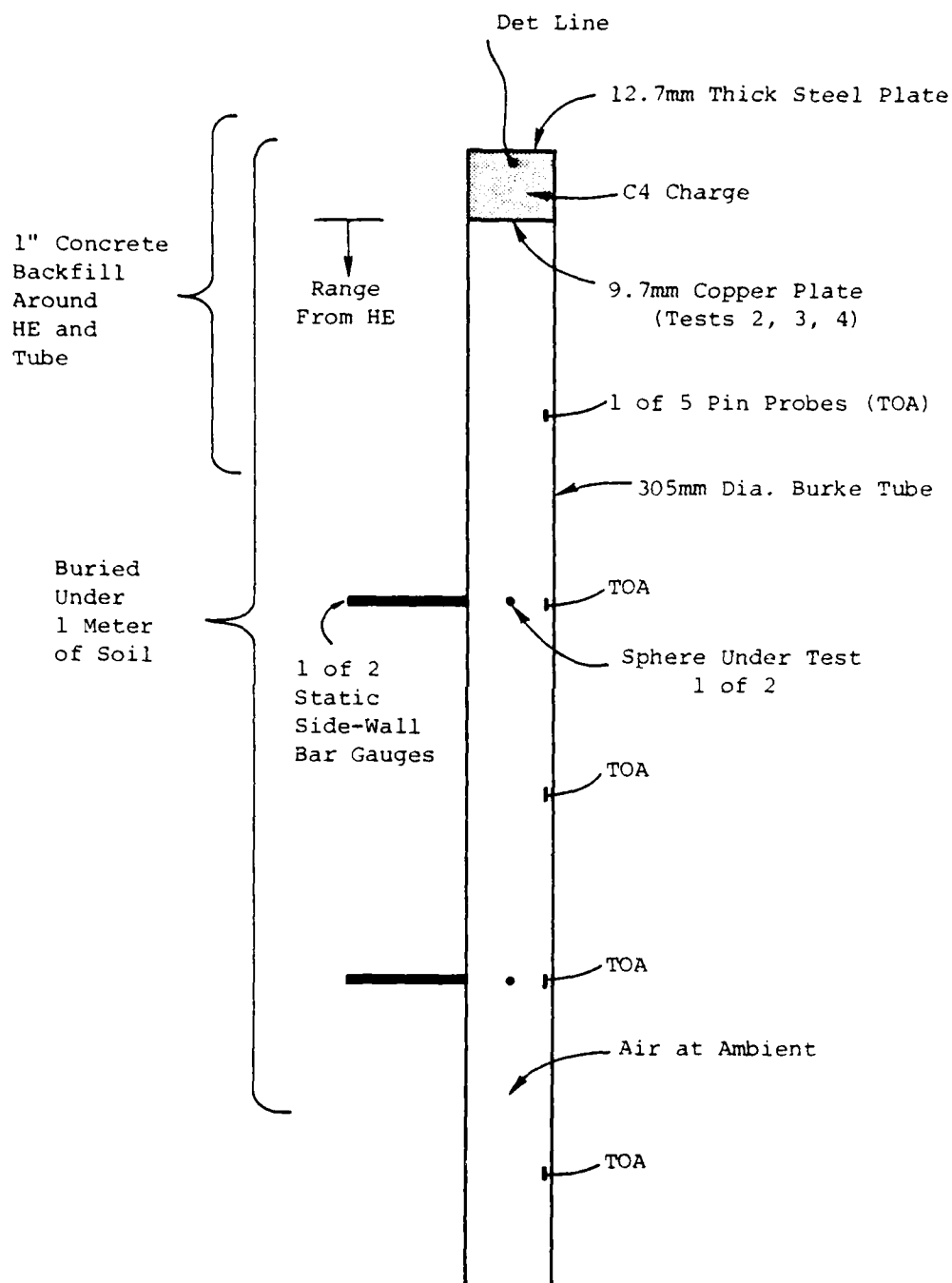
Figure 1.   Schematic plan view of shock tube test bed.

11

to the atmosphere. For our previous work, we used small
amounts of explosive (0.045 to 0.089 kilograms); we observed
significant deceleration of the shock front and decay of the
peak static pressure as the shock propaged along the tube:

$$X \propto t^{0.8}$$
$$P_{max} \propto X^{-0.8} \tag{1}$$

where X is the shock front position at time t and P_{max} is the
peak static pressure. This behavior is more nearly character-
istic of a blast front due to a delta-function deposition of
energy by the HE rather than of a shock tube driven by a con-
stant power input. In the latter case, the shock velocity,
static pressure and dynamic pressure are all constant. Since
there are no suitable reference transducers for dynamic pres-
sure, we must rely on static pressure measurements (from gauges
along the tube walls) and the usual strong shock relations

$$P_D \equiv 1/2 \ \rho_1 u_1^2 = \left(\frac{\rho_1}{\rho_0} - 1\right) \frac{(P_s - P_0)}{2} \tag{2}$$

$(P_D$ = dynamic pressure
P_s = static pressure
P_0 = ambient pressure
ρ_0 = ambient density of air)

to derive the actual dynamic pressure experienced by the
spheres under test. Thus our objective was to achieve a
behavior more like that of a conventional shock tube driven
by a reservior of high pressure gas. To that end, we increased
the quantity of explosive to over 17 kg and improved the lateral
and back end confinement of the HE.

For the four shots conducted on this project, we used
PZT pin probes at five positions along the tube to establish
the shock front motion, and two bar gauges (Blackstock, Feeney
and Kratz, 1956) [2] with quartz crystal sensors in the side walls

12

to monitor the static pressure profile. Table 1 summarizes
the results from these tests and Figures 2 through 5 show the
bar gauge records. The C4 charges were 12 inches in diameter,
6 to 9 inches long, and detonated at a single point on the
back surface of the cylindrical charge. The shock times of
arrival over the distance range 1 to 4 meters (3 to 5.5 m for
test 4) were fitted very well by a power law relation. From
this relation for each test, we derived the shock velocity
(∿5 mm/μs for test 1 and ∿3 mm/μ⌐ for tests 2,3 and 4). Then
with the usual relations for strong shocks and the ambient air
density for each test, we calculated the static and dynamic
pressures at the shock front. Table 1 compares the calculated
static pressures with the values given by the bar gauges.
Within the uncertainties in the data, there is good agreement.*

The first test gave a reasonably uniform shock but the
peak pressures (∿250 bars static and over 1 kbar dynamic) were
several times larger than desired. Thus for the subsequent
tests, we placed a 9.7 mm thick copper plate in contact with
the front surface of the HE to reduce the shock strength.
Using the Gurney relations (Gurney, 1943[3] and Kennedy, 1973[4]
we predicted a velocity of about 2.5 mm/μs for the copper
plate. This should also be the particle velocity behind the
shock front; the associated shock velocity is 2.9 mm/μs and
the expected static pressure is about 85 bars. We estimate
that within the first 90 mm of its motion (an interval of
about 40 μs), the plate was accelerated to within 95% of its
expected final velocity.

The bar gauge records merit some consideration. For
the first three tests, the 6.35 mm diameter steel bars were
152.4 mm long (input bar) corresponding to an acoustic delay

_____

*We note that the arrival times are quite consistent with a
constant shock velocity. This implies a constant shock front
pressure which is also consistent (within experimental un-
certainties) with the pressure measurements.

TABLE 1. SUMMARY OF SHOCK TUBE EXPERIMENTS

Test	Charge Length m	Mass. kg	TOA Fit $X(m) = f(t, \mu s)$	Range m	Peak Static Pressure (Bar) Calc	Observed at First Arriv.
1	0.15	17.3	$0.0102t^{0.90}$	1.5 3.0	290 248	300 ± 30 260 ± 30
2	0.23	26.0	$0.0059t^{0.90}$	1.5 3.0	101 88	80 ± 20 120 ± 20
3	0.23	26.0	$0.0069t^{0.89}$	1.5 3.0	108 91	100 ± 20 *
4	0.23	26.0	$0.0050t^{0.93}$	3.5 5.0	83 78	110 ± 10 90 ± 10

*Gauge failed.

14
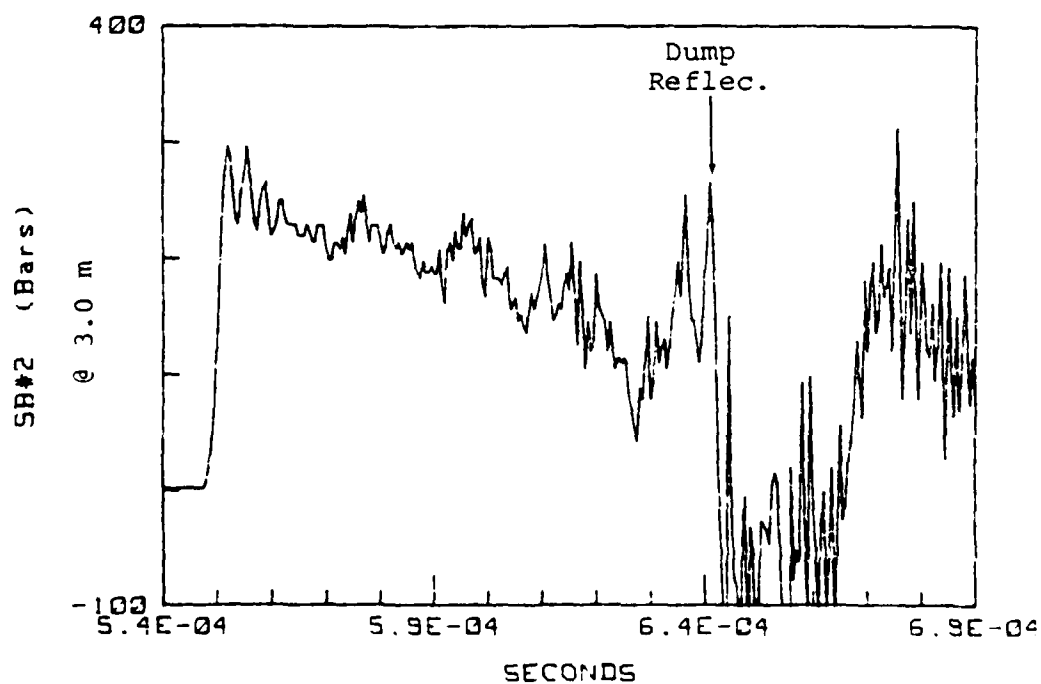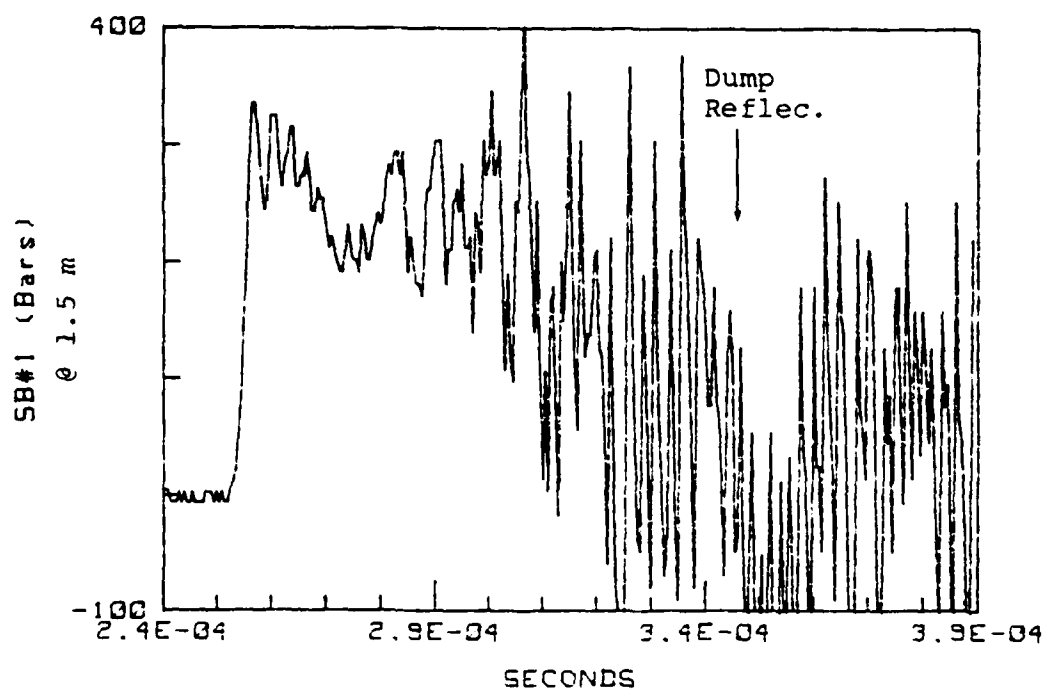
Figure 2. Bar gauge records of static pressure for
shock tube test 1. (All time scales for bar
gauges have been corrected for the input bar
delay.)

15
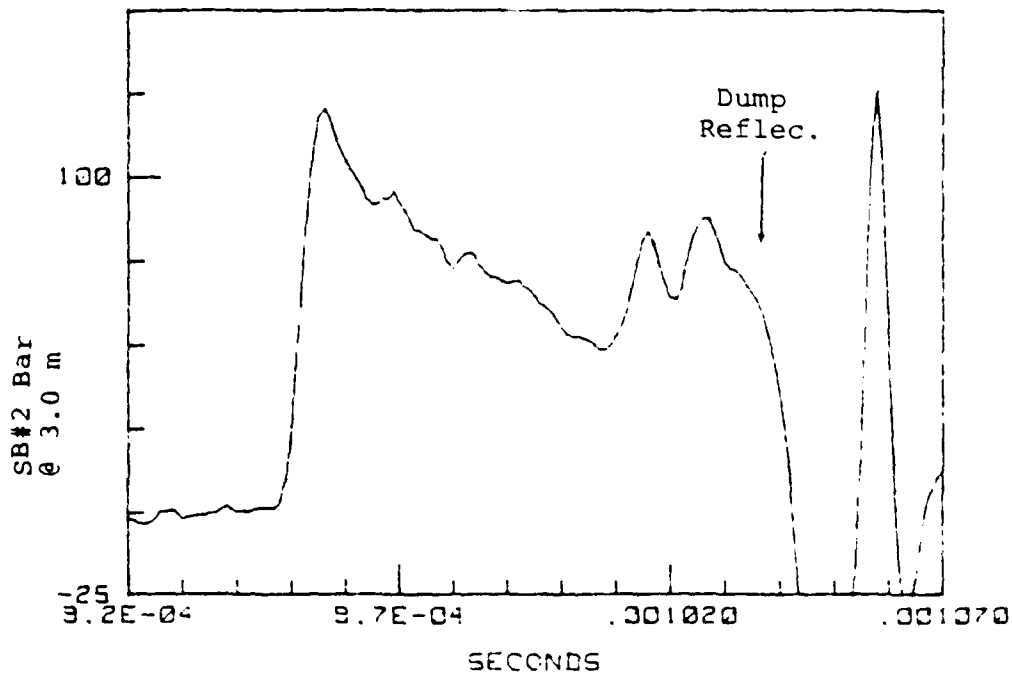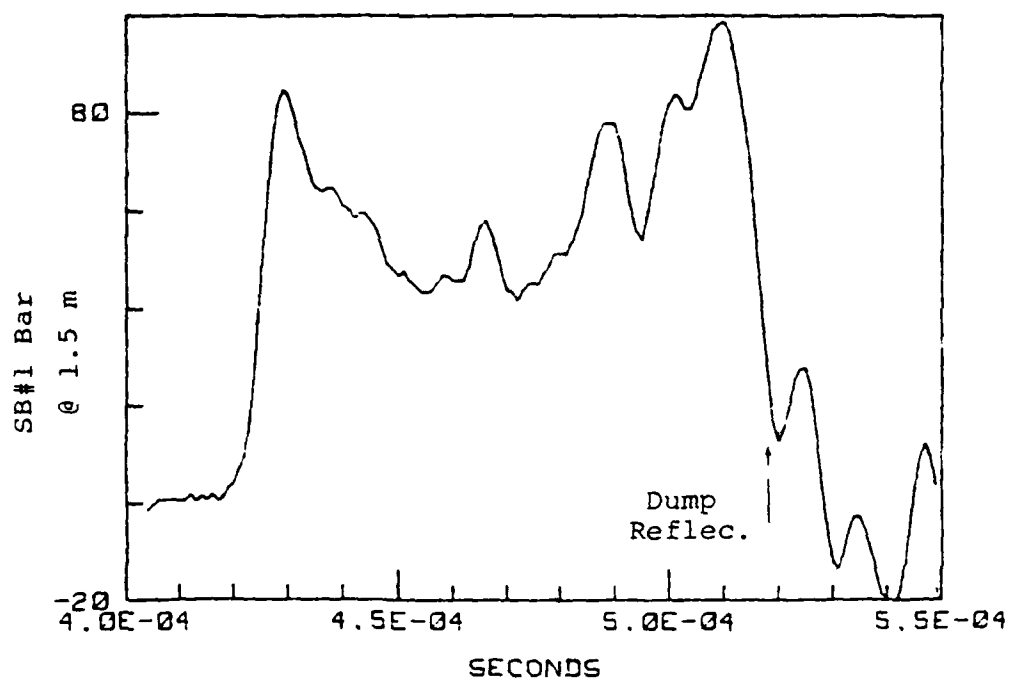
Figure 3.   Bar gauge records of static pressure for
shock tube test 2.   (FM tape playbacks.)

16
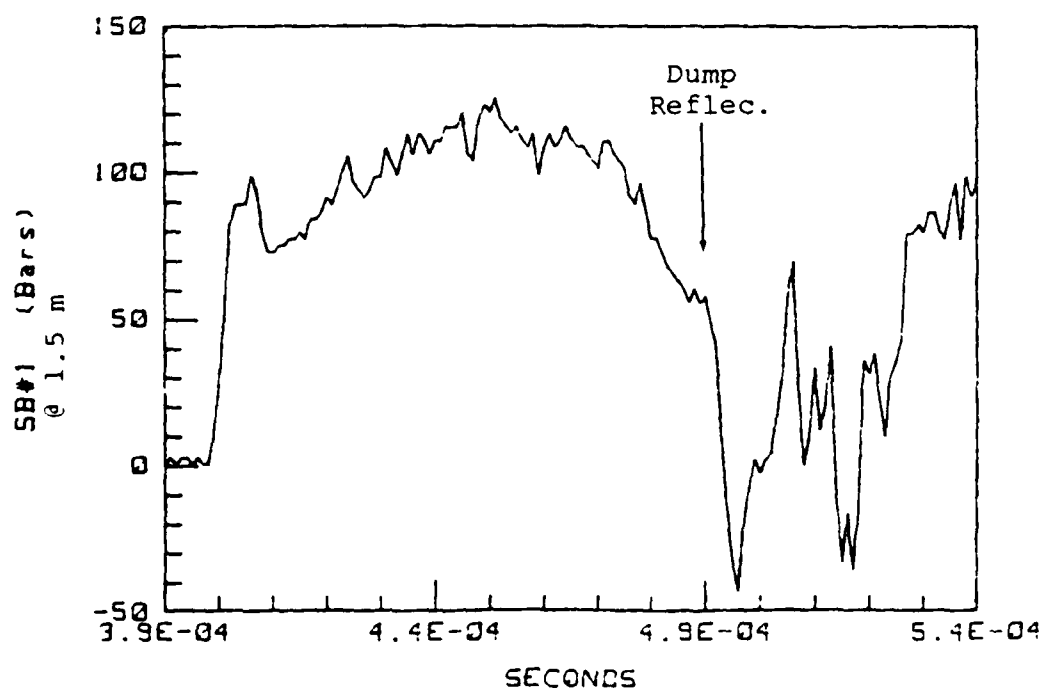
Figure 4.   Bar gauge record of static pressure for
shock tube test 3.
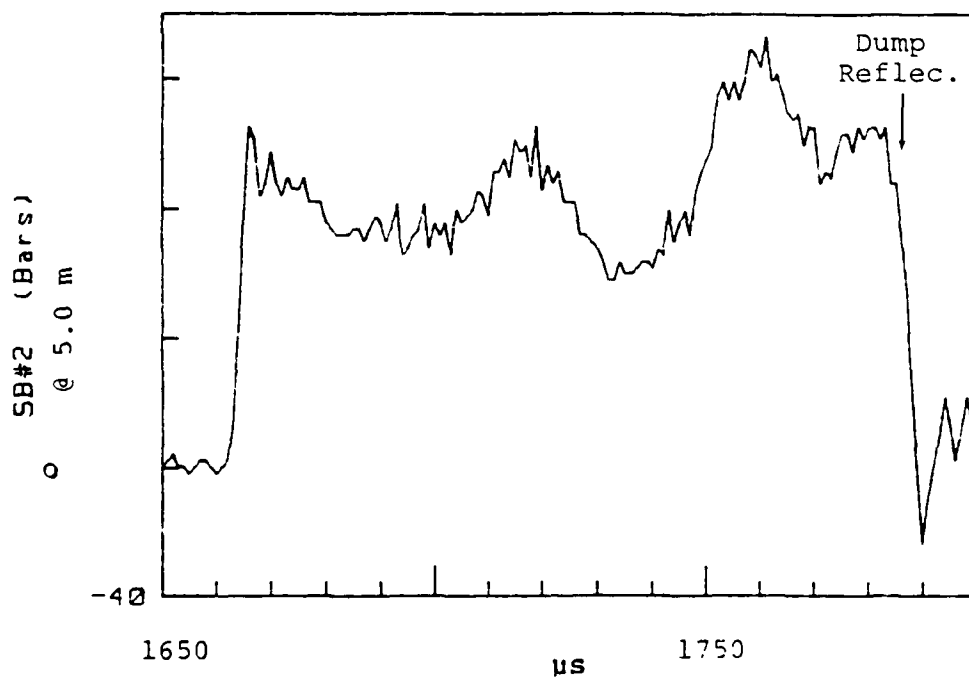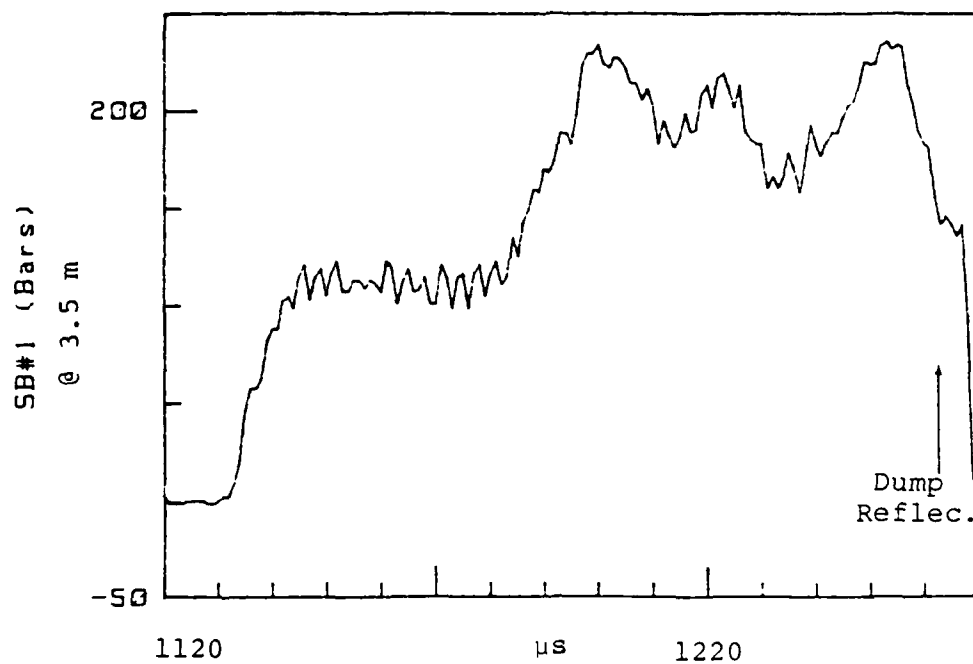
Figure 5. Bar gauge records of static pressure for shock tube test 4.

of 31 μs and 228.6 mm long (dump bar) which gives a useful
pressure measuring time of 93 μs after shock arrival. For
the fourth test, the gauges had 254 mm long dump bars, giving
measuring times of 124 μs. The initial ringing in the signal
after shock arrival was due to the response of the bar to the
sharp shock front (Coleman, 1979)[5]*.

On the first test, both gauges showed a factor of two
decrease in pressure during the first hundred microseconds
after shock arrival. The severe ringing after 30 μs in the
gauge at 1.5 m (SB-1) may have been associated with the arriv-
al of the contact surface and failure of the gauge. On the
second test, the static pressure initially decayed behind the
shock front but then appeared to be increasing at the end of
the measuring interval. The cause of this increase is not
clear. On the third test, the pressure remained fairly con-
stant after the shock passed; unfortunately the second gauge
at a range of 3.0 m failed preshot. For the fourth test, the
pressure also seemed to have been constant behind the shock;
the record for the first gauge (SB-1 at 3.0 m range) is not
reliable because of the long risetime at shock arrival and
the input bar reflection artifact which appeared after
590 μs.

Overall, the relative constancy of shock velocity and
peak static pressure are the best indications that the shock
tube performed well. In particular, we will use the strong
shock relations to estimate the magnitude and relative con-
stancy of the flow (i.e., dynamic pressure) behind the shock
front.

---

*For the second test, we had to rely on the backup FM tape
 records (80 kHz nominal bandwidth) for the bar gauge data.
 Thus the few microsecond ringing characteristic of the bar
 is not evident.

2.3 SPHERE DEVELOPMENT

Our earlier work identified the accelerometer's response to the blast-induced sphere oscillations as the major gauge problem. Our initial approach to that problem was to isolate the accelerometer from the sphere. We fabricated steel "shells" of outer radius 28.6 mm and inner radius 14.3 mm. Within the inner volume the accelerometer was embedded in a vibration attenuating medium. The total mass of the assembled sphere was 0.66 kg. See Figure 6.

Our first choice for that medium was RTV rubber, Dow Corning 3120 with catalyst S. This selection was based on the relatively high density (1.5g/cm^3), modulus, and strength (~40 bars in tension) of the RTV. In particular we were concerned that the accelerometer (an Endevco model 2264A-50KR with a mass of 1.5 grams, average density of $\sim3.4 \text{ g/cm}^3$ and $\sim1 \text{ cm}^2$ base area) not move relative to the sphere during the shock induced motion of the sphere.

For initial testing of each gauge design, we monitored the accelerometer signal while the suspended sphere was impacted by a hammer. Such a collision may be roughly modelled as the collision of two elastic spheres. From an analytical treatment of this impact by Hertz in 1881 (see Love, 1927[6] page 198), we may estimate the duration of the impact τ and the force at the contact point of the spheres, F, as

$$\tau \sim 2.94 \ \alpha_{max}/v \qquad (3)$$

and

$$F = k\alpha^{3/2} \qquad (4)$$

where α_{max} = maximum value of α,

α = relative displacement of the centers of the spheres
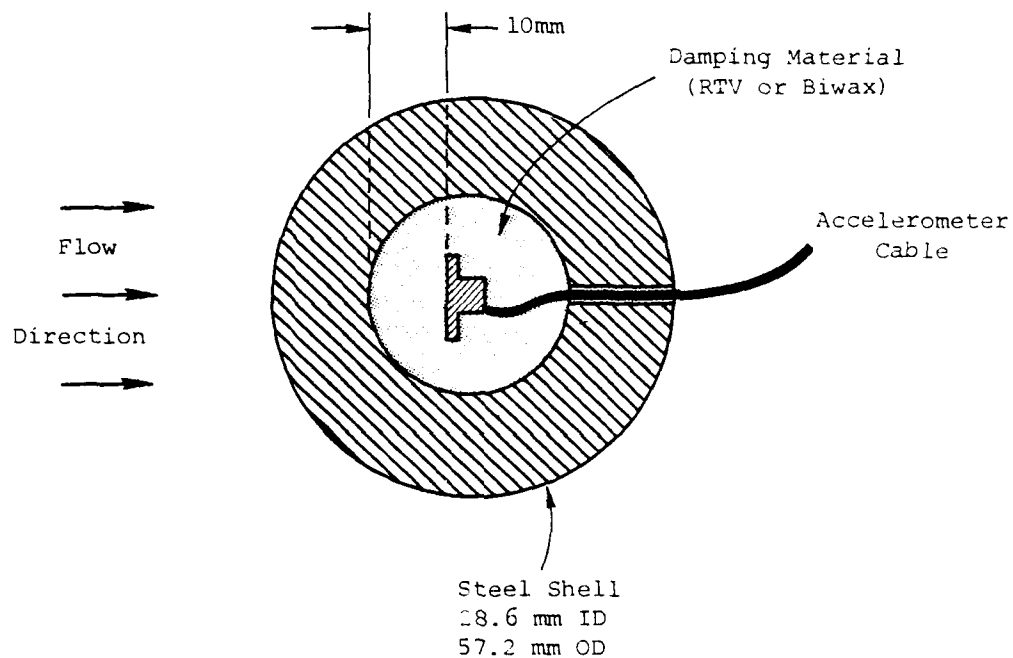
Figure 6.   Internal design of sphere for initial lab tests
            (RTV and Biwax) and for shock tube test 1 (Biwax
            damping).   (All accelerometers used were Endevco
            2264A-50KR.)

$$v = \text{velocity of impact}$$

$$k \equiv \frac{4}{3\pi} \left(\frac{r_1 r_2}{r_1 + r_2} \right)^{1/2} \frac{1}{(I_1 + I_2)} \tag{5}$$

$$r_i \equiv \text{radius of sphere } (i = 1 \text{ or } 2)$$

$$I_i \equiv (1 - \nu_i)^2 / (\pi c_i^2 \rho_i (1 - 2\nu_i)) \tag{6}$$

$$\nu_i \equiv \text{Poisson's ratio for material } i$$

$$c_i = \text{compressional velocity in material } i$$

$$\rho_i = \text{density of material } i$$

$$m_i = \text{mass of sphere } i$$

For spheres made of the same metal, the maximum value of force, F_{max}, is

$$F_{max} = k\alpha_{max}^{3/2} = g \, v^{6/5} \, m^{3/5} \, r^{1/5} \, I^{-2/5} \tag{7}$$

where $\alpha_{max} = h \, v^{4/5} \, m^{2/5} \, r^{-1/5} \, I^{2/5}$ (8)

The numerical constants g and h depend on the relative sizes of the spheres. If the spheres are identical,

$$\begin{array}{ll} g = 0.35 & \left. \begin{array}{l} m_1 = m_2 \\ r_1 = r_2 \end{array} \right\} \end{array} \tag{9}$$

and if one sphere is very large

$$\begin{array}{ll} g = 0.61 & \left. \begin{array}{l} m_2, \ r_2, \ \to \infty \end{array} \right\} \\ h = 2.0 & \end{array} \tag{10}$$

For steel, the material constant I is $1/(5.2 \times 10" \text{ Pa})$. As an example, if two identical spheres of radius 28.6 mm impact at 1 m/s, the expected contact duration is 200 μs and the peak acceleration would be 9×10^3 m/s^2; for impact of the sphere on a large steel plate, the duration is 220 μs and the peak acceleration of the sphere is 1.6×10^4 m/s^2.

Our initial lab tests with the new design of Figure 6 were disappointing. Unfortunately, the exceptional elasticity and ultrasonic transmission of this RTV made it a poor choice for this application. As Figure 7 shows, a few tens of microseconds after the impact test began, the accelerometer signal showed severe ringing to peaks about $\pm 10^5$ m/s^2 at a dominant frequency of about 220 kHz. This frequency is characteristic of some modes of the steel sphere and also of the accelerometer's natural resonance. (The Fourier spectrum of the waveform is given in Figure 8).

As a more suitable damping material, we tried a polyurethane foam* around the accelerometer. Figure 9 and 10 demonstrate the much cleaner response of the foam damped sphere to the laboratory test impacts. The duration, amplitude and wave symmetry are plausible in terms of the impact theory given above. The phase of negative acceleration is probably an indication of some relative motion of the accelerometer with respect to the sphere.

Two spheres with Biwax damping were tested in the first shock tube. Figure 11 shows the installation technique. They were located at ranges of 1.5 and 3.0 meters from the front surface of the HE. Based on the TOA data for shock front velocity, we calculate peak dynamic pressures of 126 MPa and 104 MPa for the two spheres respectively; the corresponding accelerations are 4.6 x 10^5 m/s^2 and 3.8 x 10^5 m/s^2 respectively.

---

* The foam is Biwax 601 available from Biwax Corp., Des Plaines, Illinois. The mean density is 1.01 g/cm^3; unconfined compressive strength exceeds 30 bars (3 x 10^6 Pa); the Young's modulus is of order 1 kbar (10^8 Pa). Waterways Experiment Station (Day, 1978)[7] personnel use this material to fill and water seal ground motion gauge canisters.
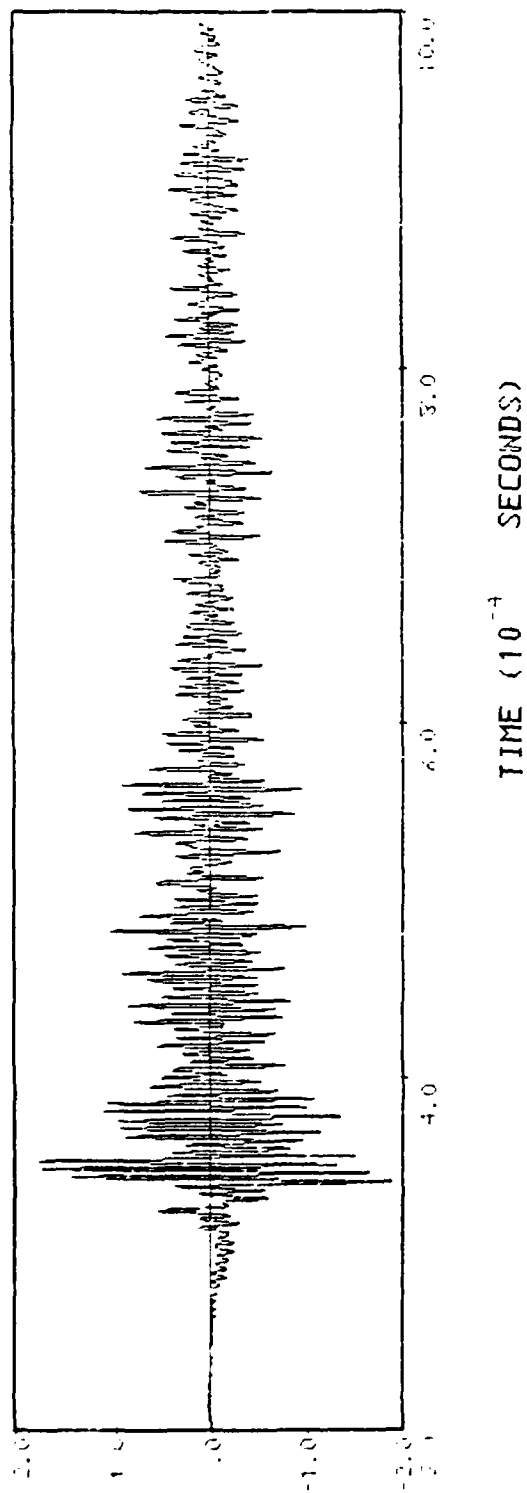
Figure 7. Example of lab test of sphere with RTV "damping" material. (Units of kilo "G's" = 10^4 m/s^2).

TIME (10^{-4} SECONDS)

FREQUENCY (10⁻¹ HERTZ)
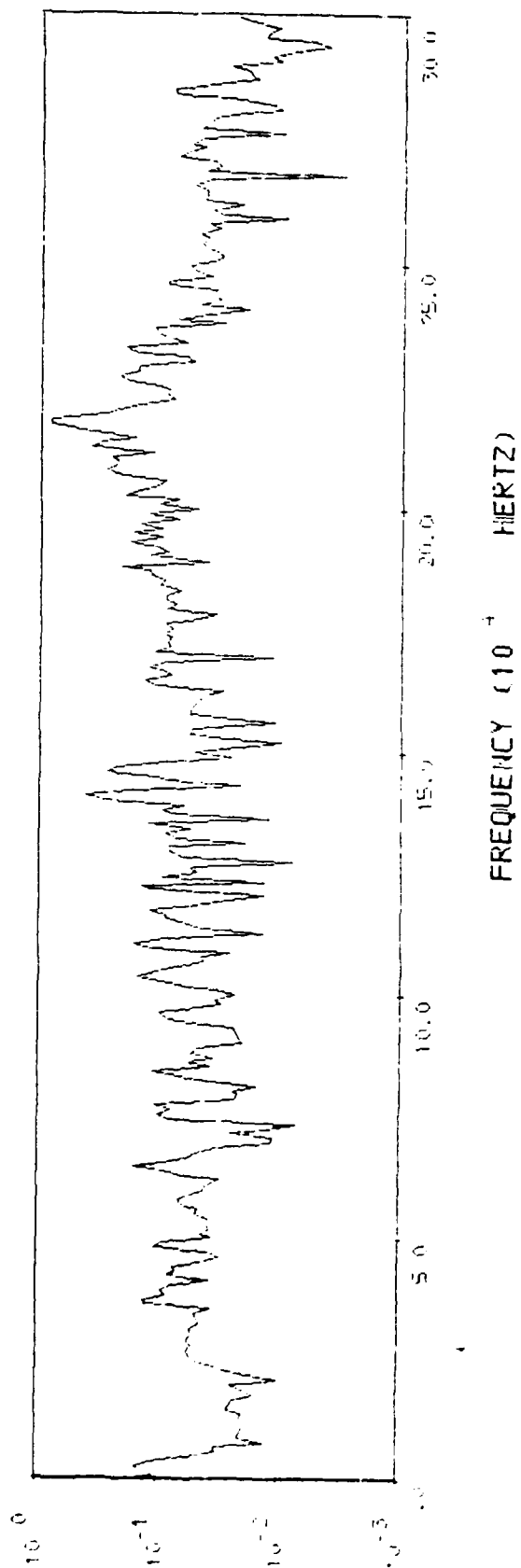
Figure 8. Fourier amplitude spectrum for lab test of RTV "damped" sphere. (G/Hz).

25

TIME (10⁻⁴ SECONDS)
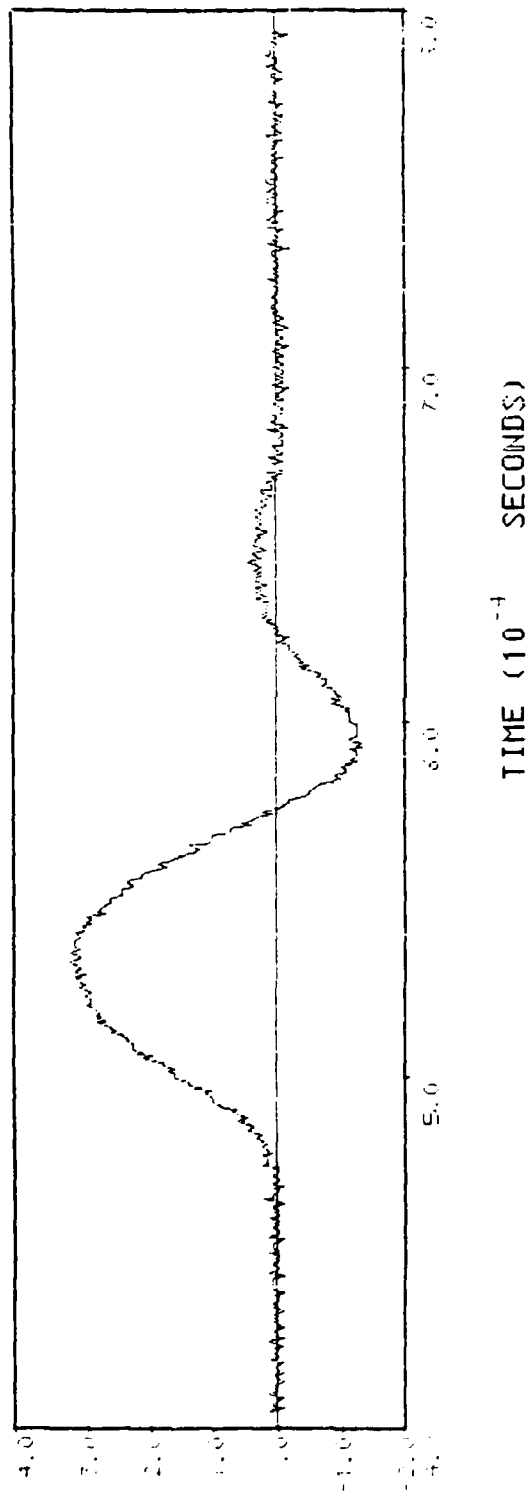
Figure 9. Example of lab test of Biwax damped sphere. (Units of kilo "G's").

FREQUENCY (10⁻¹ HERTZ)
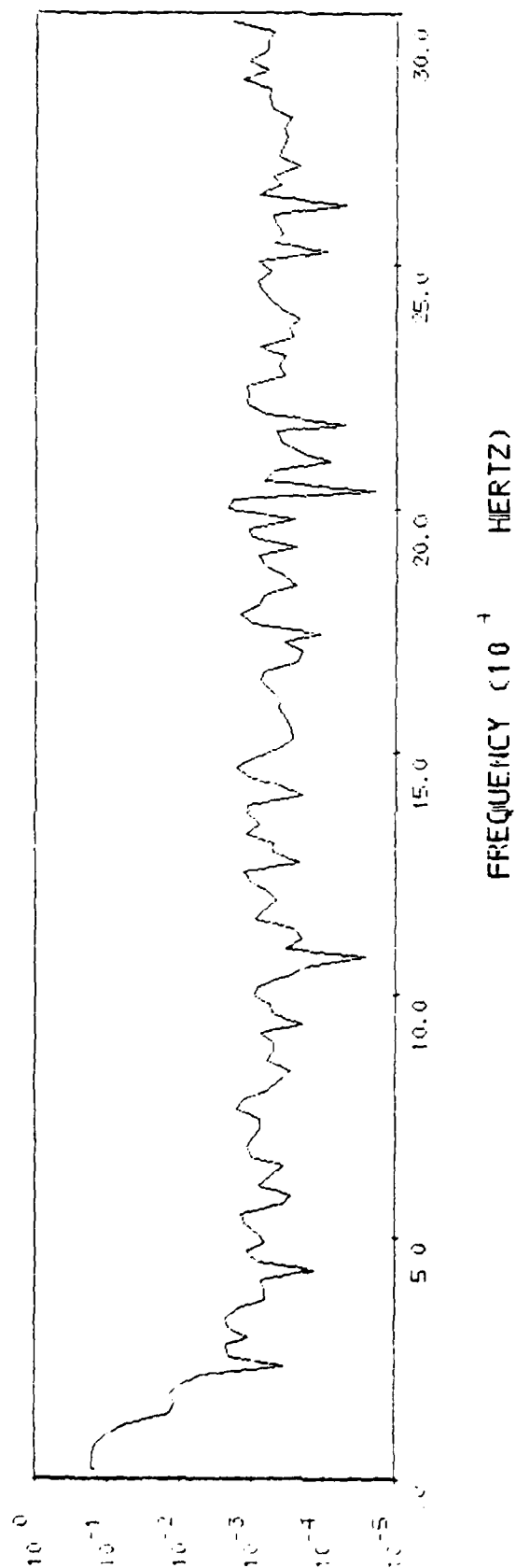
Figure 10. Fourier amplitude spectrum of lab test of Biwax damped sphere. (G/Hz).

27
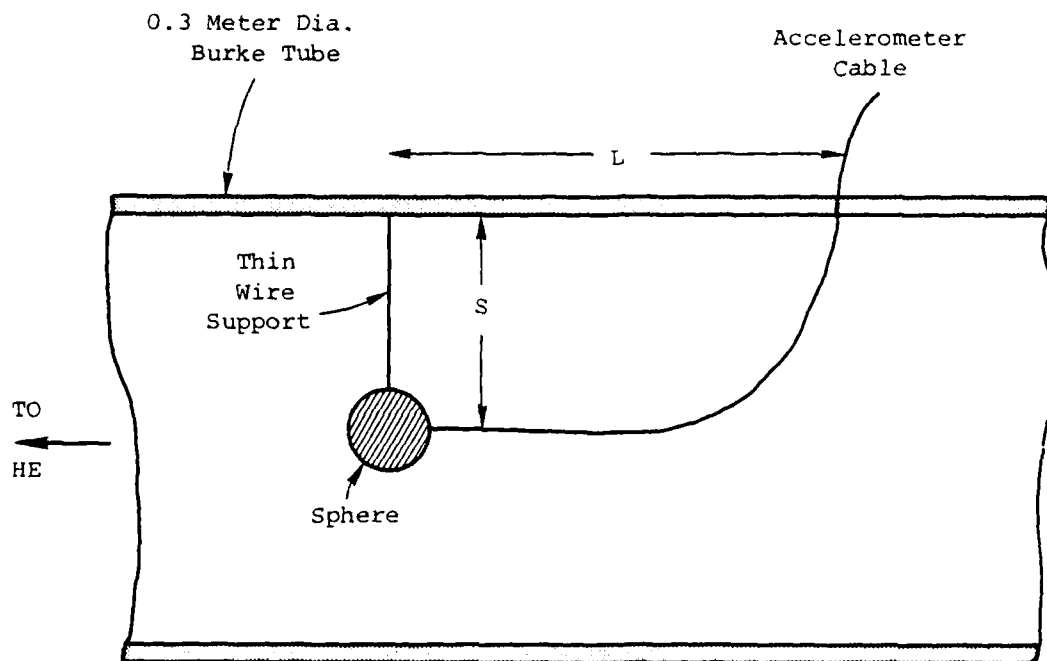
Figure 11. Mounting details of sphere in shock tube.
(S = 0.15m except 0.10m for test 2; L = 0.30m
for test 1, 0.46m for test 2, 0.61m for test 4).

Our observed initial peak accelerations, Figure 12 and 13, are lower and have risetimes of 15 to 20 μs. The latter feature may have been due to the damping material in which the accelerometers were embedded. Combined with decay of the dynamic pressure behind the shock (at a rate several times that of the static pressure, e.g., a 1/e time of order 40 to 50 μs) this may explain the initial low response of our gauges.

A very obvious ringing at ∿210 kHz (4.7 μs period) appears in the first sphere's signal at about 295 μs. This could be due to either oscillation of the sphere at one of its natural frequencies and/or the resonance of the accelerometer. (Failure of the accelerometer or cable occurs with a signal level of 3.5×10^5 m/s^2 at 330 μs. The unprotected accelerometer cable entered the wall of the shock tube at a range of 1.80 m.) The shock front arrived at that point at about 314 μs.) The calculated flow velocity at 1.5 m is 4.75 mm/μs. Thus we would expect arrival of the contact surface at roughly 290 μs. If no early venting of HE products occurred, the mean density of the HE gases was about 150 kg/m^3 (0.15 g/cm^3) and the shocked air's density was 11 kg/m^3. Using these numbers, we would estimate a dynamic pressure of 1.7 GPa (17 kbar) associated with the contact surface. Hence after 290 μs, we would expect that our dynamic pressure probe was seriously overranged and the ringing may reflect this condition.

The signal from the second sphere is not so easy to interpret. After the initial peak at 575 μs, the record decreases to 1.4×10^5 m/s^2 at 580 μs, increases again to 5.6×10^5 m/s^2 at 596 μs, a possible failure is evident at 598 μs, and the record continues to oscillate about 4×10^5 m/s^2 until a complete failure at 632 μs. Ringing of the sphere is not obvious. For this gauge, we estimate a contact surface arriving at about 625 μs with a dynamic pressure of order 0.7 GPa (7 kbar) and arrival of the shock front at the cable of 615 μs.
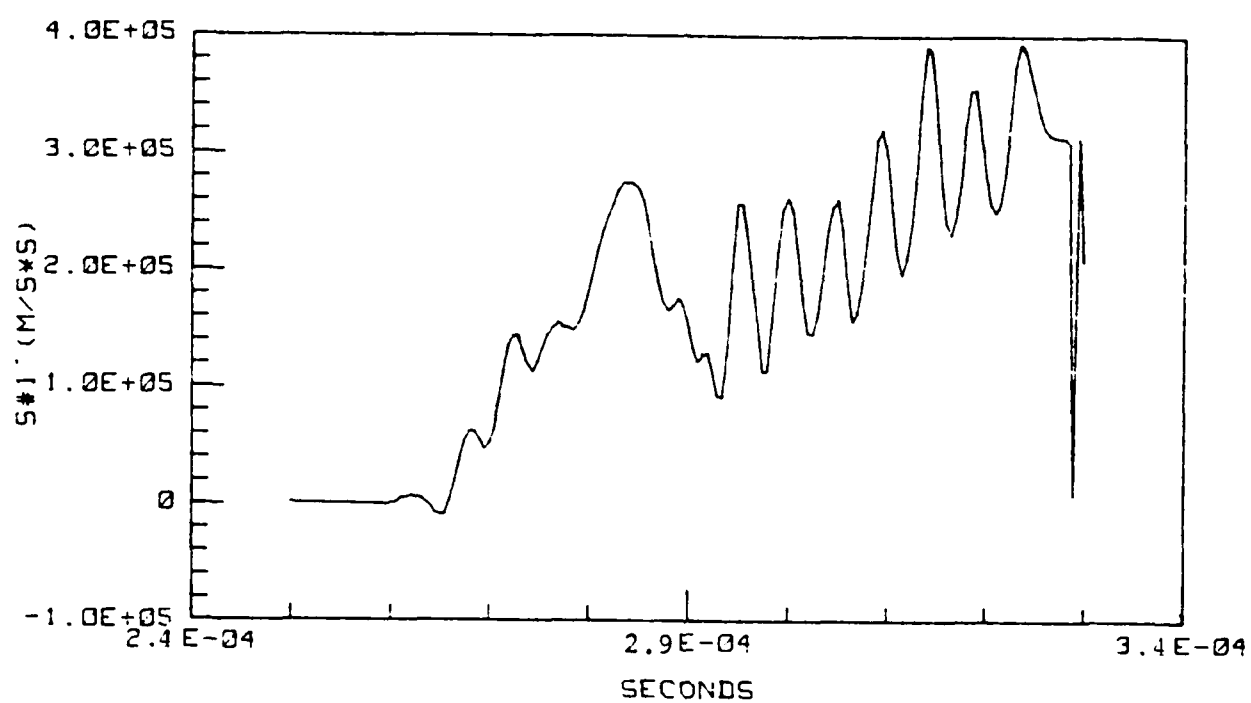
Figure 12.   Accelerometer signal for sphere at 1.5 m on
             shock tube test 1.
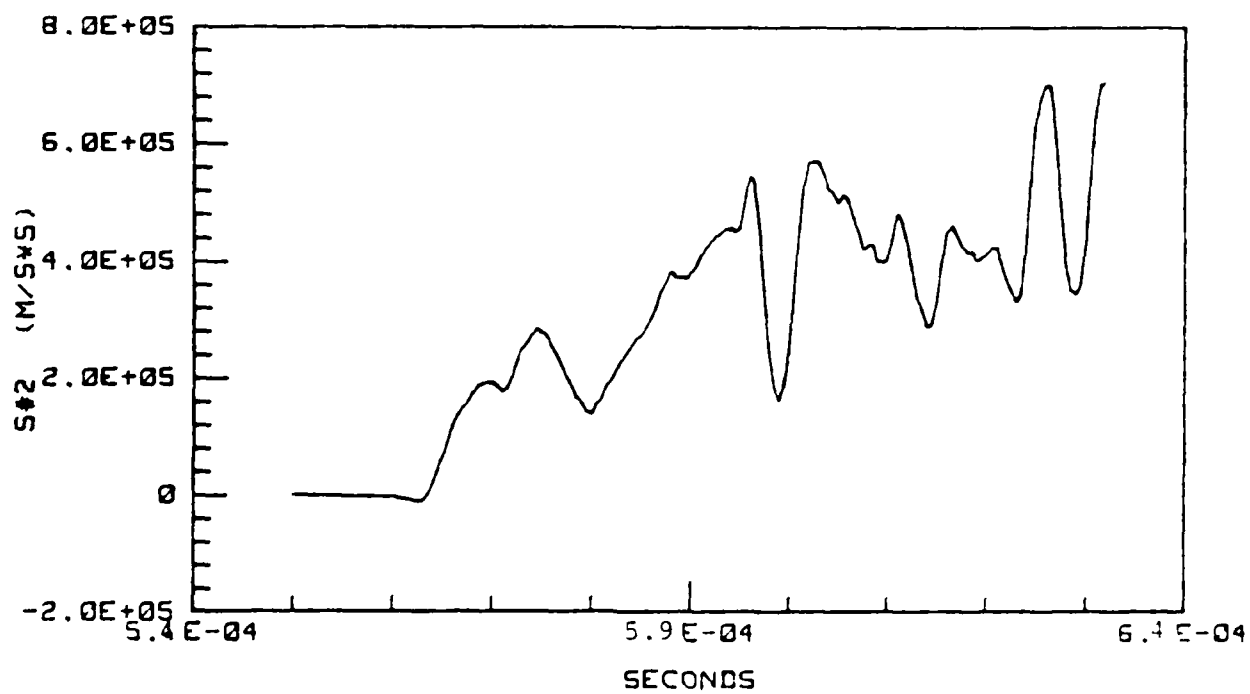
Figure 13.   Accelerometer signal for sphere at
              3.0m on shock tube test 1.

Because the spheres are intended for use at the fractional kilobar (dynamic pressure) level, our subsequent experiments used a "Gurney" plate (as described in Section 2.2) on the HE to reduce the shock strength. In addition, we reduced the amount of damping material under the accelerometer base (Figure 14) in the sphere in an effort to improve the gauge's response time. Figure 15 shows the acceleration signal for the test sphere on the second shock tube shot. Unfortunately a number of problems in the recording system left us with only the initial 40 µs of the data. However it is clear that the amount of foam isolating the accelerometer from the sphere was inadequate and severe ringing at a frequency of 0.2 MHz is evident. Based on the TOA data, we expected a dynamic pressure of 28 MPa (equivalent to 1.0×10^5 m/s^2 acceleration) at this gauge. The observed mean is twice as large and the peak excursions exceed ±100 MPa.

Our approach to the gauge design had been to isolate the accelerometer from the natural ringing of the sphere. The success of that approach was low. Thus we began an investigation of ways to damp the oscillations of the sphere.

5mm

Biwax

Flow

Direction

Accelerometer
Cable

Steel Sphere, 57.2 mm OD
With Cylindrical Cavity
for Accelerometer
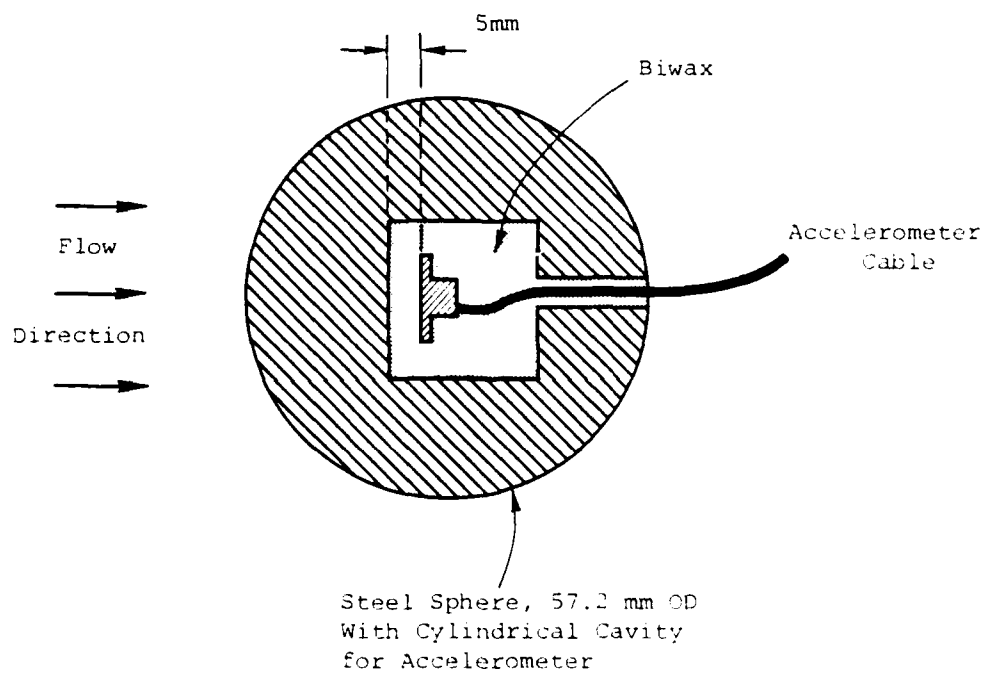
Figure 14.   Internal design of sphere for shock
tube test 2.
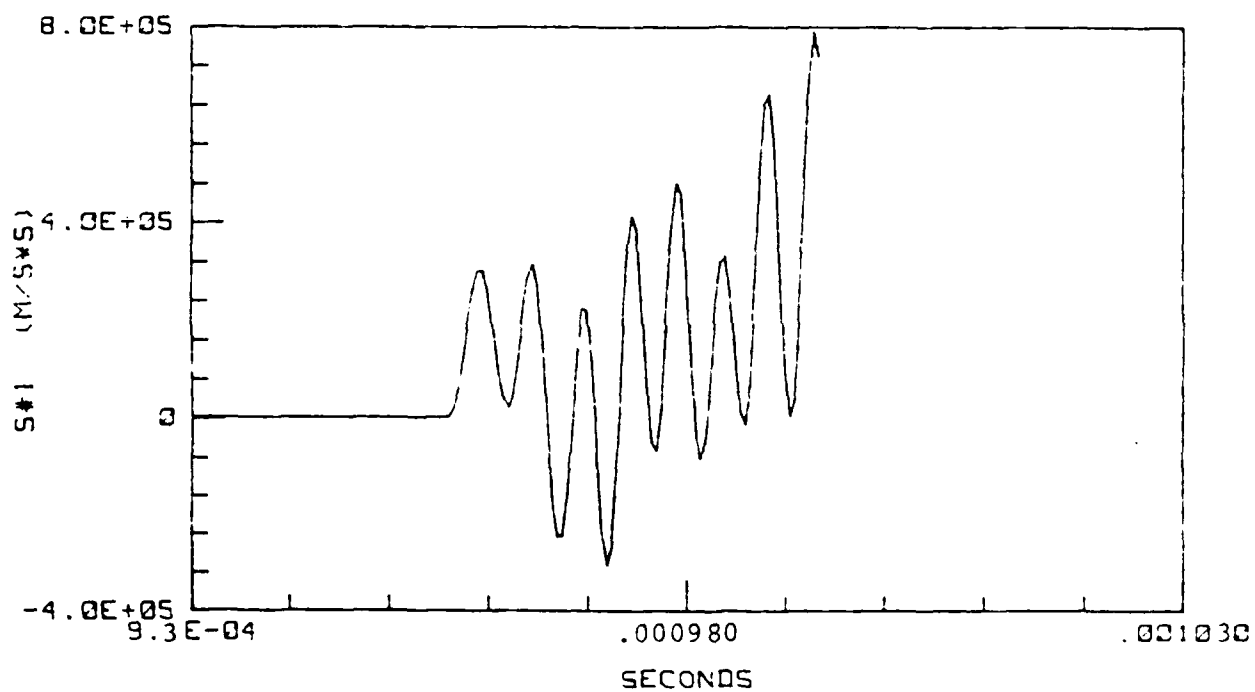
Figure 15.   Accelerometer signal for sphere at
3.0m range on shock tube shot 2.

2.4 DAMPING OF THE SPHERE'S OSCILLATIONS

If the accelerometer were very small in size, it could be located at the exact center of the sphere where the motions due to various modes of oscillation have a node. However, the finite size of the accelerometer ($\sim$10 mm) means that it can respond to both radial and angular displacements associated with the sphere's ringing. In order to damp the oscillations, it is necessary to attenuate the acoustic waves as they propagate through the sphere. Thus, we began a review of the sound attenuation properties of materials.

The scientific literature and commercially available products emphasize the frequency range of 0.1 to 10 kHz which is relevant for noise control around people. For most materials, the acoustic attenuation rate (per unit length of material) is dependent on the ambient temperature, the frequency, the amplitude of the wave, and its type (shear or compressional). (See Ungar and Hatch, 1961[8]; Jones, 1972[9].) A few papers have considered the sonic transmission properties of polymers between 0.1 and 1 MHz. Generally, the attenuation increases with frequency. (See Ivey, et al., 1949[10], and Auberger and Rinehart, 1961[11].) Nakamura, 1963[12] reported an absorption coefficient for polystyrene of

$$x(\text{nepers/cm}) \sim 7 \times 10^{-5} \, f^{1.4} \tag{11}$$

where 1 neper* is 8.7 db and f is in kHz. At 400 kHz, McSkimin and Andreatch, 1971[13] measured 0.07 neper/cm for lucite (PMMA) and 0.6 neper/cm for epoxy foam. Folds, 1972[14] observed 0.2 neper/cm for polypropylene and low density polyethylene at 599 kHz and suggested that the attenuation rate increases with the thermal coefficient of sound velocity. The available data

---

*One neper corresponds to an attenuation by a factor of e.

suggest that at the 100 kHz range of interest to us, "good" materials like polypropylene may offer absorption coefficients of up to 2 db/cm.

Because of the low modulus and strength of polymers, it would be impractical to have sufficient path length within the sphere to utilize the absorption effect; i.e., the whole sphere cannot be constructed from polypropylene, etc. Thus, we turned to a relatively complex internal structure for the gauge. A variety of materials were used to take advantage of acoustic mismatches at boundaries. The initial configuration is shown in Figure 16.

The accelerometer was mounted to a lead disk [speed of sound 1.1 km/s, density 1.13×10^4 kg/m^3 (11.3 g/cm^3)]. Underneath the lead disk and between the hemispheres, we used a sheet of 1.3 mm thick sound damping material*. The top and sides of the accelerometer were surrounded by Biwax foam. The hemispheres were connected together with steel screws.

Figure 17 shows a typical record for a laboratory impact test for this configuration. Clearly, the result is quite unsatisfactory. The dominant late-time resonance at about 23 kHz disappears if nylon screws are used between the hemispheres; however, severe ringing above 100 kHz remains. The use of aluminum for the back hemisphere and GRS rubber or cork in place of the "DYAD" led to no significant changes. Improvements did occur if (1) the back hemisphere was split in half (on a diameter) and cork or rubber sheet placed between the halves; (2) slots were milled into the front hemisphere and filled with the Biwax foam; (3) many small holes were drilled into the front half from its equatorial plane and filled with Biwax; and (4) the lead disk was fully surrounded by cork or rubber and thus has no direct metal-to-metal contact with hemispheres. The influence of all these changes is demonstrated in Figure 18, which compares typical lab tests for two configurations.

---

*"DYAD 606," Soundcoat Co., Brooklyn, NY. This material is most effective at acoustic frequencies.

0.05" Thick Sound Dampening Sheet

Hole for Support Wire

Biwax

Flow

Accelerometer
Cable

Direction

Steel Front
Hemisphere,
2.25" Dia.
with Cavity
for Lead Disk

Accelerometer

Steel Back
Hemisphere
With 0.875" Dia x
0.5" Cavity for
Biwax and
Accelerometer

Lead Disk,
1.25" Dia. x 0.375"
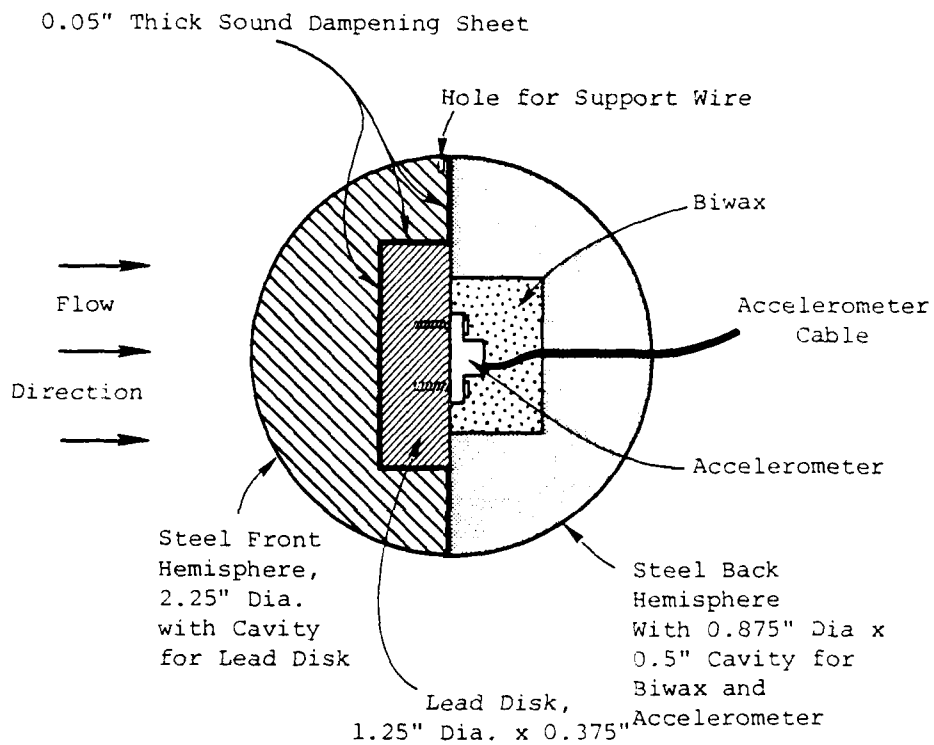
Figure 16.   Internal design for "composite" sphere.
            (Section view in plane parallel to flow.)

37
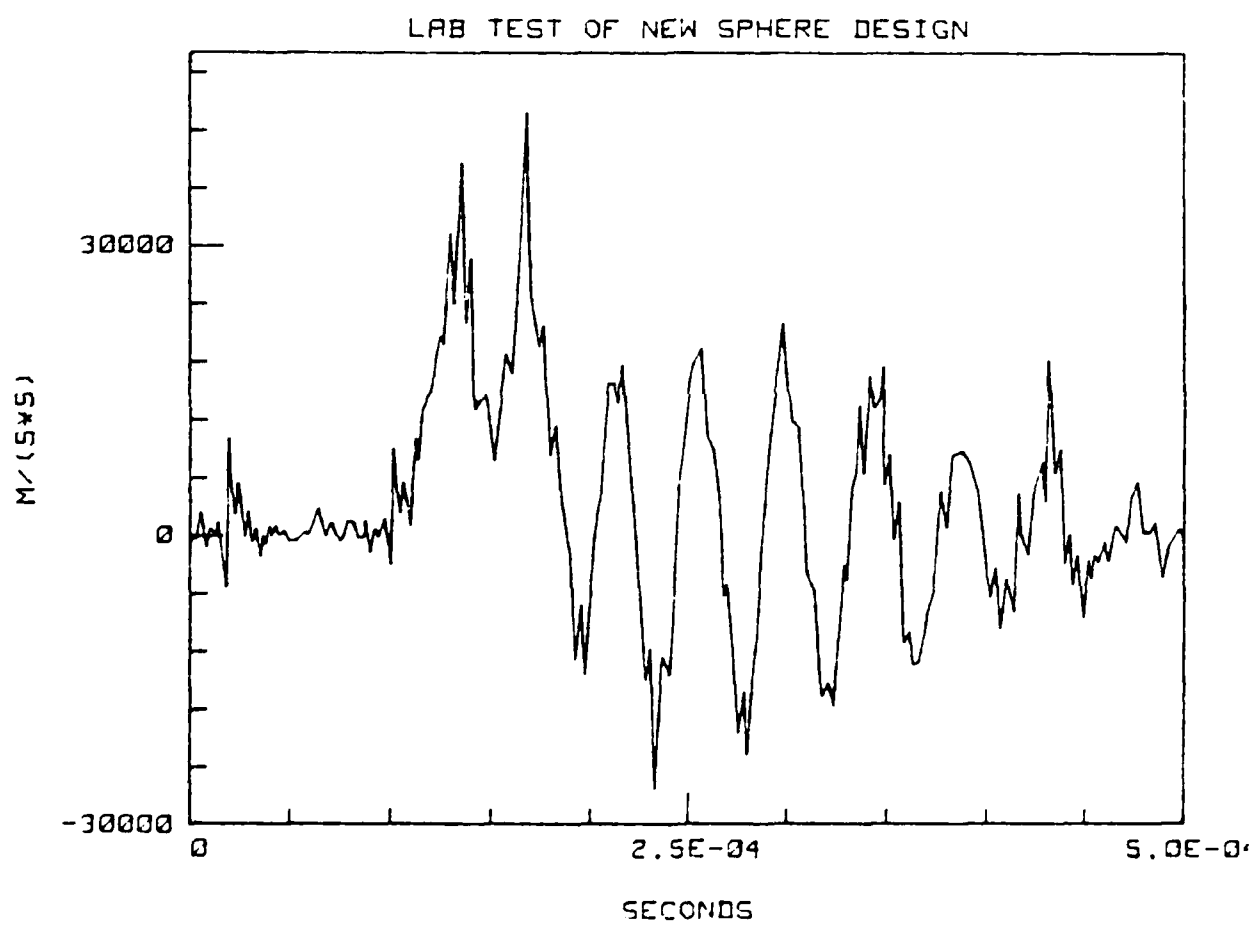
Figure 17.   Example of lab test of sphere with initial
             composite interior design.
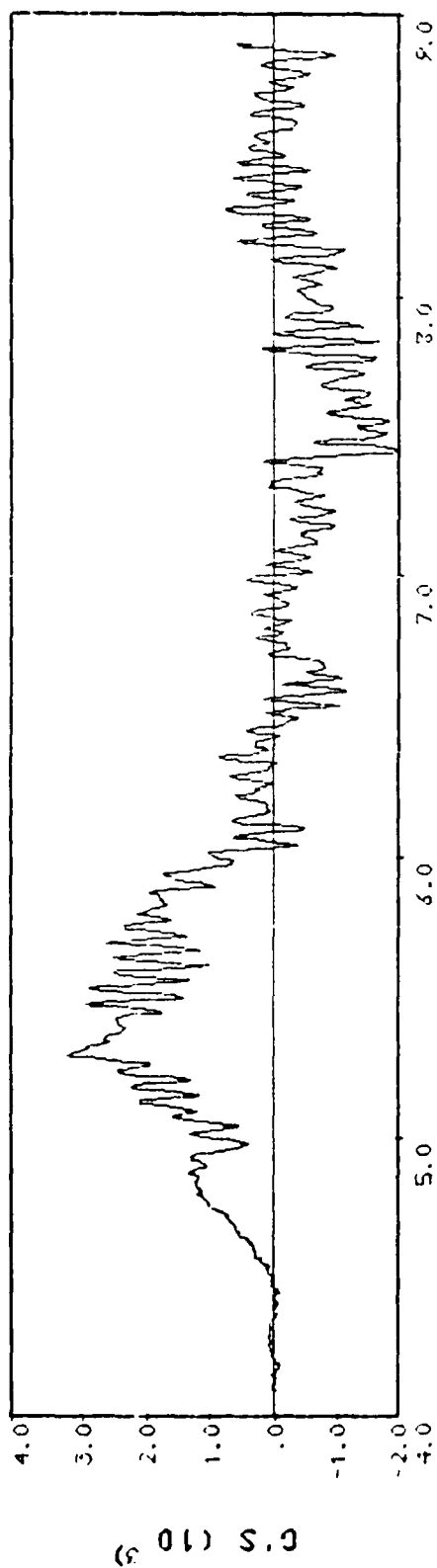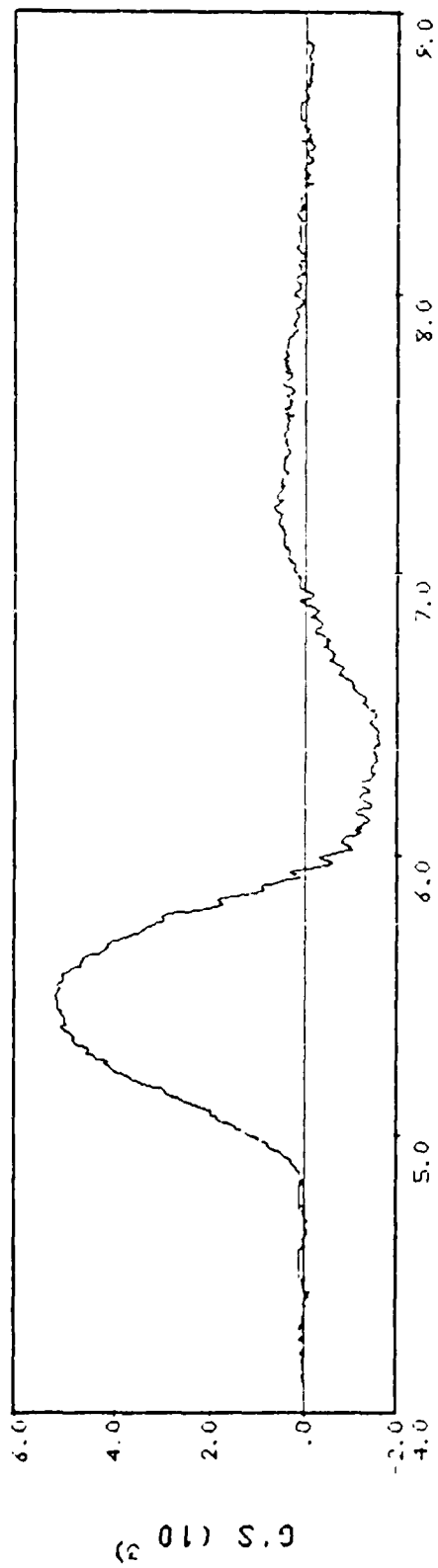
Figure 18. Examples of lab tests of spheres. Top: Design per figure 16 with aluminum back hemisphere. Bottom: Design per figure 19.

Figure 19 shows the final design of the spheres. Two such gauges were prepared for the fourth shock tube experiment. Lab impact tests for each sphere are shown in Figure 20, and Figure 21 compares the Fourier spectra of the lab tests.

The raw data records for the fourth experiment are shown in Figures 22 and 23. For sphere No. 1 at a range of 3.5 m*, ringing at a frequency of 195 kHz is almost immediately evident but not extreme in magnitude. The mean peak acceleration of about 2.2×10^5 m/s^2 corresponds to a dynamic pressure of 310 bars (31 MPa) for the 0.35 kg mass spheres. The dynamic pressure predicted by the TOA data is 26 MPa. This 20 percent discrepancy does not seem serious in view of the simplified assumption of steady flow around the sphere (discussed below) and the fact that the measured static pressures are also 15 to 25 percent higher than predicted** (Table I). Severe ringing with a peak-to-peak amplitude of over 6×10^5 m/s^2 begins at 1287 usec. This probably represents arrival of the contact surface, i.e., the copper "Gurney" plate. An estimate for contact arrival from the TOA data and strong shock relations is 1.3 ms.

For sphere No. 2 at a range of 5.0 m, ringing at 191 kHz is more significant but not fatal to the accelerometer. The peak (mean) acceleration is also 2.2×10^5 m/s^2, equivalent to 31 MPa dynamic pressure. Severe ringing begins at 1905 us which is consistent with the estimated time of arrival of the copper plate.

---

*The length of the shock tube and the sphere ranges were increased to give a longer time interval between shock arrival and arrival of the copper "Gurney" plate.

**Both the static and dynamic pressures predicted from the TOA data depend linearly on the ambient air density in the shock tube. Using the weather conditions (80°F, 29.490 in Hg, 44% relative humidity) reported at the Miramar Air Station near the Green Farm test site, we derived an ambient density of 1.16 mg/cm'. However, this shock tube had been buried in the ground for over a month and it was possible that the air in the tube was cooler and more nearly saturated. For example, at 50°F (10°C), the density would be about 1.24 mg/cm', a 7% increase.

SECTION VIEW:

Extra Dampening Sheet

Slots

A'

Flow

Direction

Aluminum
Back Half,
Split in Two,
Cork Between
Parts

Biwax Filled
Cavities in Steel
Front Half

A

Nylon Bolts
Between Hemispheres

Biwax Filled Cavitites

A'

END
VIEW OF
STEEL
HALF:

(2) 15mm Deep
Slots Milled
Across Hemisphere

A
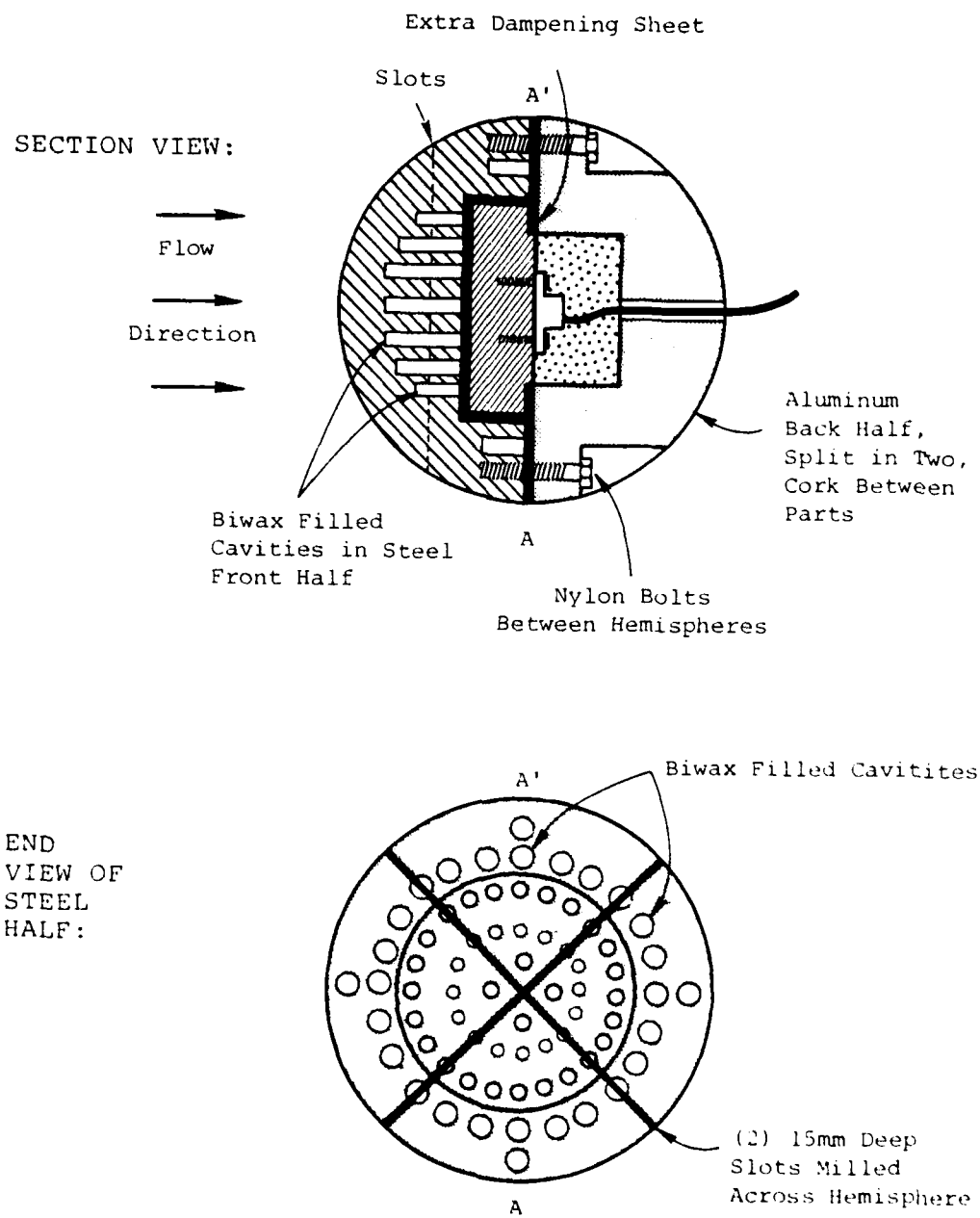
Figure 19. Final design for "composite" sphere. (Only
major changes from Figure 16 are shown.)

41
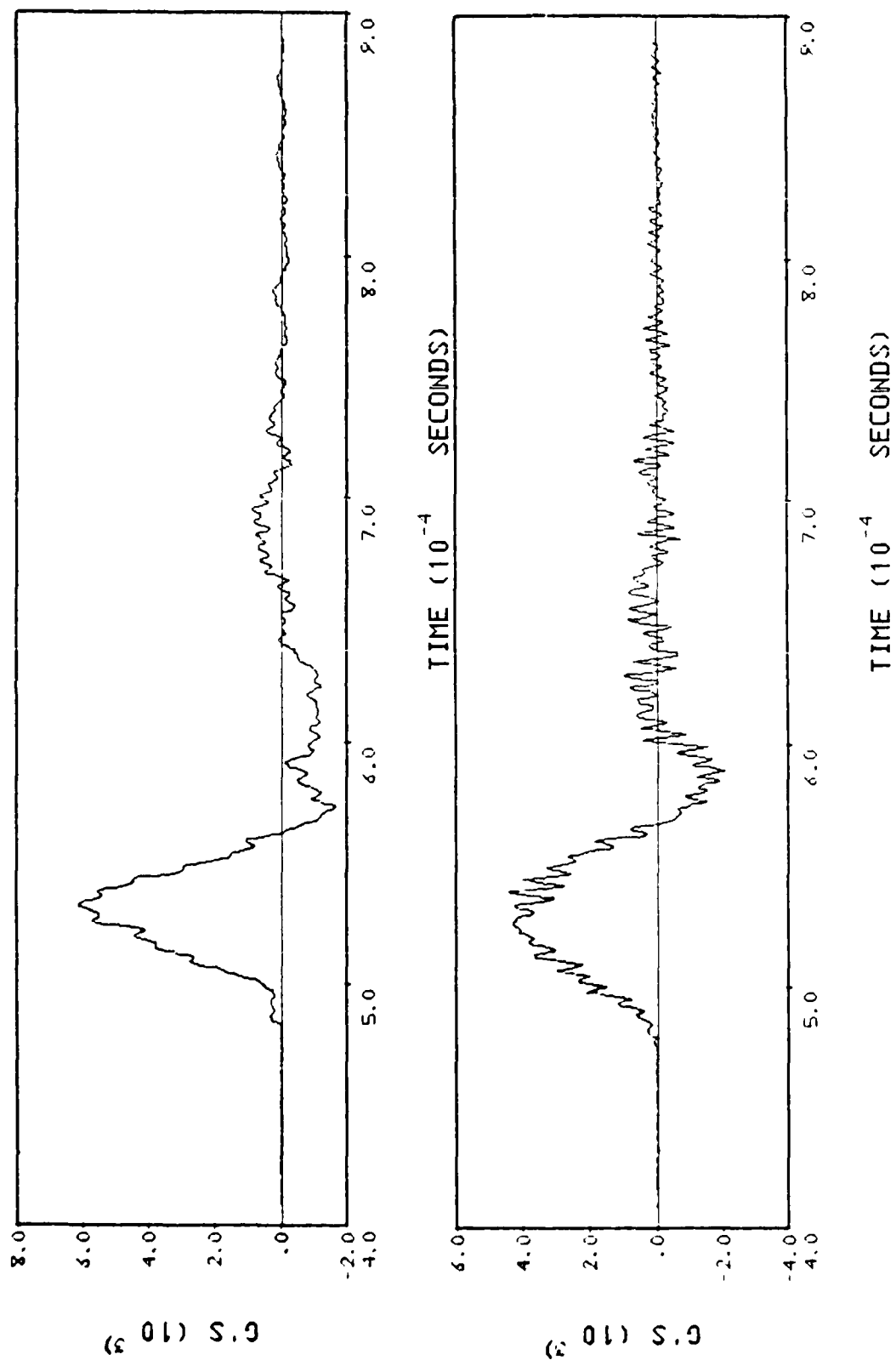
Figure 20. Lab tests of spheres used for shock tube test 4. Top trace – sphere placed at 3.5m. Bottom trace – sphere placed at 5.0m.
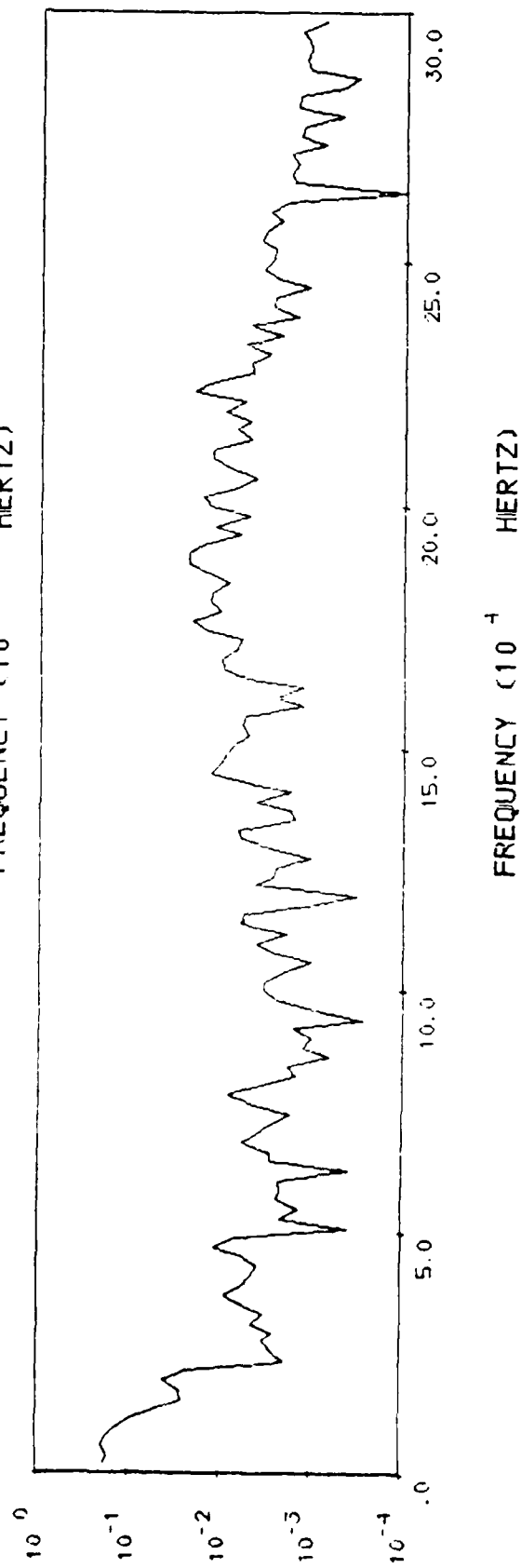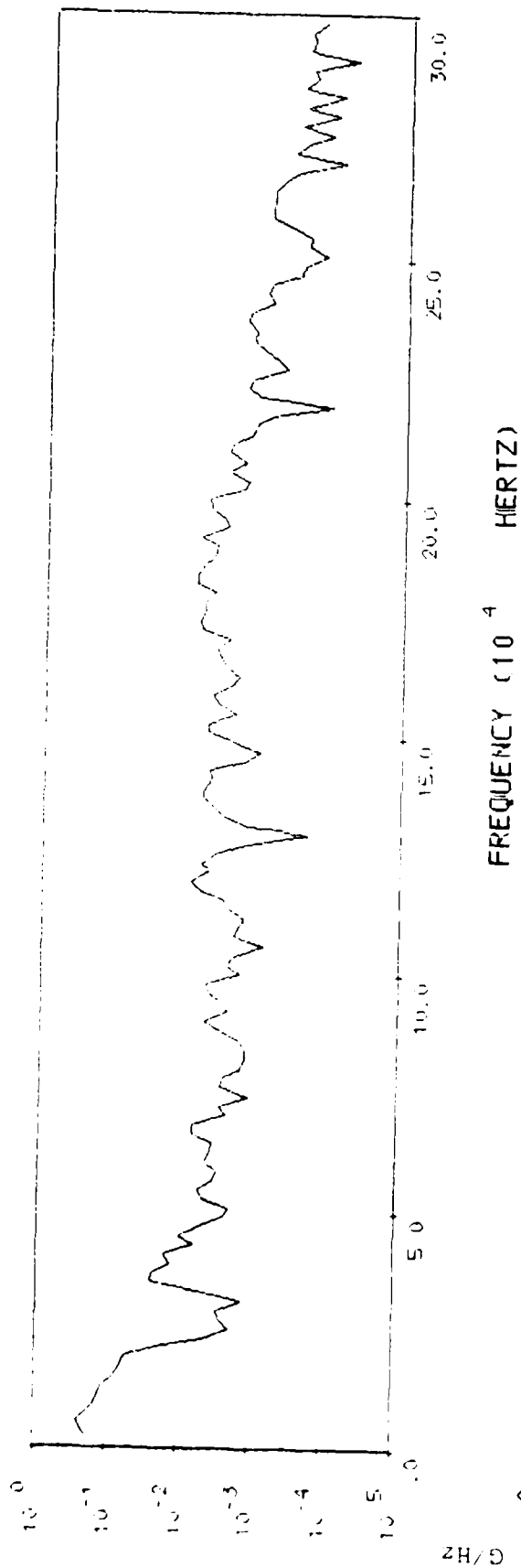
Figure 21. Fourier spectra of lab tests for spheres used for test 4. Top trace – sphere placed at 3.5m range. Bottom trace – sphere placed at 5.0m.

43
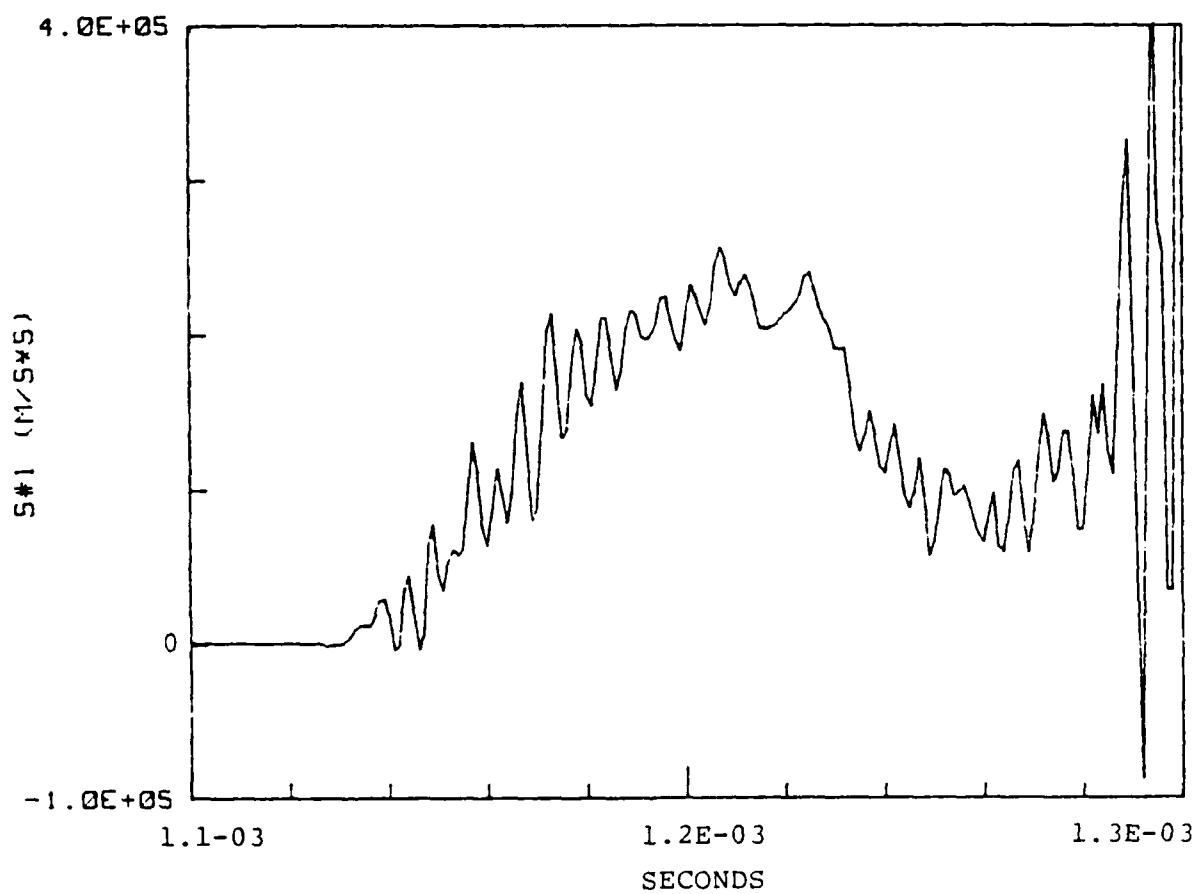
Figure 22. Accelerometer signal for sphere at 3.5m range
on shock tube test 4.
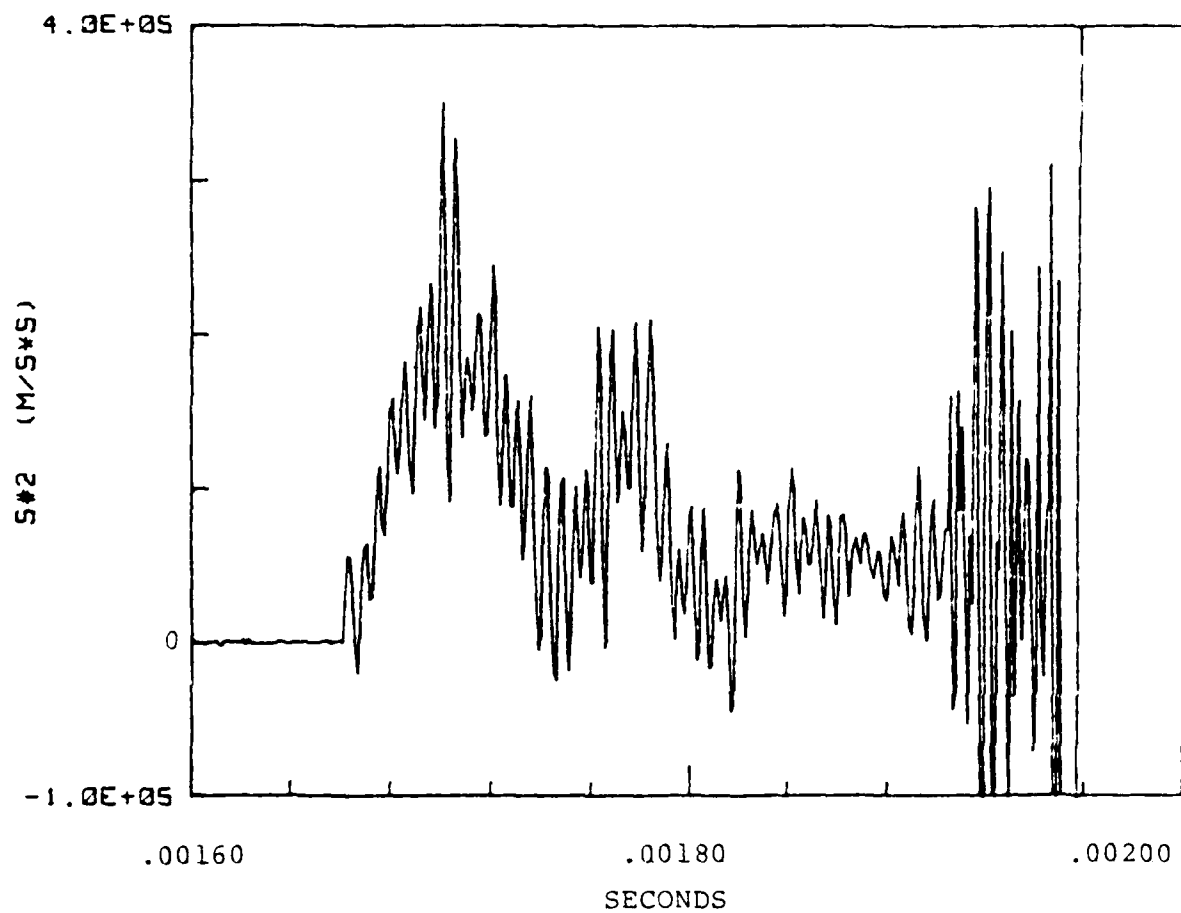
Figure 23. Accelerometer signal for sphere at 5.0m range on shock tube test 4.

The spectra of these two signals (up until the plate contact ringing) are shown in Figures 24 and 25. Since the overall waveforms have risetimes of tens of microseconds, we applied a 100 kHz low pass digital filter (Kaiser and Reed, 1977[15]) to both signals and plotted them on a common scale with first motions coincident. Figure 26 shows this comparison. While both spheres show a low level resonance at 65 kHz, there are marked differences in risetime and decay duration at the peak. The risetime for the sphere at 3.5 m is about 40 μs; the maximum acceleration lasts for about 50 μs. For the sphere at 5.0 m, the risetime is about 25 μs and the peak lasts for less than 30 μs. These variations may be due to slight varia-tions in the internal construction of the spheres. They might also be associated with the non-planarity of the shock. At 3.5 m range, the shock has traveled only 11-1/2 tube diameters and could still have had radial flow components due to the point initiation of the HE (Wright, 1961[16]). In addition, "initi-ation" of the shock is not instantaneous; roughly 40 μs are needed to accelerate the copper "Gurney" plate to 95 percent of its final velocity and its displacement during that time is roughly 90 mm.

We also note that part of the observed risetime may not be due to the internal construction of the sphere. Some time is surely required after the shock first contacts the sphere for a "steady" flow field to be set up around the sphere. Bryson and Gross, 1960[17]) show examples of shock fronts enveloping spheres at large Mach number (3) and Reynolds number ($\approx 8 \times 10^4$). Their data and analysis suggest that the front must move a distance of one to two sphere diameters after first contact to establish the flow pattern around the sphere. For our test, the equivalent time interval would be 20 to 40 μs. During that time, the drag force on the sphere is probably not constant.

At late times, the apparent dynamic pressure at the second sphere (Figure 27) has decayed to about 7 MPa (70 bars).

46
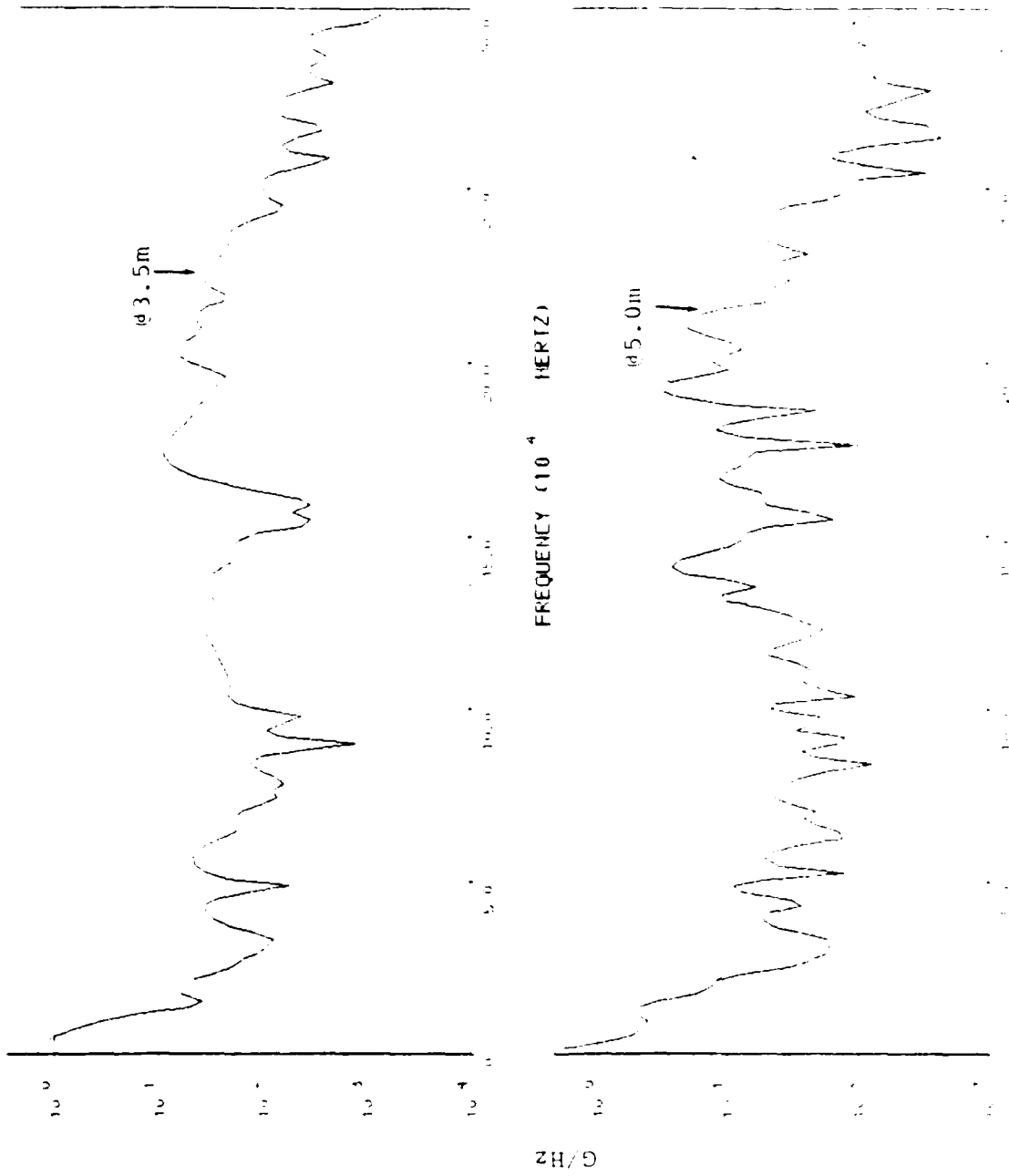
Figure 24. Fourier spectra (log amplitude in G/Hz versus frequency) for accelerometer signals on shock tube test 4.
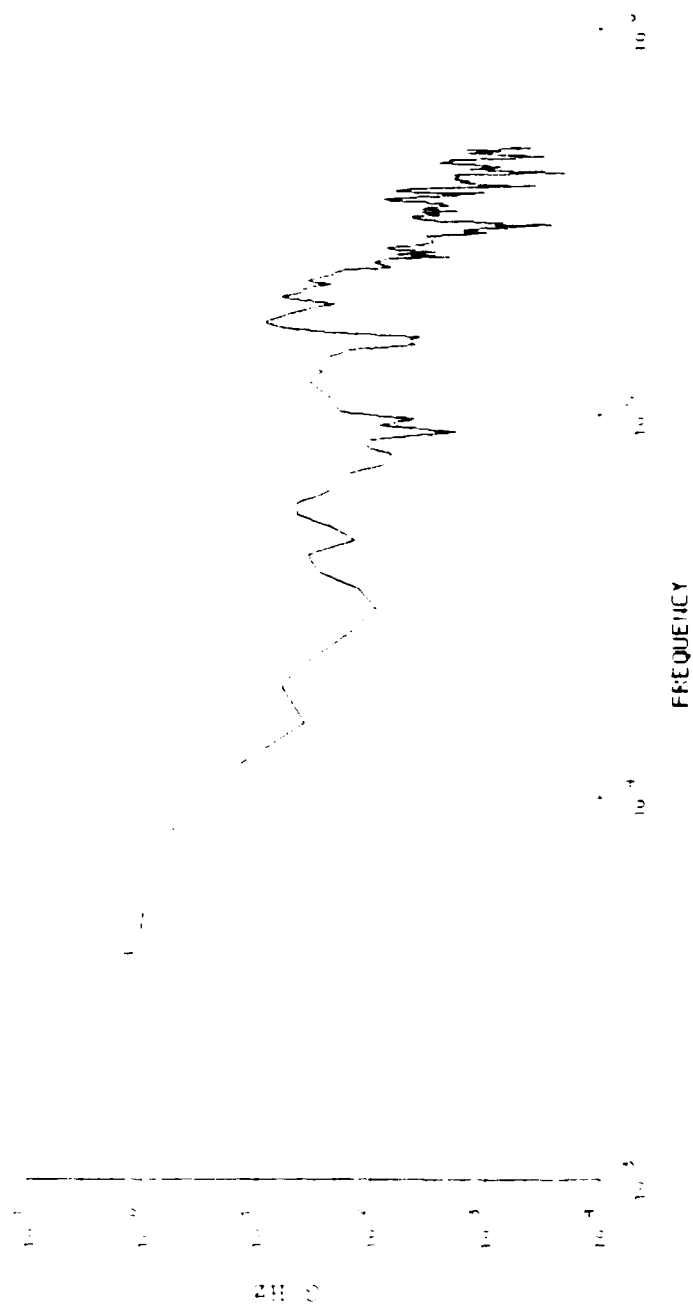
Figure 25. Log – log plot of Fourier spectrum for sphere at 3.5m, test 4.

FREQUENCY

48
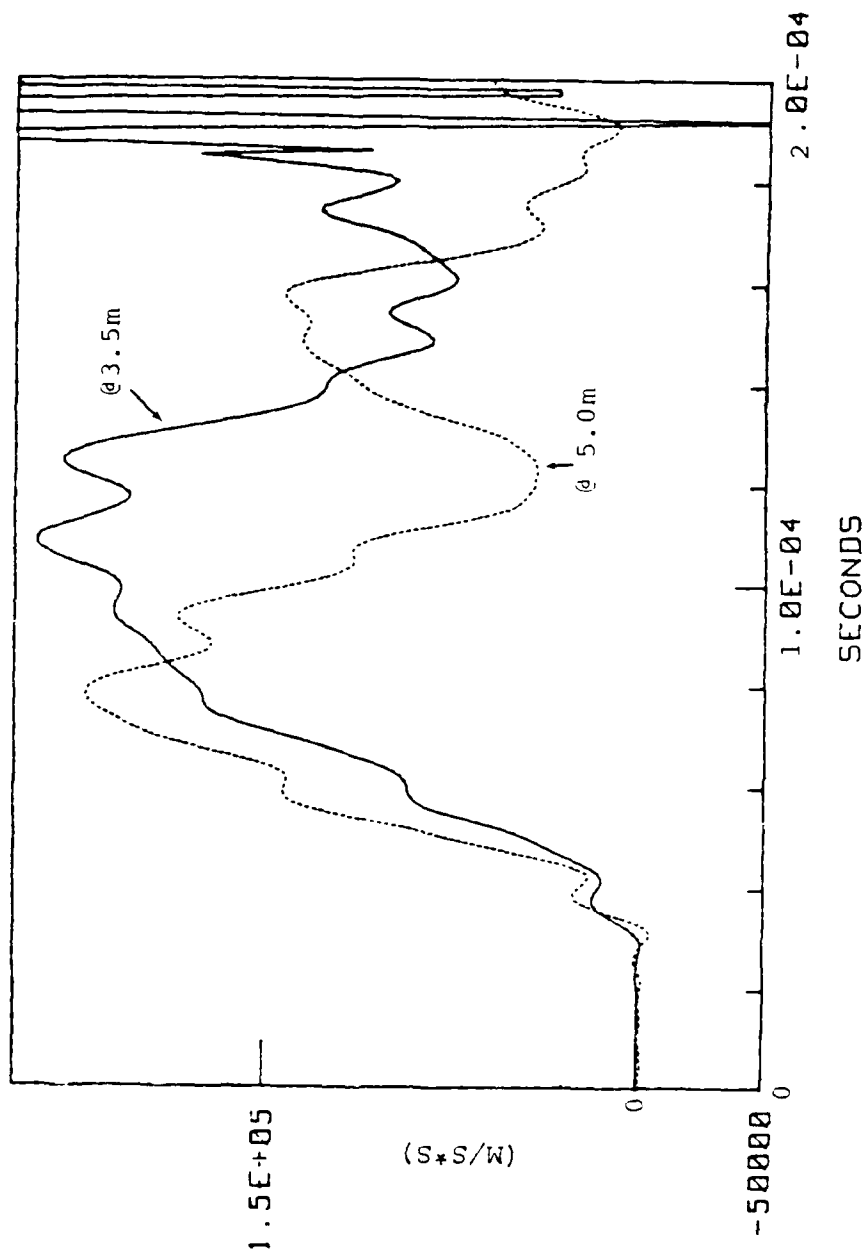
Figure 26. Lo-pass filtered sphere records, test 4, superimposed at first motion. (Absolute value of time scale is arbitrary.)

49
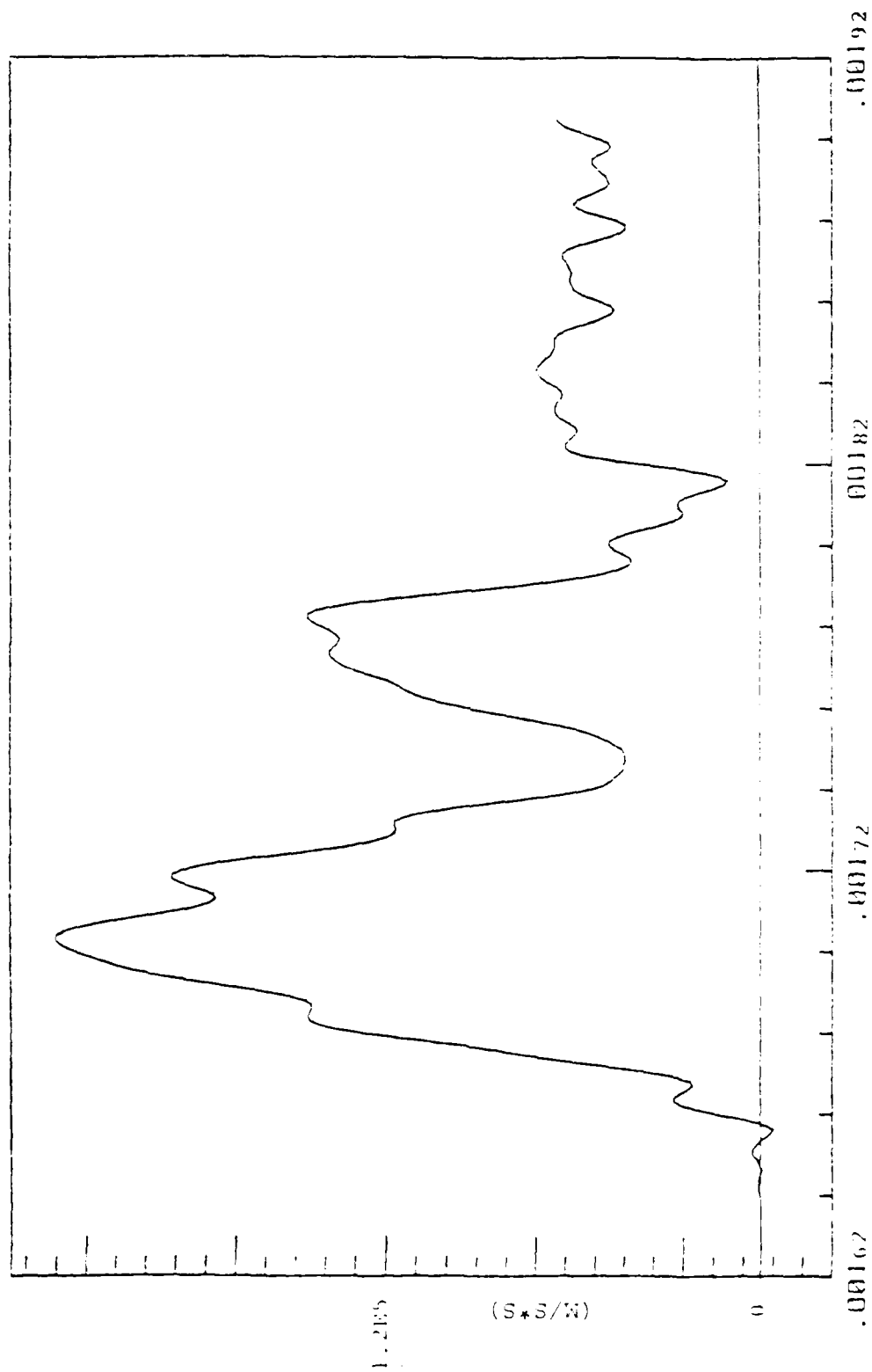
Figure 27. Lo-pass filtered version of data for sphere at 5.0 m range on test 4. (Cutoff frequency was 100 kHz.)

50

At 120 µs after shock arrival, the dynamic pressure is down by
roughly a factor of two from the peak. Since the static pres-
sure (Figure 5) has even slightly increased at the same time,
the density of the shocked gas cannot be decreasing significantly.
Hence, the reduced dynamic pressure must be associated with a
~40 percent decrease in axial flow velocity. Perhaps expansion
of the shock tube walls has already made the flow significantly
two dimensional by that time.

2.5   CONCLUSIONS

We have demonstrated that an accelerometer instrumented sphere can be designed so that resonances in the sphere do not seriously compromise the quality of the signal nor the survival of the accelerometer. Empirical evidence suggests that the key to controlling the sphere's natural oscillations is to give the sphere a nonuniform internal structure which eliminates uniform paths for sound propagation in the sphere.

For supersonic flow behind a shock (static pressure above ~100 psi in air), the sphere could give dynamic pressure data good to perhaps ±20% if the flow's duration is sufficiently long to establish a "uniform" flow field about the sphere. In subsonic flow, the dynamic pressure measured by the sphere will likely be a factor of 2 to 4 less than the actual dynamic pressure; this is due to the reduced drag coefficient at low flow velocities.

Additional laboratory experiments using impacts of the sphere with another sphere (see Section 2.2) or a bar gauge (see Appendix A) could lead to some improvements in the construction of the gauge. However, the next significant step would be to field the drag spheres on a large (many ton) HE test to measure the flow behind the air shock and compare the data with detailed code calculations.

SECTION III

APPLICATIONS OF BAR GAUGES TO AIRBLAST MEASUREMENTS

3.1 INTRODUCTION

For purposes of making measurements of the blast wave due to a nuclear explosion in an underground cavity, bar gauges (Coleman, 1979)[5] have several advantages. The separation of the pressure transducer from the sensitive end of the gauge introduces a useful time delay between the prompt electrical noise induced by EMP and gamma radiation, and the pressure signal. In addition, the transducer can be located in the cavity wall and thus be better shielded from the device.

Coleman, et al (1976)[18] considered several generic packages for the bar gauge to measure static and stagnation pressure in the blast flow. Kratz, et al (1978)[1] reported on initial efforts to solve the practical problem of coupling the pressure on the surface of a wedge (inclined at an angle to the flow direction) to the bar which would be aligned parallel to the flow.

We discuss below several possible configurations for bar gauges to measure blast pressures. The results of initial tests of these configurations in HE driven shock tubes are given.

3.2 QUANTITIES OF INTEREST

In the flow behind a shock front, the three primary quantities of interest are the static (i.e., thermal) pressure and density of the gas and its flow velocity. The static pressure, P_s, (and shock velocity) are relatively easy to measure. The gas density and flow velocity are

relatively difficult to directly monitor in a non-laboratory
environment. The dynamic pressure, $1/2\rho u^2$, may be measurable
with the drag sphere concept discussed in Section II. The
pressure measured on a small surface area normal to the flow,
the stagnation pressure P_m, is readily detected in subsonic
flow. In supersonic flow, we have

$$P_m/P_s = \frac{\left(\frac{\gamma+1}{2} M^2\right)^{\gamma/\gamma-1}}{\left(\frac{2\gamma}{\gamma+1} M^2 - \frac{\gamma-1}{\gamma+1}\right)^{1/\gamma-1}} \tag{12}$$

where γ is the ratio of specific heats for the shocked gas,
and M is the Mach number of the flow. Since the gas density
can be related to γ, the stagnation pressure is also a
function of density and flow velocity. Finally, if the flow
is brought to a stop over an extended area, the resulting
reflected pressure, P_r, can be monitored with relative ease;
P_r is also a function of static pressure, gas density and
flow velocity.

For example, in the second shock tube test of Section
2.2, the observed shock velocity of 2.88 mm/μs at a range
of 3.0 m implied a static pressure of 8.8 MPa (88 bars),
a dynamic pressure of 28.0 MPa, a stagnation pressure of
56.9 MPa, a reflected pressure of 76.0 MPa, a flow velocity
of 2.49 mm/μs, a flow Mach number of 2.22, a speed of sound
in the shocked gas of 1.12 mm/μs, a temperature ratio across
the shock front, T_1/T_o, of 11.9, a density ratio, ρ_1/ρ_0, of
7.43 and a gamma of 1.29. By observing several quantities
such as shock velocity, and static, dynamic, stagnation and
reflected pressures, confidence in derived values of density
and flow speed would be increased. In addition, nonideal
features like dust entrainment could be identified. We turn
now to the details of three bar gauge packages designed to
respond to reflected, stagnation and static pressure respectively.

3.3   REFLECTED PRESSURE BAR GAUGE

In order to measure the reflected pressure out in the
flow away from a large rigid boundary, it is necessary to
provide a region ahead of the bar gauge that confines the
flow to one direction. The 6.35 diameter x 25.4 mm long
(1/4 x 1) air column at the front end of the probe shown in
Figure 28 was an attempt to establish such a region. Once
the shock reaches the front end of the bar gauge, it should
set up a reflected shock that advances back towards the tip
of the probe. When the reflected shock reaches the tip, the
flow around the probe should become similar to that due to
stagnation on the surface of a small object in the air stream.
Information concerning this flow adjustment will then return
to the bar at roughly the speed of sound in the shocked
column.

This gauge was placed at the 3.0 m range on test 2.
Figures 29 and 30 show the measured signals. The few micro-
second initial rise time is appropriate for this gauge but
the stress level of 45 MPa is low compared to an expected
(from TOA data) reflected pressure of 76 MPa or even a
stagnation pressure of 57 MPa. Within about 8 μs, the
observed pressure increased to 70 MPa and then decreased to
about 30 MPa after 30 μs. About 50 μs after apparent arrival,
the data jumped to over 200 MPa. The 305.4 mm long dump bar
led to a dump reflection feature 124 μs after first arrival.
Since the gauge was calibrated per equation A1 of Appendix A,
we believe the measured pressures are good to at least $\pm 10\%$.
However, the relation between the measured pressure and the
true flow pressures of interest is not clear. We estimate
from the TOA shock velocity that the reflected shock reached
the probe tip 50 μs after first arrival and than an additional
20 μs was needed for the flow readjustment to be felt by the
bar gauge. The several kilobar pulse starting at 970 μs is
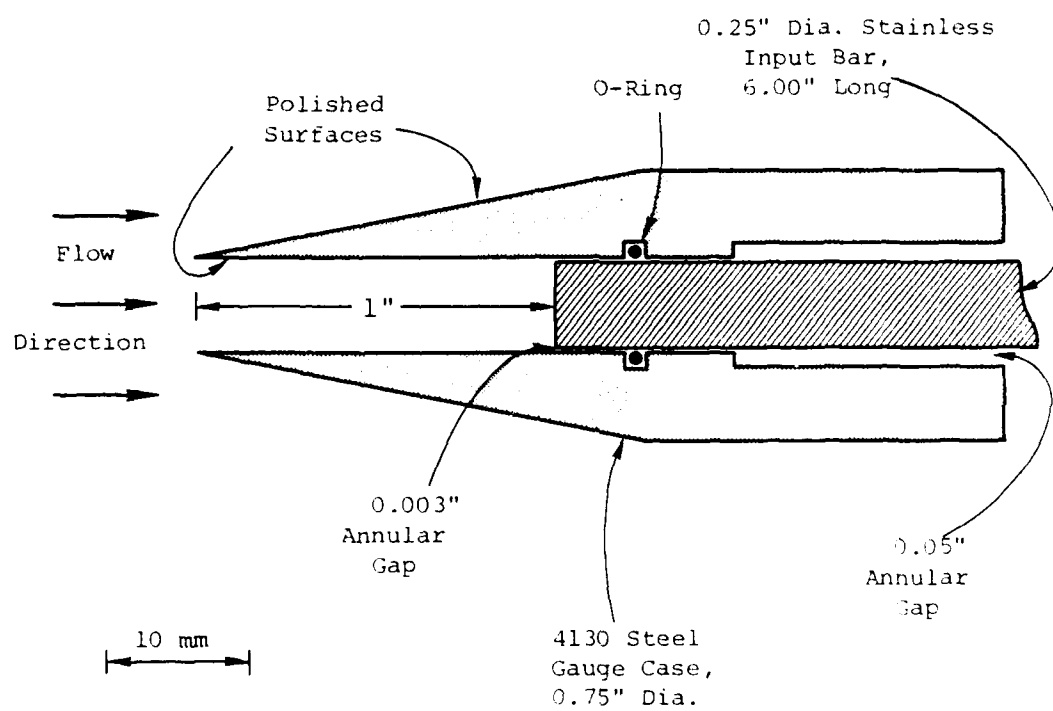
Figure 28.   Reflected pressure bar gauge,
             front end detail, section view.
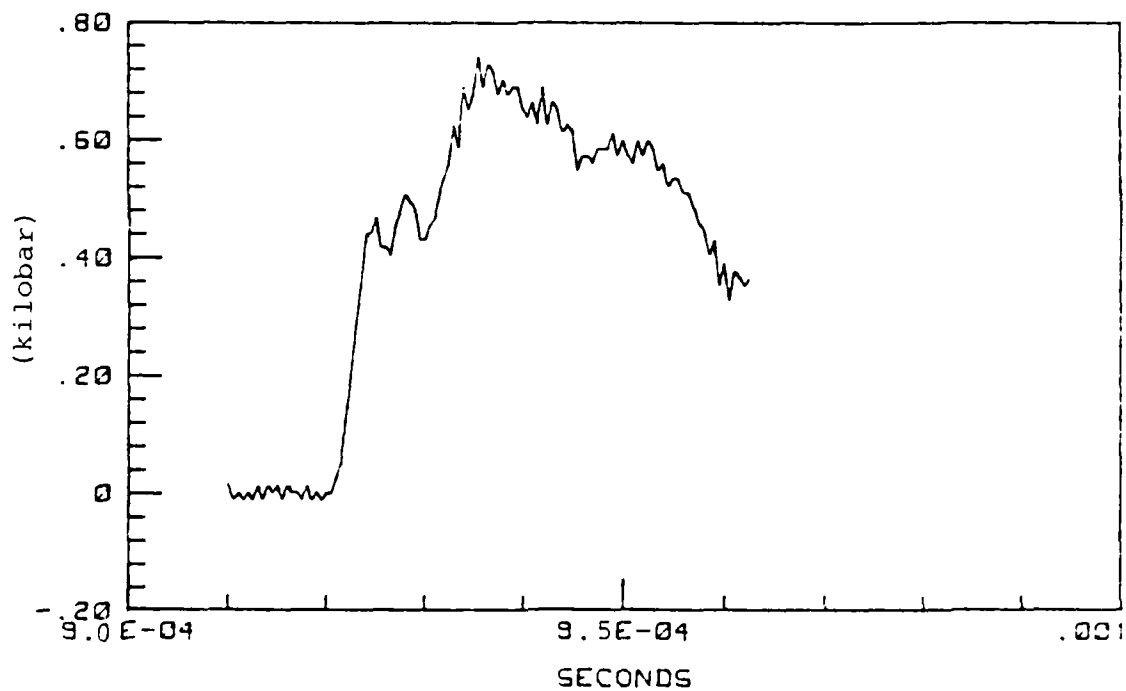
Figure 29.   Initial signal for the reflected pressure bar
             gauge probe on test 2.   (Digital oscilloscope
             recording, 1 MHz bandwidth.)
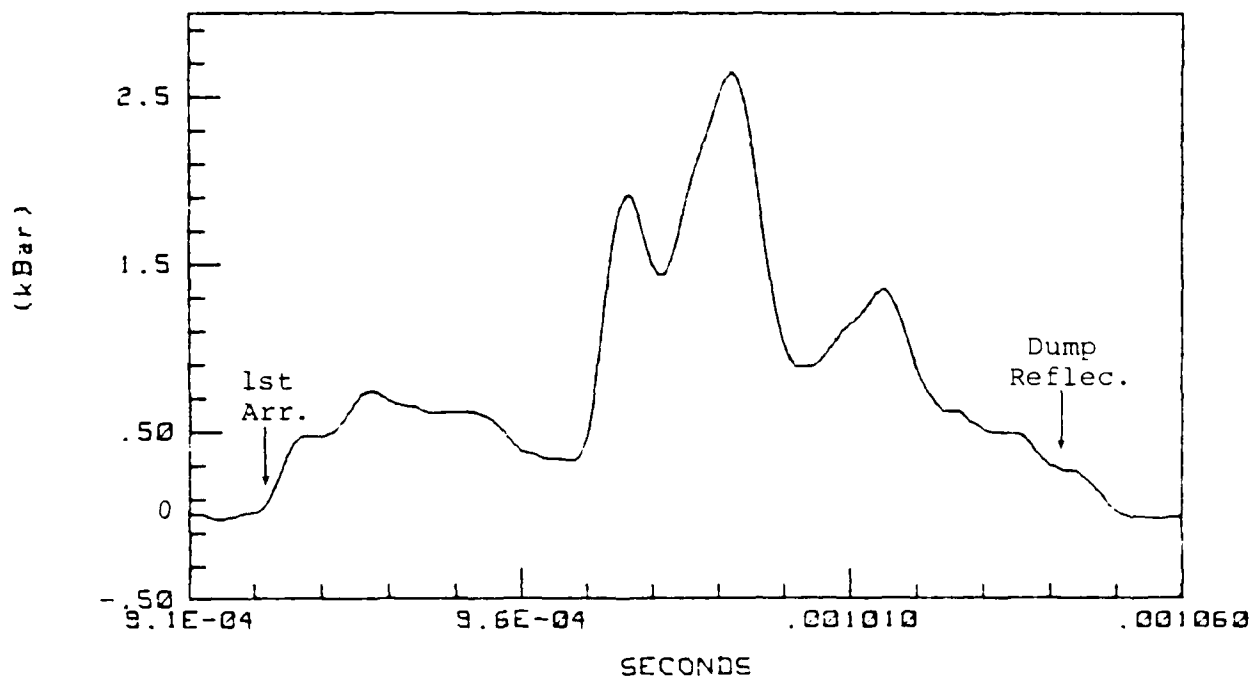
Figure 30. Complete signal for the reflected pressure bar
gauge on test 2. (FM tape playback, 30 kHz band-
width.)

difficult to explain in terms of the flow. It is possible
that the pressures on the gauge case were sufficient to close
the nominal 0.003 inch gap between the case and bar; in that
case, drag on the case could be coupled to the bar and give
extreme pressure features. An even more serious problem is
the apparent arrival time of 922 μs, 28 μs before the shock
arrival given by the TOA pin, drag sphere and static bar
gauges all at the same range. We have no clear explanation
for this; either the gauge was misplaced at a range of about
2.92 m, or the shock front was not uniform in cross-section
or anomalous stress waves in the bar were introduced by
some feature of the gauge design. None of these possibilities
seem likely.

This gauge concept may have some value as part of a
suite of air blast instruments, but many details must be
resolved to have a viable instrument. Aside from the anomalies
evident from the shock tube test, it would be important to
evaluate the sensitivity of the gauge to misalignment with
the flow direction.

3.4 STAGNATION PRESSURE BAR GAUGE

Stagnation pressure is measured on the surface of a
small area aligned normal to the flow, see Figure 31. Initial-
ly, the pressure on the area is the reflected pressure.
However, as the shock advances, a rarefaction wave moves in
from the perimeter of the area at the speed of sound of the
shocked air; see Butler (1966)[19]. For our gauge, the rare-
faction should reach the bar axis within about 7 μs. The
measured pressure approaches the stagnation value during
that time interval.

This design was placed at a range of 3.0 m on the
third shock tube test. Figure 32 shows the observed signal.
The arrival time of 888 μs is in excellent agreement with the

0.75" Dia. Case,
4130 Steel, Hardened

0.25" Dia. Stainless
Input Bar, 6" Long

0.1" Annular
Air Gauge

0.003 Annular
Gap

Flow

Direction
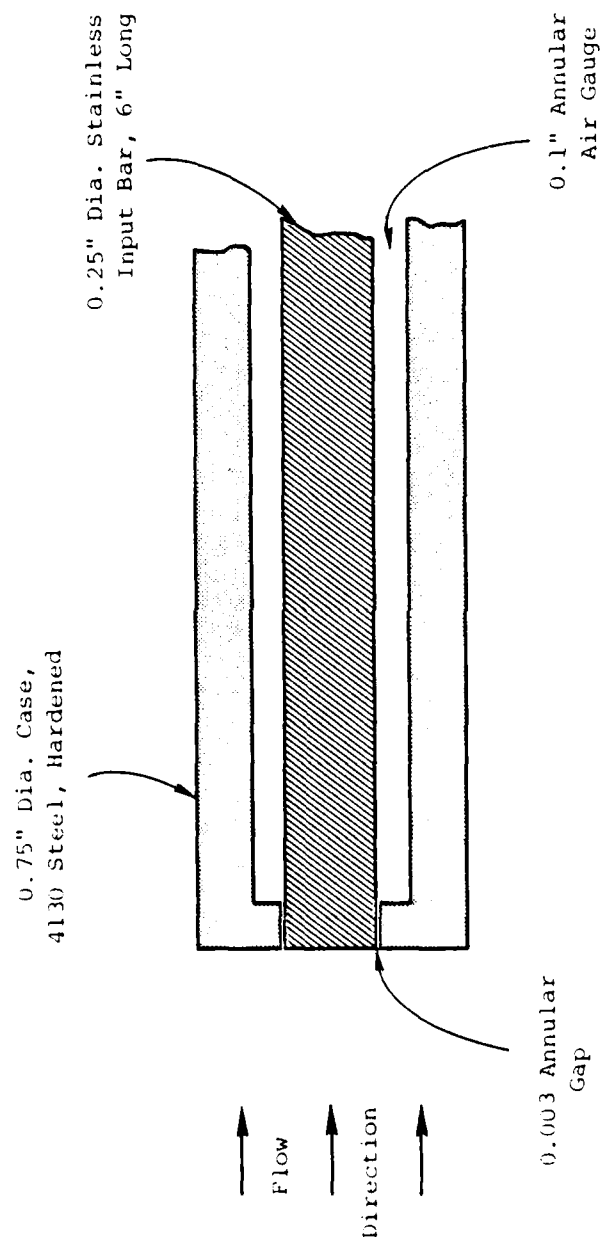
Figure 31.   Sensitive end of stagnation bar probe,
section view.

Figure 32. Signal for stagnation pressure bar probe on test 3.

61
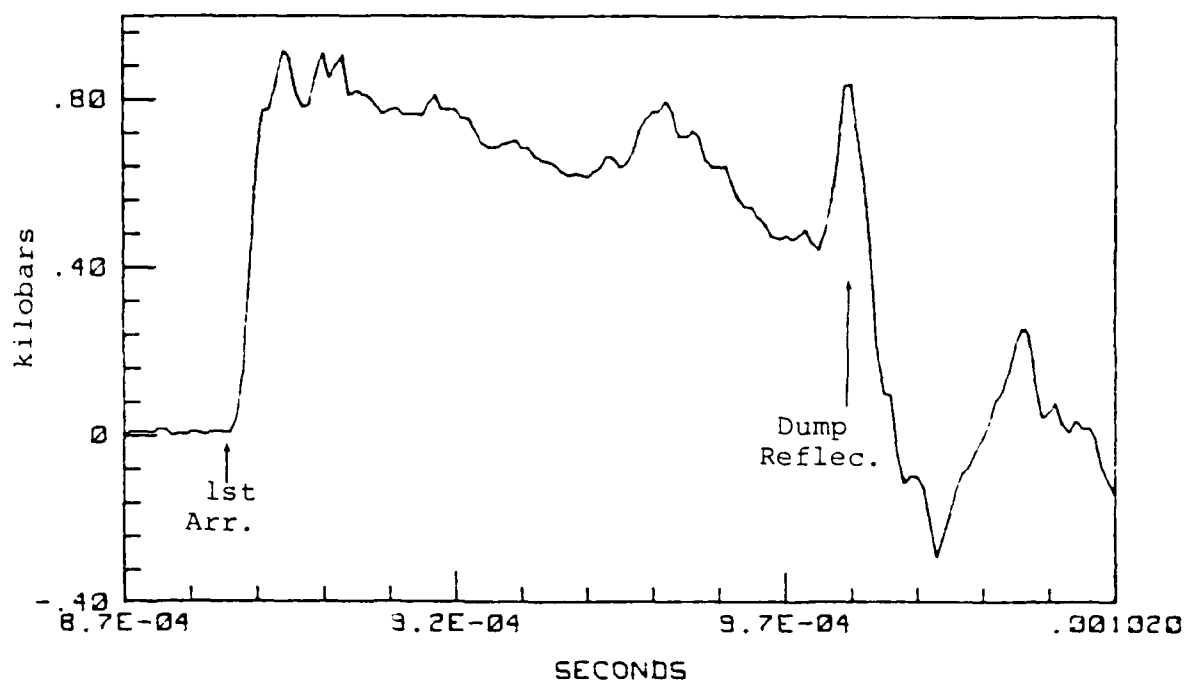
other TOA measurements. The few microsecond response time of the bar obscures the initial transition from reflected to stagnation pressure. The peak pressure (neglecting ringing due to dispersion in the bar) is 85 MPa (850 bars) which is well above the 59 MPa predicted from the TOA data. It is possible that case contact with the bar could induce the extra measured bar pressure. The overall shape of the measured pulse is plausible.

Some straightforward changes in gauge construction could eliminate the possible contact of case with the bar sides. In particular, the 0.003 inch annular gap could be greatly increased and the bar's end could rest against a thin metallic diaphram attached to the case end. Such an approach was quite successful for the bar gauges used on the HYBLA GOLD event (Coleman and Kratz, 1979).[20]

3.5   STATIC PRESSURE PROBE

The classical technique to measure static pressure in a flow field is to introduce a streamlined probe into the stream and measure the pressure on its lateral surface. The point of pressure measurement should be at least ten probe diameters downstream from its tip. The surface of the probe should be smooth in comparison to the thickness of the boundary layer, $\sqrt{\nu x/u}$, where ν is the kinematic viscosity (1.5×10^{-3} m^2/s for air at STP), x is the distance from the probe tip and u is the flow velocity. Any ports or other structural features connecting the pressure gauge to the surface also should be small compared to the boundary layer thickness.

Kratz, et al (1978)[1] envisioned the use of a piston mounted flush with the probe's surface and pushing on a small reservior of mercury. The bar gauge, contained within the probe along its axis, would have its sensitive end form one

of the boundaries of the reservoir. Initial lab tests
indicated some problems with friction between the piston
and the probe case. In addition, the piston measures the
pressure on one surface only (for a wedge-like probe) or
over only a small portion of the circumferential surface
(for a circular probe). If the probe is not perfectly
aligned with the flow, the measured pressure will be in error.

In an effort to eliminate some of these problems, we
pursued the cylindrical design shown in Figure 33. The
mercury reservoir was ported to the probe surface via eight
holes around the circumference; the objective was to get the
average pressure on the surface of the probe to the bar gauge
and thus reduce errors due to misalignment. A 0.025 mm
thick stainless steel diaphram capped the ports and eliminated
the use of discrete pistons.

This design was placed at a range of 3.0 m (to the
mercury ports) on the third shock tube test. Figure 34
displays the recorded signal. All other gauges at this range
indicated shock arrival at 889 ± 1 μs. While this gauge
showed a feature at that time, the 2 MPa maximum was small
compared to the 9.1 MPa level consistent with TOA data and
the side wall bar record at a range of 1.5 m (Figure 4).
The roughly 1 MPa signal that appeared about 20 μs before
shock arrival may be due to a pressure wave induced in the
probe case at its tip and propagated at the sonic velocity
of steel (5 x 10^3 m/s) to the reservoir. In principle, this
anomalous signal could appear up to 35 μs before the shock
using the observed shock velocity of 2.96 mm/μs.

After a time of 940 μs, the measured pressure did rise
to 6 MPa and may represent a reasonable response to the true
static pressure. The severe excursion starting at 990 μs
may be due to contact of the probe case with the bar. A
dump reflection feature corresponding to the rise at 920 μs
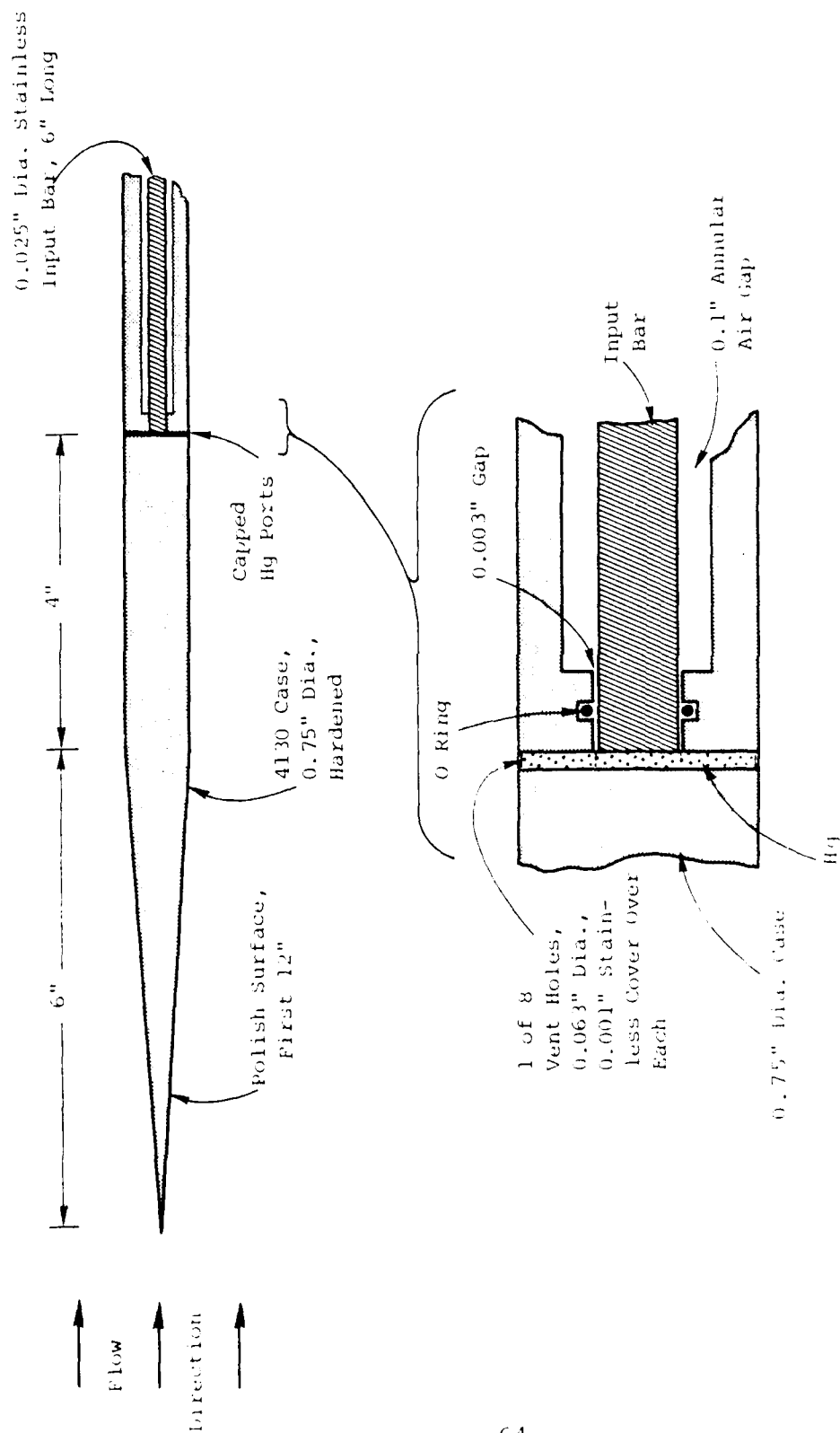
Figure 33. Static pressure bar probe. Upper – Overall section view. Lower – Detail of mercury reservoir at front end of bar.

0.025" Dia. Stainless Input Bar, 6" Long

Capped Hg Ports

4130 Case, 0.75" Dia., Hardened

Polish Surface, First 12"

6"

4"

Flow Direction

0.003" Gap

Input Bar

0.1" Annular Air Gap

O Ring

1 of 8 Vent Holes, 0.063" Dia., 0.001" Stainless Cover Over Each

0.75" Dia. Case

Hg
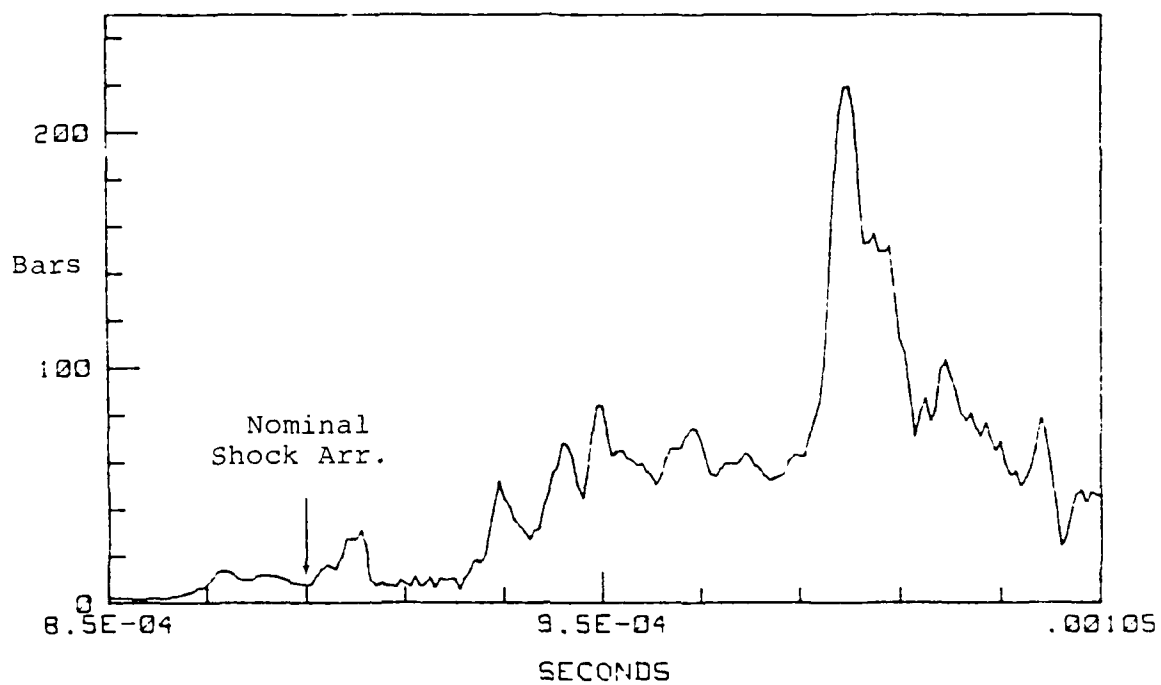
Figure 34. Response of the static pressure bar probe to the third shock tube test.

is present at about 1055 μs.

This initial test of the probe was not encouraging. With additional effort, the concept might prove workable. In particular, it is possible that there was a small bubble in the mercury which could explain the poor response to the shock. Improved construction techniques should eliminate that problem. The completed probe is difficult to test in the lab. Some simple test equivalent to the drop ball system (Appendix A) is needed. Coupling of sound through the leading portion of the probe into the reservoir must also be eliminated. Finally, improved isolation of the bar's tip from the case might be possible if the bar gauge presses against a diaphram that forms one boundary of the reservoir.

SECTION IV

INITIAL DEVELOPMENT OF A DYNAMIC SOIL STRENGTH GAUGE

4.1   INTRODUCTION

Soil strength is an important parameter in the calculations of cratering and of structure-medium-interaction (SMI). There is a possibility that the explosion induced stress pulse may affect the strength of the surrounding soil. Pre-shock and post-shock strengths are often assumed to describe the observed motions in cratering studies (Cherry, 1967[21]; Terhune, Stubbs and Cherry, 1970[22]). Since the stress pulse passes through the medium well ahead of the main motions of cratering or SMI, sufficient time may be available to make a measurement of any change in soil strength. The choice, design, and construction of a gauge capable of measuring such changes in soil strength would be of a great benefit in verifying the validity of the assumed shock induced strength change. The measurements of strength changes could then be used to improve the modeling of a cratering event.

The soil strength gauge will be subjected to a unique environment. For a reusable gauge, it must be placed beyond the true crater radius and be able to withstand the accelerations and stresses characteristic of that point. The gauge must also be able to continuously monitor the soil strength before and after passage of the stress pulse. If the stress gauge is sufficiently rugged it could be implaced within the radius of the true crater, make real-time strength measurements during the period of interest to modeling and be expended when ejected from the forming crater.

4.2 BACKGROUND

Presently there are three major methods for measuring soil properties in-situ; the standard penetration test (SPT), the vane test, and the cone penetration test.

The standard penetration test (SPT) involves boring a hole to some depth where the sampling spoon is placed. The operator counts the number of blows of a falling hammer which cause the spoon to penetrate one foot. The spoon, essentially a rod with a cavity in the tip, collects a sample of soil during the test. The blow count can be related empirically to the effective angle of internal friction, ϕ', for soil. The effective angle of internal friction can also be estimated from an intermediate parameter, the relative density of the soil D_r.

In the vane test the soil is penetrated by a rod. On the end of the rod are four fins which are initially perpendicular. The torque which causes the rod to turn is measured. This torque is related directly to the undrained shear strength of the soil, S_{uv} (Mitchell, Guzikowski and Villet, 1978[23])

$$S_{uv} = \frac{2T}{\pi D^3 \left(\frac{H}{D} + \frac{a}{2} \right)} \tag{15}$$

where

      T = maximum applied torque,

      H = vane height,

      D = vane diameter,

      a = shear distribution factor (it depends on the shear distribution along the top and bottom of the failure cylinder created by the vanes).

The cone penetration test relates the soil strength parameters to the load required to achieve penetration. Two

types of cone penetration tests are commonly used: (1) the dynamic test, (2) and the quasi-static and sometimes static test.

The dynamic cone penetration test is very similar to the SPT. The operator counts the number of blows of a falling hammer necessary for the cone to penetrate a certain distance. The results are related to the soil strength parameters by empirical methods.

The quasi-static and static tests measure the applied load necessary to maintain a constant rate of penetration (for the quasi-static test the rate is usually two centimeters per second and for the static test the rate of penetration is much smaller, typically one centimeter per minute). The "Dutch cone" design is the most common. In this design, the cone has an included angle of 60° with a base of unit area. The cone is hydraulically propelled with the load measured either mechanically or electrically. The load required to cause penetration is the combination of the friction between the rod and soil and the resistance of the soil to penetration of the cone tip. Some designs measure these parameters separately by utilizing a separate friction sleeve around the rod. This friction sleeve is held stationary while the cone-tipped rod penetrates a certain distance.

4.3   GAUGE DESIGN

The design of a soil strength gauge for crater modeling must be considered in the context of fulfilling these necessary requirements:

1)   the gauge must continuously monitor the soil strength parameters before and after the passage of the stress pulse,

2)   The gauge should be reusable for crater radius measurements (i.e., it should survive the 0.25 kbar peak stress and 1000 g peak acceleration characteristic of the crater lip region as estimated from MIDDLE GUST III data); and possibly expendable for measurements made at less than one crater radius,

69

3) the gauge must be easily installed and recovered with a minimum number of operational components subject to airblast and throw-out.

The quasi-static and static cone penetration design is capable of fulfilling these three requirements with less effort than the other designs. The SPT, dynamic cone penetration test, and the vane test do not measure soil strength parameters continuously, however, the quasi-static and static cone penetration tests do. Also, it would be more difficult to design a gauge that fulfills requirements two and three based on the vane test design, SPT, or dynamic cone penetration design than it would be for a design based on the quasi-static and static cone penetration test.

Several different approaches were possible for designing a soil strength gauge based on the quasi-static and static cone penetration test. The gauge should penetrate parallel to the ground motion vector in order to reduce the possibility of damage to the penetrating rod. Also, to eliminate exposure to airblast and throw-out, the gauge can be installed in a borehole. The depth of penetration should be at least a borehole diameter so that the disturbed soil adjacent to the hole does not contribute to the strength measurement. With a vertical borehole the gauge would be lowered to the required depth. Once positioned the soil would be penetrated in a plane perpendicular to the axis of the borehole. Figures 35 and 36 show two designs for a gauge that could be dropped down a vertical borehole. Figure 35 is a design for an electromechanical penetrator and Figure 36 is a design for a hydraulic penetrator. In either case, the penetration resistance of the soil would be measured by a load cell. Of the two, the hydraulic penetrator would be less susceptible to damage induced by the stress pulse. In either case it would be difficult to design a gauge that could penetrate beyond one borehole diameter. Telescoping sections could be used but then the gauge would be more sensitive to damage from the stress pulse.

70

Borehole

Wire Rope,
Motor Power Line,
Signal Leads

Body

Motor (Submersible Pump)

Gear Box

Ball Screw

Load Cell

Roller Chain (Confined)
Penetrating Cone
    (Telescoping)
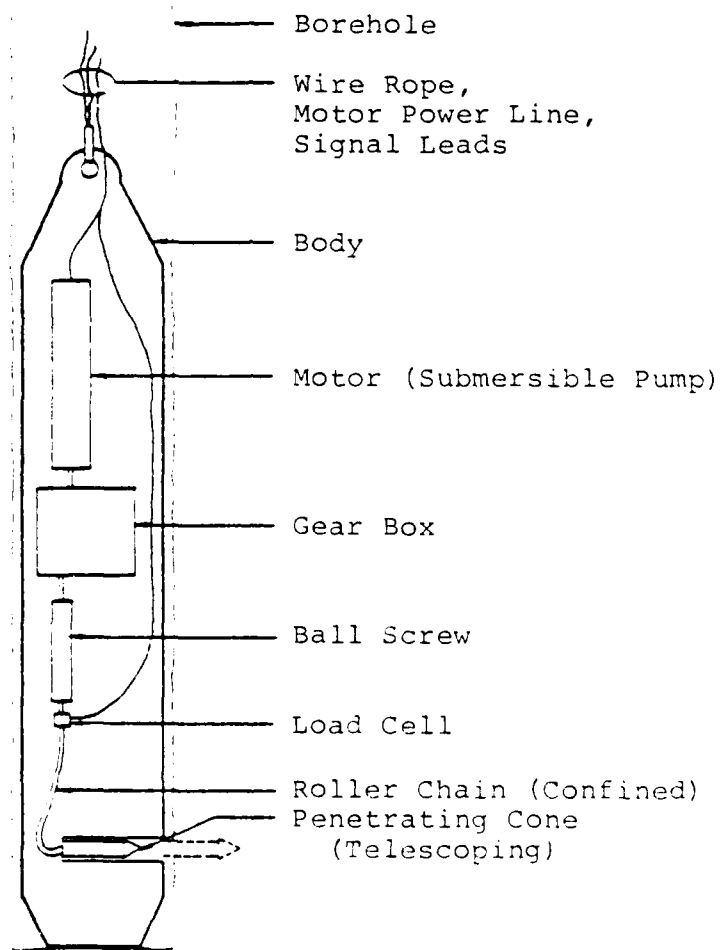
Figure 35.   Concept of an Electrically Driven,
              Telescoping, Cone-Point Penetrator
              Gauge.
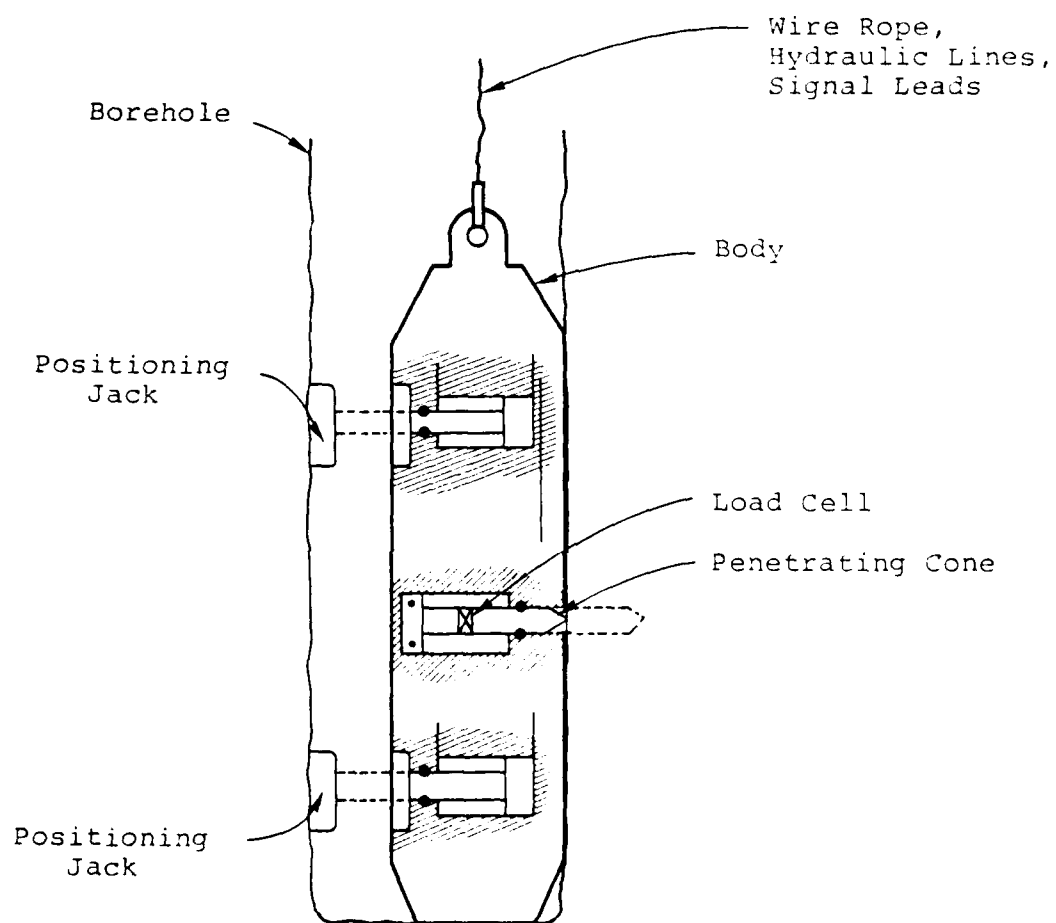
Figure 36. Concept of a Hydraulically Operated
Cone-Point Penetrator Gauge.

The near horizontal borehole gauge would penetrate
the bottom of the hole (Figure 37). The depth of penetration
would be limited only by the length of the body of the gauge.
Once the gauge is positioned, the borehole would be backfilled
by grout to provide the necessary support for the gauge body.

The prototype soil strength gauge (Figure 38) utilizes
the near horizontal downhole design. A standard Dukes model
WC 2512 hydraulic cylinder was modified to contain a PCB model
230A load cell in the penetrating rod. Also a 60° included
angle hardened steel cone tip was attached to the end of the
rod.

This gauge is capable of providing about 1 kbar at the
cone tip. This is sufficient to penetrate all but the densest
of soils. Durgunoglu and Mitchell (1975)[24] indicate that
the range of loads necessary for the penetration of various
sands is between 10 bars and 1 kbar.

Figure 39 shows the schematic layout of the penetrator
system. A constant volume hydraulic system is adjusted to
provide a flow such that the velocity of penetration is about
0.5 cm/sec. The four-way valve controls the operation of the
soil strength gauge by controlling the flow of hydraulic fluid
to and from the cylinder; forward, neutral and reverse are pro-
vided. The pressure by-pass controls the maximum differential
pressure that can exist between the inlet and outlet of the
hydraulic cylinder.

Two different types of experiments were devised to test
the operation of this prototype soil strength gauge. In one
the interface between two different strength soils would be pene-
trated while observing the load cell output. In the second, more
important experiment, the gauge would be installed in a single
strength soil, which would then be subjected to a stress pulse
simulating the environment of a cratering event. Such a stress
pulse can be approximated with a high explosive shock generator.
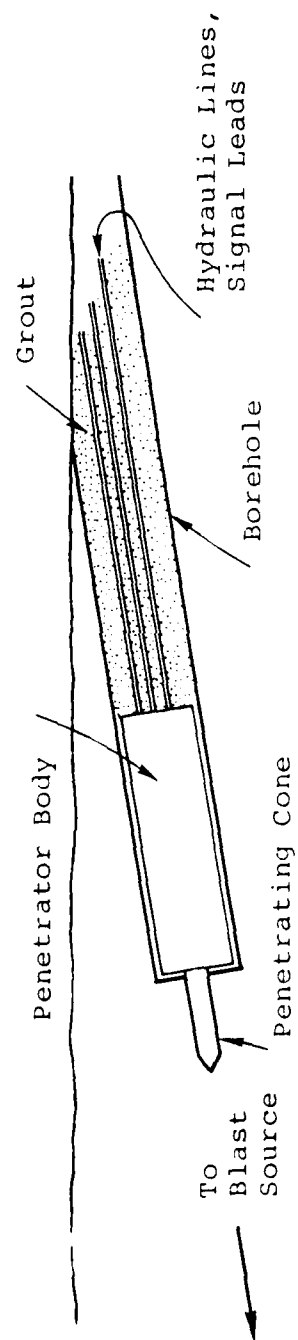
Figure 37. Near Horizontal Downhole Penetrator
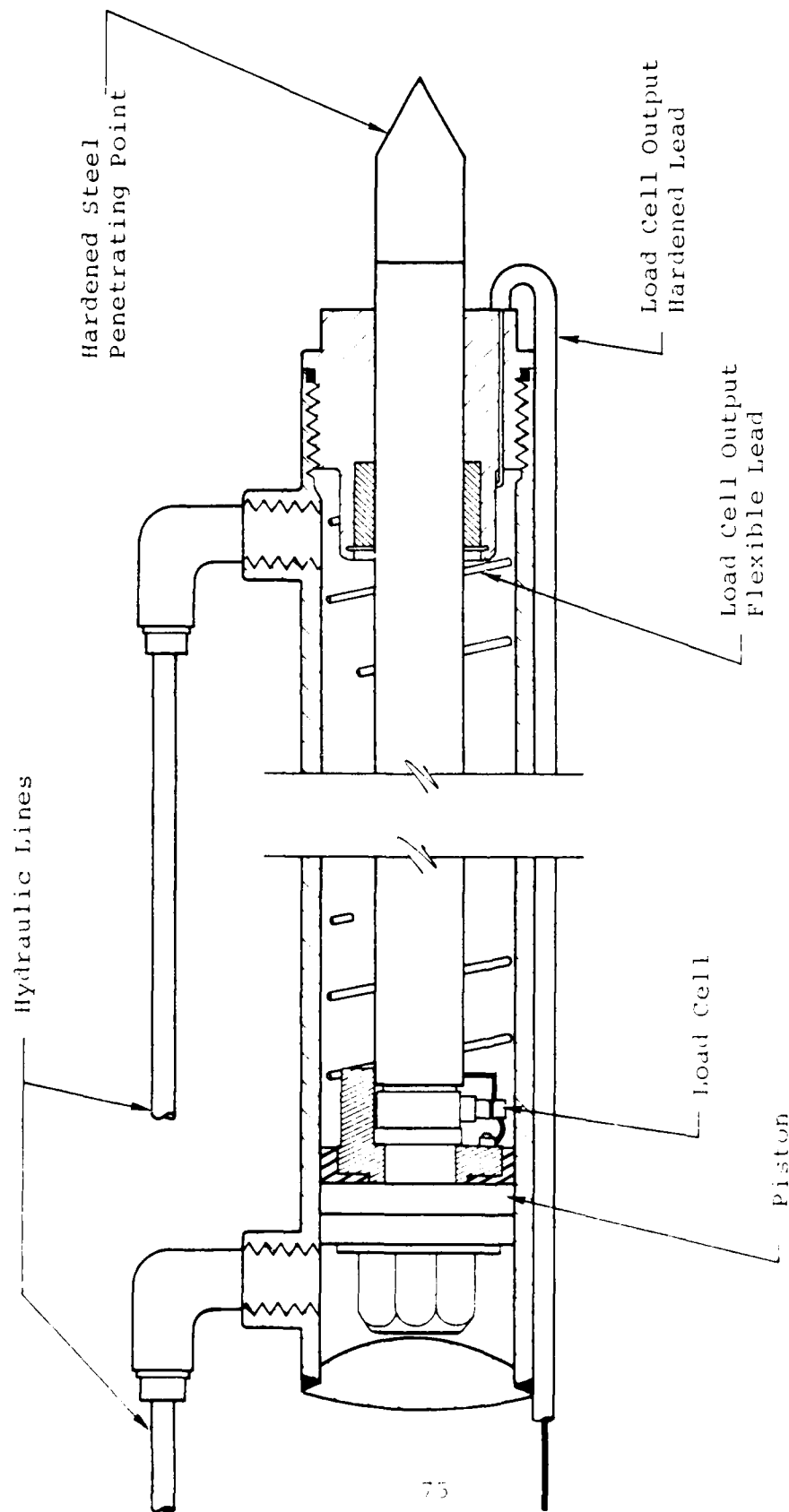
Figure 38. Construction Details for the Soil Strength Gauge-Penetrator. (Unit is a Modified Double Acting Hydraulic Cylinder – Dukes WC-2512, 2 1/2-in Bore, 12-in Stroke, 5000 PSI Shock Load).

Filter

Flow
Controller

4-Way Valve

T   P

B   A

Pressure
By-Pass

Hydraulic
Power Unit

Force
Signal
Recorder

Operating
Station

Hardened
Point

Force Ring

Signal Lead

Down Hole

Hydraulic Cylinder
Modified Dukes
WC-2512
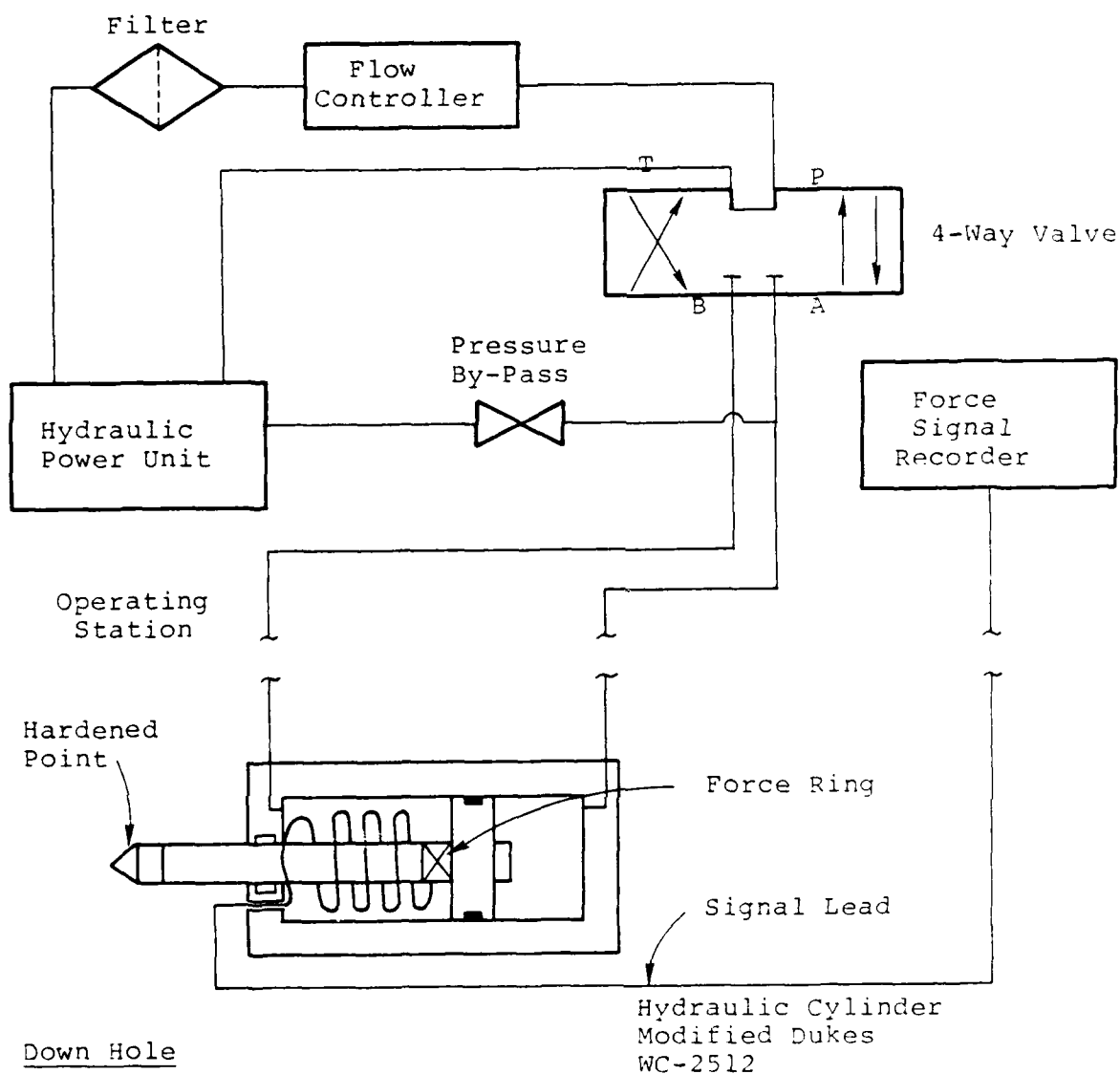
Figure 39. Schematic of Near-Horizonal Downhole Penetrator.

Several experiments were necessary first to determine the proper shock generator design. Additional details concerning the instrumentation for the strength gauge and these tests are given in Appendix B.

4.4 DUAL STRENGTH GROUT TESTS

Variations in soil strength can be achieved by utilizing weak grout mixtures (small quantities of cement mixed with sand). To simplify the formation of the test soil, pits were dug in the existing medium and the grout was poured in. For each pouring, standard test cylinder samples were taken. On the morning of each experiment the respective test sample was broken and the compressive strength of the grout was measured by a testing laboratory.

For the two-strength grout interface penetration experiment, the higher strength grout (1-1/2 sacks of cement per yard of sand) was poured first and allowed to cure. The dividing form was removed and the lower strength grout (one sack per yard of sand) was poured with the soil strength gauge cast in place. The gauge placement and pit dimensions are given in Figure 40.

The grout pit was 68.6 cm wide and the soil strength gauge was positioned centrally across the width. The back-up plate, 30.5 cm square by 1.27 cm thick aluminum, was used to provide additional support for the gauge body.

The higher strength grout in the interface penetration experiment had a compressive strength of 29* bars, the value for the lower strength grout was 1.0 bar. During penetration, the lower strength grout block broke up. Insufficient restraint was provided by the back-up plate and the surrounding soil. This allowed movement to the soil strength gauge body

---

*All these samples were poured on the same day and tested within an interval of three days.

77
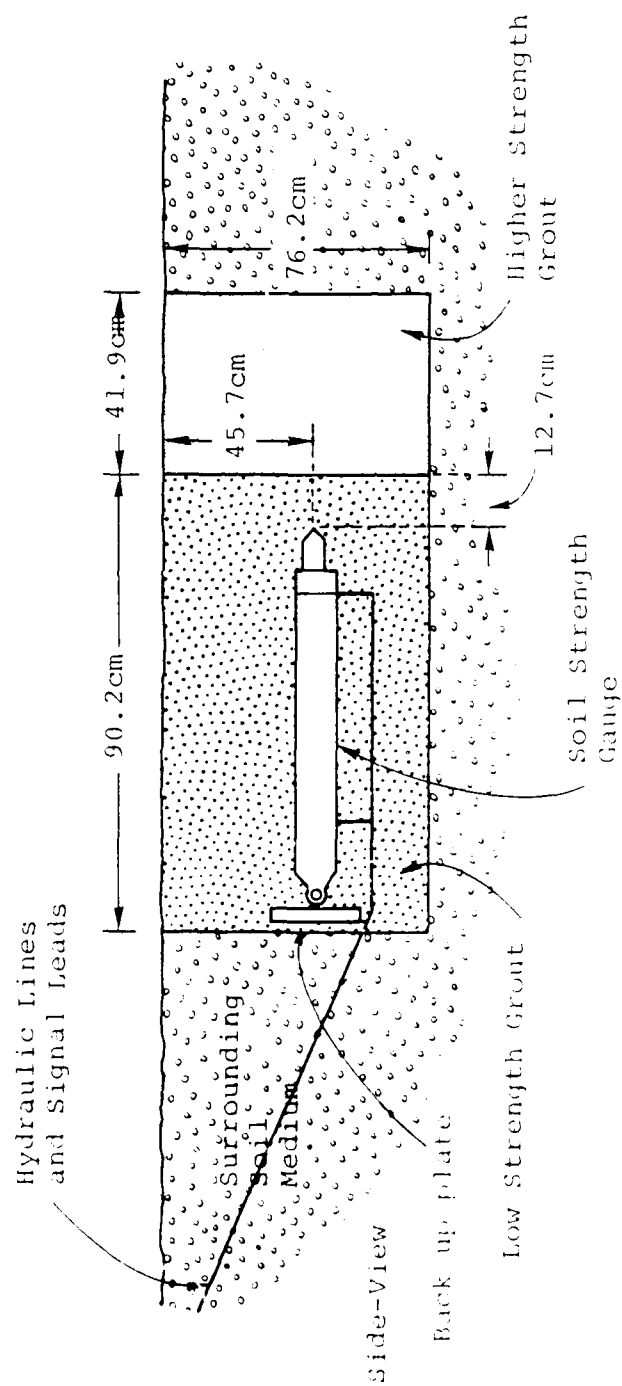
Figure 40. Two-Strength Grout, Interface Penetration Experiment.

Hydraulic Lines and Signal Leads

Surrounding Soil Medium

Side-View

Back up plate

Low Strength Grout

Soil Strength Gauge

Higher Strength Grout

90.2cm

41.9cm

45.7cm

76.2cm

12.7cm

Figure 41. Test setup for the HE shock generator
proof tests.

and the higher strength grout block was only slightly pene-
trated. The effect of the gauge body movement was to prevent
observation of a change in load cell output when the interface
was traversed. The priority of this experiment was low and
therefore it was not repeated.

4.5   TESTS OF THE SHOCK GENERATOR DESIGN

The choice of the proper HE shock generator design was
based on experiments where a stress gauge (PCB model 109A),
cast into a grout pit, was subjected to a stress pulse gener-
ated from a high explosive driver. The orientation and posi-
tioning of the stress gauge, along with the HE shock generator,
is illustrated in Figure 41. The cement and sand mixture was
the same as the higher strength grout in the interface pene-
tration experiment. The stress gauge was positioned centrally
with respect to the 91.4 cm width of the grout pit.

The initial HE shock generator was designed to provide
roughly a 20 MPa (0.2 kbar) peak stress at the gauge location.
The plastic foam (19.2 kg/M^3) was used to reduce pressure and
to increase the pulse duration in the grout. To obtain the
desired peak stress, it was necessary to extrapolate data
taken several years ago at S^3 from pressures of 100 MPa and
higher, reflected at the surface of thick metal plates. Many
conditions of the current setup differ from those of the earlier
experiments making the extrapolation more a guess. For the
first try, 19.2 kg/M^3 density foam of 190 mm thickness was
used. Sheet explosive was cut into strips and cemented to a
6 mm fiberboard in a spaced array to reduce the average density
to one-half the density of the sheet high explosive (DuPont
C-2, 3100 g/m^2 or 2 g/in^2). The resulting charge was
1.55 kg/M^2. The sheet HE was cut in 12.7 mm wide strips
spaced with 12.7 mm gaps. The strips ran in the 91.4 cm width
direction of the grout block. An explosive train (header)

ran along one edge of the grout block and was detonated by a
boosted exploding bridgewire detonator set in the middle of
the header strip. The compressive strength of the grout sample
for this experiment was 29* bars.

The recorded stress pulse due to the HE shock driver
indicated a peak stress of $\sim$ 0.03 kbar and a $\sim$ 200 usec rise
time. This peak stress was an order of magnitude lower than
desired. Inspection of the grout block indicated that it was
undamaged and reusable. A second HE shock generator was con-
structed utilizing a sheet of C-4 explosive, 1.12 m by 1.42 m
(9.856 kg). This increased the mass of explosive by five
times. The compressive strength of the grout was again tested
prior to the experiment and was found to be 29* bars. The
soil strength gauge output indicated that failure of the trans-
ducer had occurred. Examination of the transducer, on removal
from the grout block, revealed that the leads had been sheared.

4.6   SHOCK TESTS OF THE STRENGTH GAUGE

The single strength grout, shocked medium experiments
were attempts at observing a change in soil strength due to
the passage of a stress pulse through the medium. The soil
strength gauge, accelerometer (on the soil strength gauge),
stress gauge and several TOA gauges were cast into a low
strength grout (1-1/4 sacks of cement per yard of sand mix).
An HE shock generator was detonated on the surface of the
grout during penetration by the soil strength gauge. The pit
dimensions and respective locations of the various components
are given in Figures 42, 43, and 44.

Four PZT piezoelectric TOA transducers were used in
the initial experiment to determine the shock velocity in the

_____

*All these samples were poured on the same day and tested
 within an interval of three days.

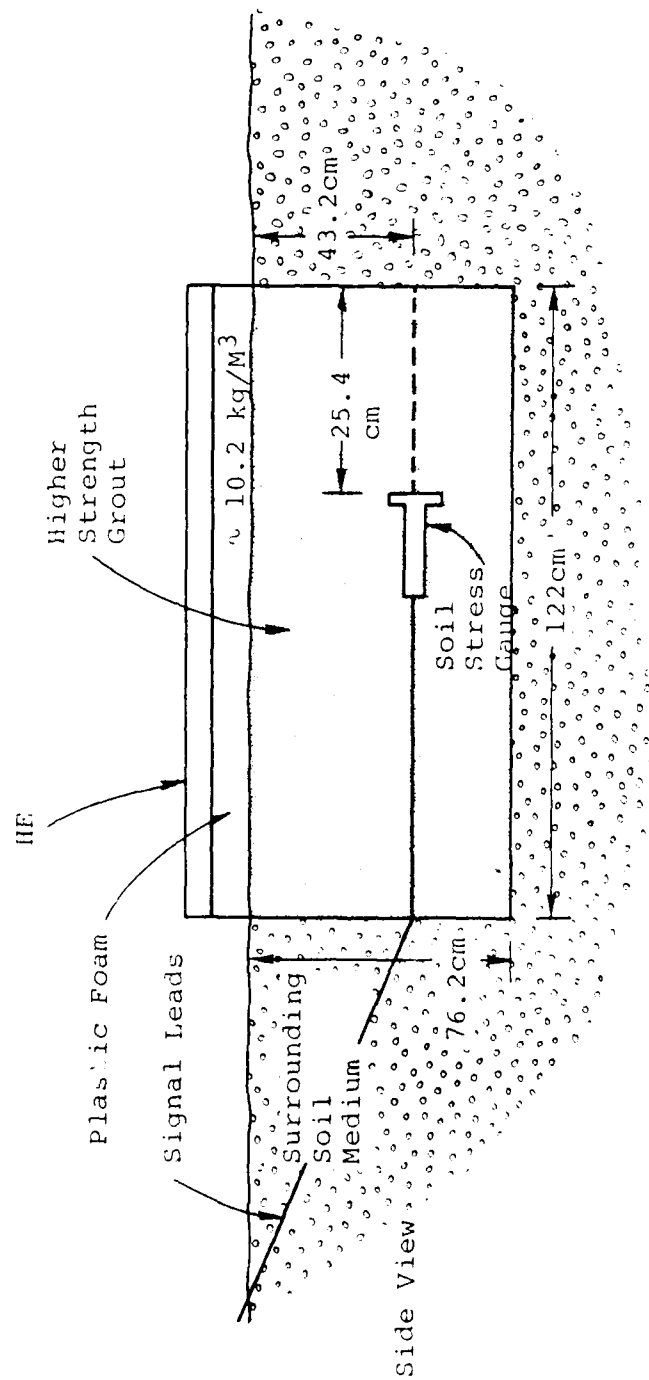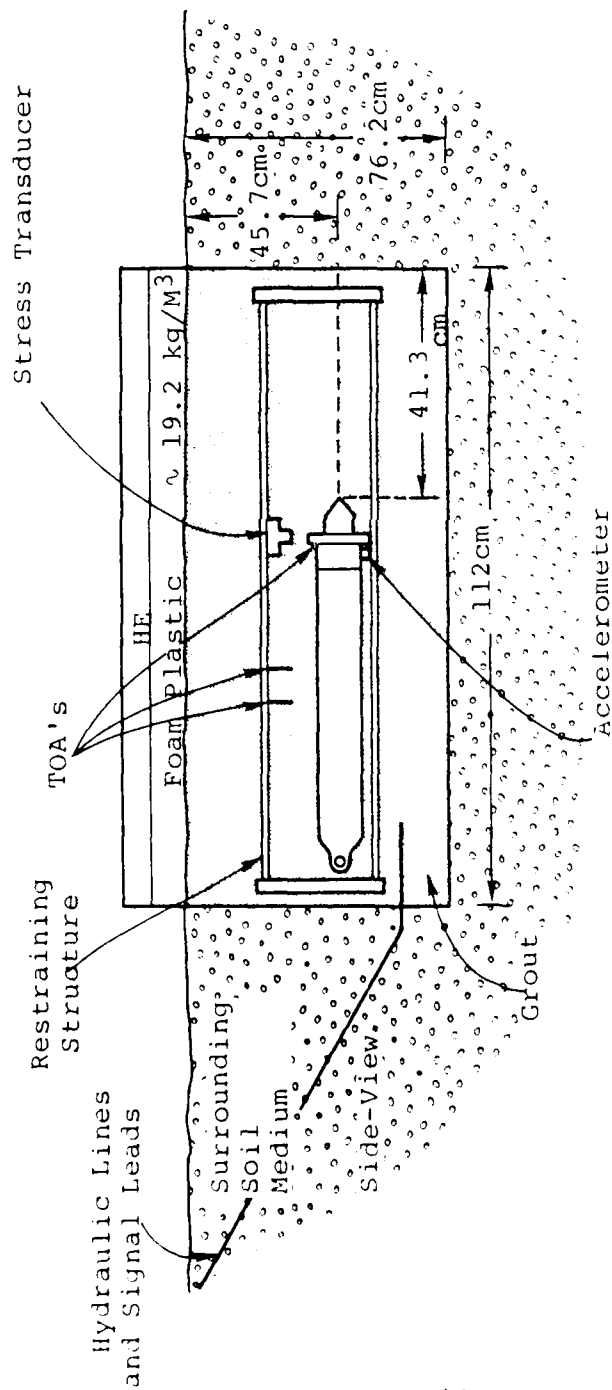Figure 42. The Single Strength Grout Shocked-Medium Experiments.
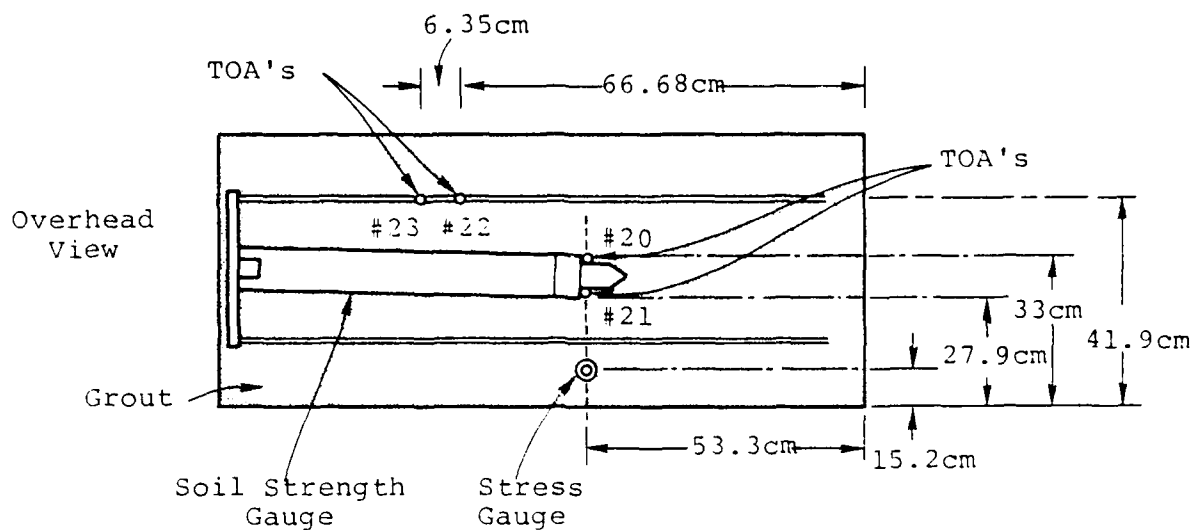
Figure 43. Gauge Placement for Single Strength Grout, Shocked-Medium Experiments.
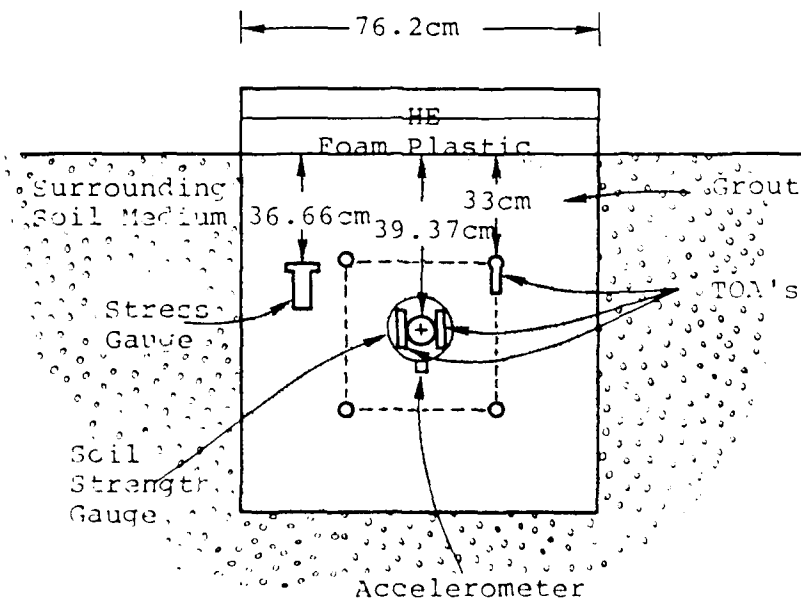
Figure 44. Gauge Placement for Single Strength Grout, Shocked-Medium Experiments. (End view).

grout medium. The acceleration of the soil strength gauge
was measured by an attached PCB (Model 305A02) accelerometer.
The accelerometer and TOA's were positioned with a vertical
orientation.

The restraining structure was designed to prevent grout
block fracture due to gauge body forces and insufficient sup-
port from the surrounding soils. It consisted of four 3/4-10,
122 cm long all-thread rolls attached to the corners of 30.5
cm square by 1.27 cm aluminum plates. The rear of the soil
strength gauge was braced against one of the aluminum plates
with penetration parallel to the all-thread rods.

For the shocked-medium experiments, the HE in the shock
generator was reduced to a sheet of C-2, 0.965 m by 1.32 m
(3.952 kg). This was done since the grout block in the second
HE generator test underwent extensive damage due to the HE
shock.

Just prior to the first shocked-medium experiment, the
compressive strength of the grout was tested and found to be
15.8 bars. Several preliminary checks were made, one of
which involved penetrating the grout a small distance so that
proper operation of the load cell could be verified. The load
cell functioned normally. On initiation of the test sequence,
a wiring error in the HE shock generator prevented its opera-
tion. After the problem was corrected, the test was resumed
by restarting the cone penetrator and then, after a few seconds,
initiating the HE.

The load cell output (Figure 45) indicates that the
stress pulse passed through the grout at nearly the same time
that the gauge reached the end of its travel. The first de-
crease in load cell output occurred at 5.1 seconds after the
start of penetration. It is believed that penetration of
the grout ceased at this point with the level being determined
by residual loads exerted on the cone tip from the surrounding

84
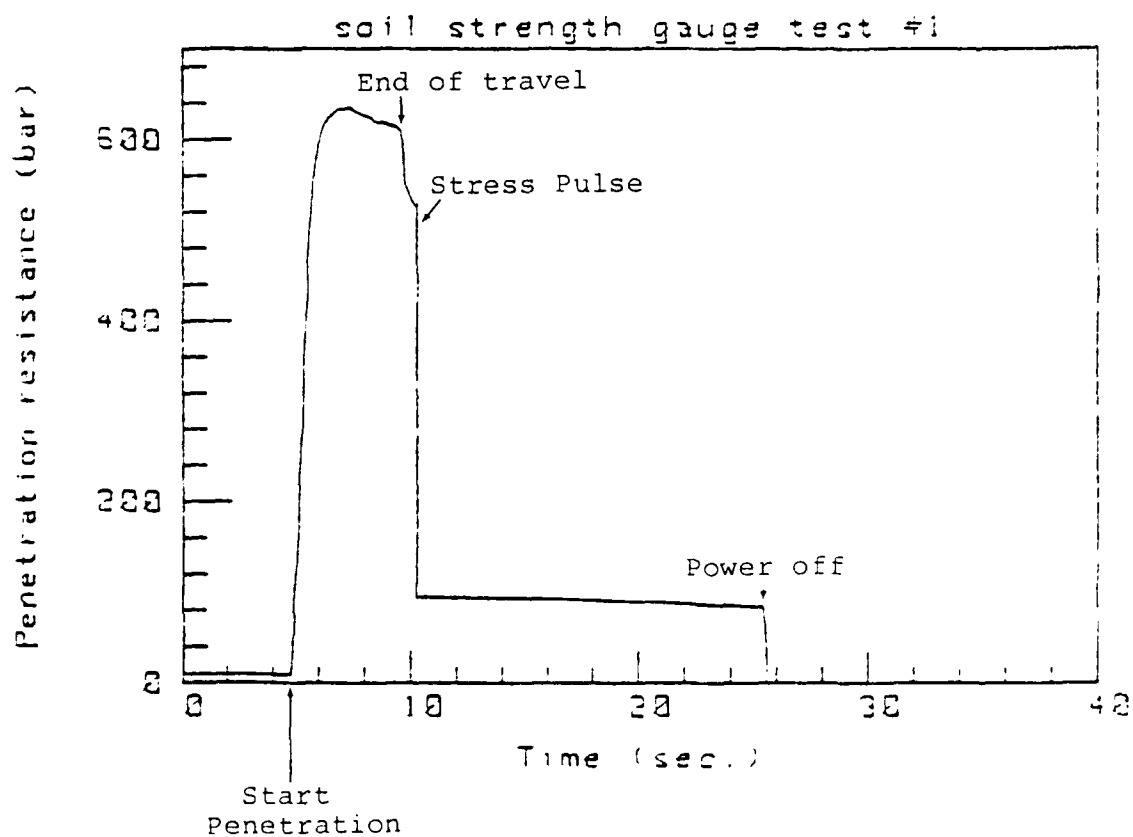
Figure 45. Load Cell Output From the First Shocked Medium Test.

soil. The stress pulse passed through the grout 0.64 seconds later causing a significant decrease in the observed load cell output. The next decrease in the signal occurs when the power to the hydraulic pump was shut off. This allowed a reverse flow of hydraulic fluid relieving the differential pressure across the piston and reducing the signal to zero.

Useful information was nevertheless obtained from the stress gauge (Figure 46) and accelerometer (Figure 47) records. A peak acceleration of 10^3 g's was observed, which is an acceptable value for a cratering event. The corresponding peak stress amounted to about 60 bars, a factor of four low when compared to the desired optimum of 0.25 kbar.

The outputs from the TOA gauges indicated that the shock velocity in the grout was roughly 300 m/sec, which is similar to values obtained for the MIDDLE GUST III event at shallow depths[25].

Since no determination of a change in soil strength was made, the experiment was repeated. The gauges were recast into a low strength grout which had the same mixture ratio as that in the previous experiment, 1-1/4 sacks of cement per yard of mix. The only changes made with respect to the location of gauges were (1) TOA #21 was installed in the same plane and 6.35 cm from the stress gauge, and (2) three additional TOA gauges were installed at the surface of the grout block directly over the major transducer clusters.

On the day of the experiment, a grout sample was tested for compressive strength, the result being 2.76 bars, which is much lower than the 15.8 bars from the previous experiment. Incomplete mixing is the most likely source of the variation, however, the lower compressive strength was not expected to be detrimental to the performance of the experiment.

The preliminary checks of the system were performed, with the test of the soil strength gauge indicating normal

86
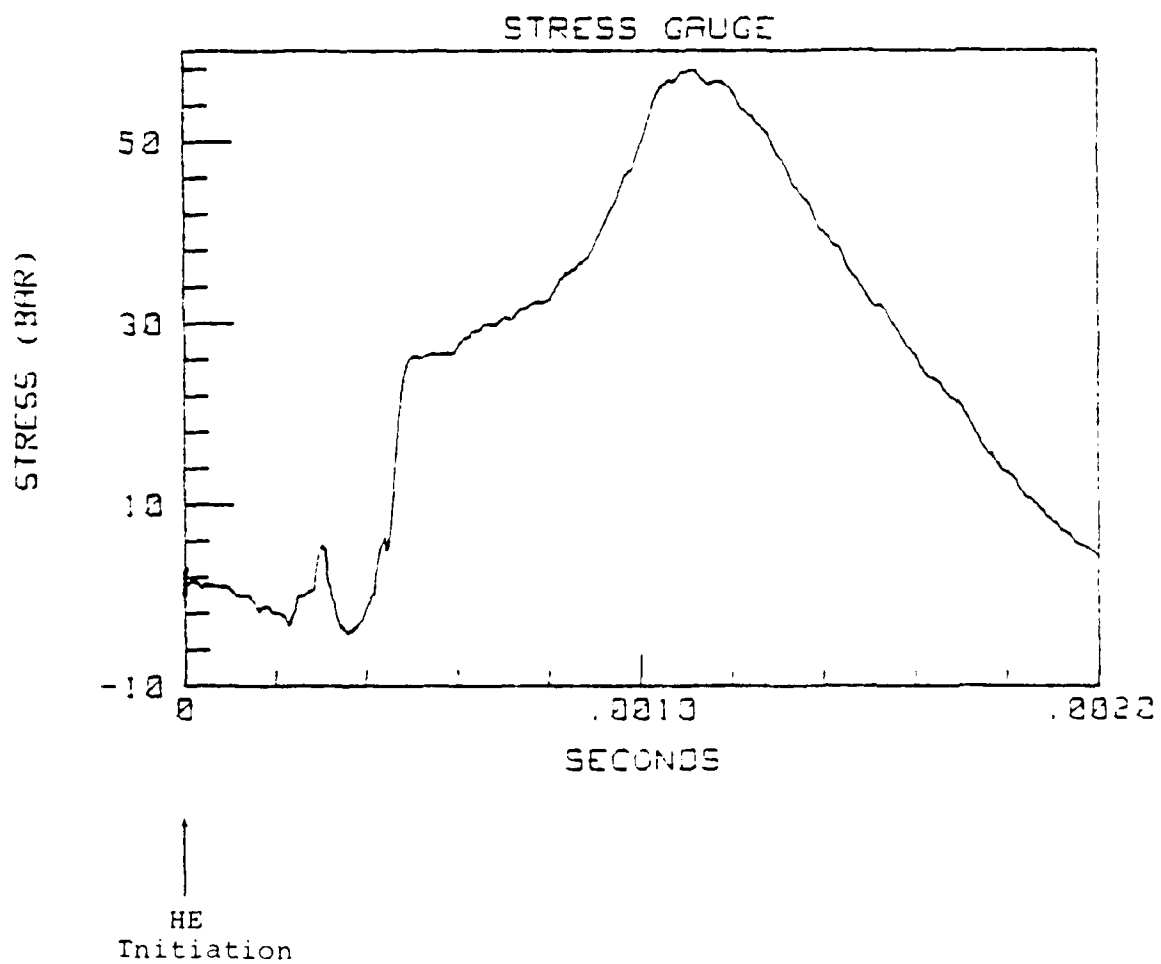
Figure 46. Stress gauge record from the first
shocked medium test.
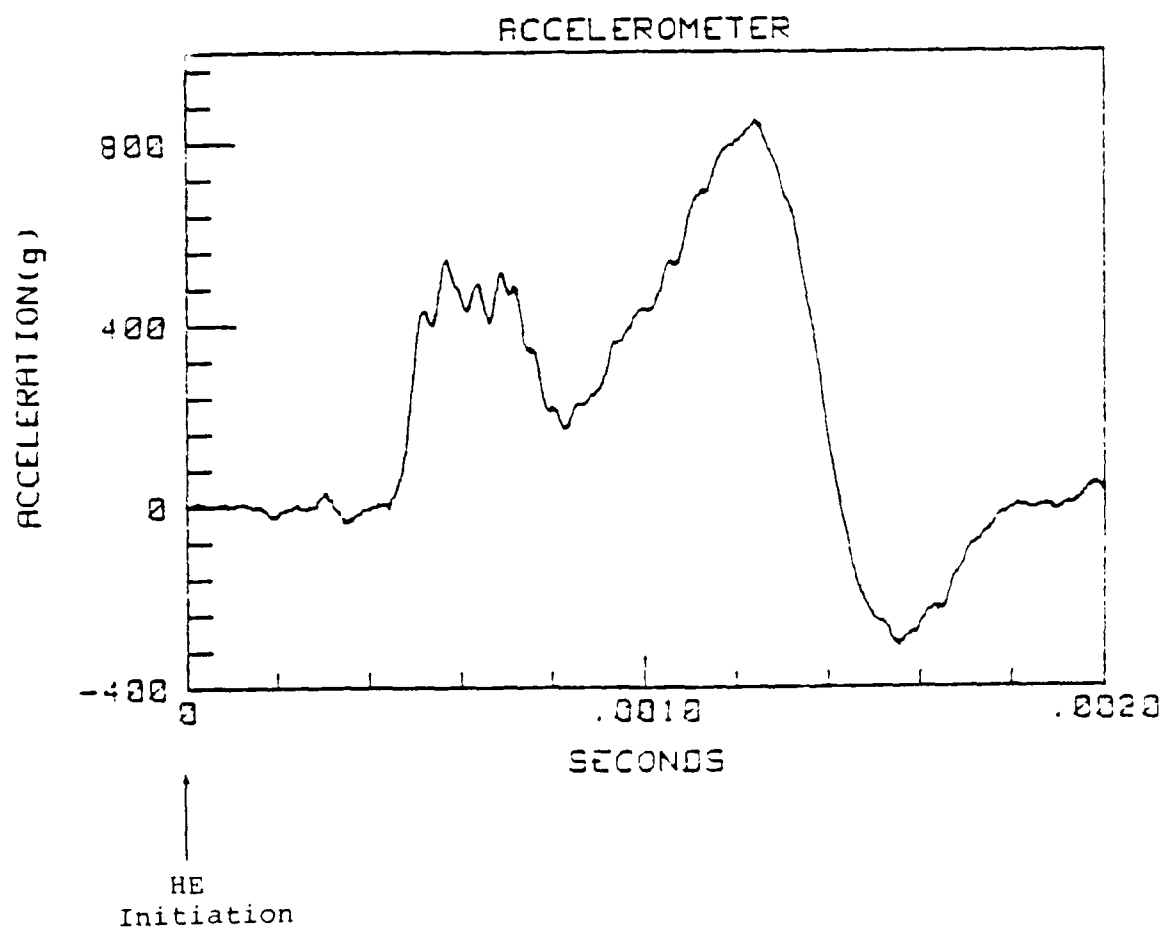
Figure 47. Accelerometer record from the first
shocked medium test.

load cell operation. The experiment was completed with records being obtained from all of the gauges. Examination of the accelerometer output (Figure 48) revealed a peak acceleration of 1000 g's. The peak stress (Figure 49) was 68 bars. These values are very similar to those observed in the previous experiment. The reason for the different wave shapes is not clear.

The TOA gauges show that the average velocity of the shock, in the region of the soil strength gauge, was about 400 m/sec.

From the soil strength gauge output (Figure 50) we note that prior to the start of penetration the gauge registered a positive load. This was a result of the preliminary check of the load cell operation. The penetration was controlled by a four-way valve (Figure 39). The motion was stopped by placing the valve in the neutral position. This stopped the flow of fluid to and from the valve; therefore, a residual load was maintained on the cone tip by the surrounding grout. It represented some static load below the bearing capacity of the soil. Also, the very long time constant of the load cell (~ 2000 sec) prevented any significant decay of the output during the time between the preliminary check and actual experiment (~ 6 min).

Once penetration was started, the output rose smoothly from 104 bars to 146 bars. At this point the stress pulse passed through the soil and the resistance of the soil to penetration dropped to a minimum of ~ 20 bars. A time base expansion around this time region (Figure 51) shows that the drop occurred about 3.52 msec after initiation of the HE driver. The gauge record increased from ~ 20 bars to 77 bars at which time the power to the hydraulic pump was shut off. As discussed earlier, this caused the output to drop to zero.
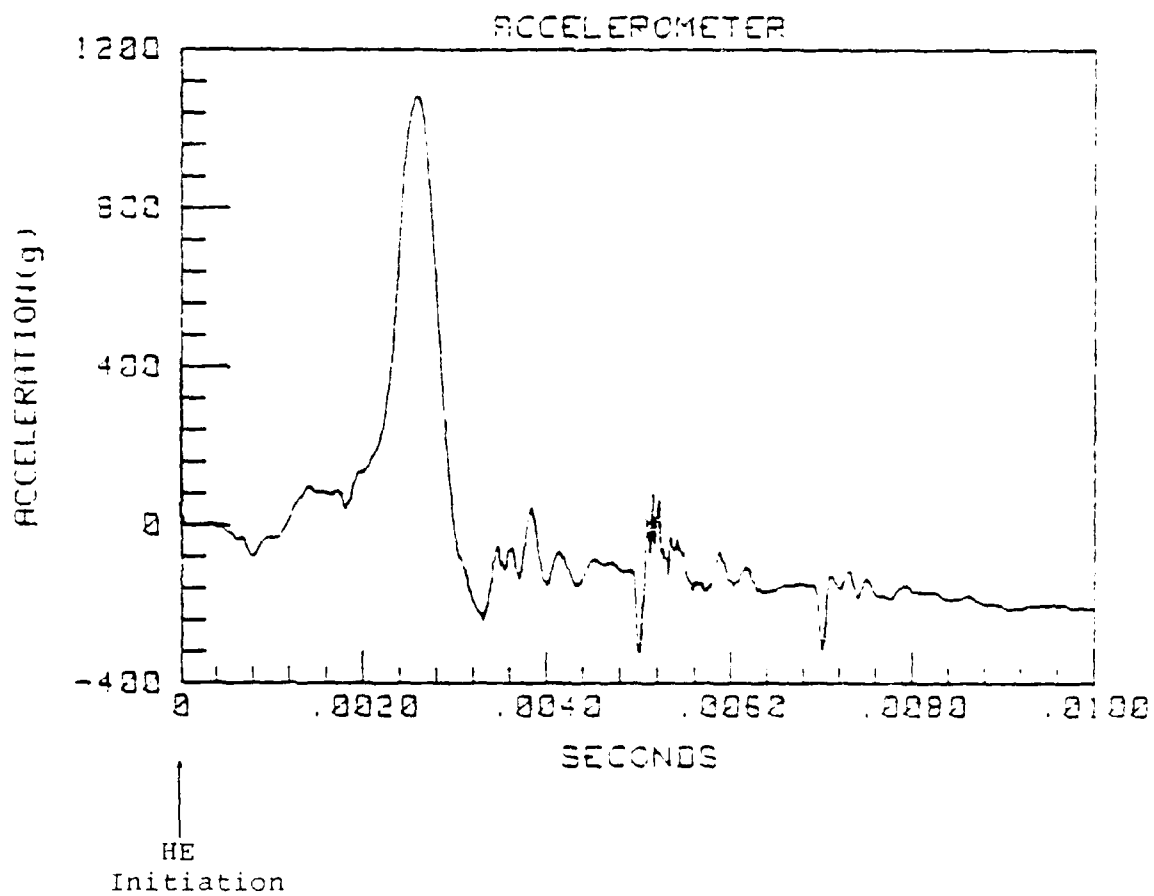
Figure 48. Acceleration record from Test 2.

Figure 49. Stress gauge record from Test 2.

Figure 50. Record of Load Cell Output from the
            Second Shocked Medium Experiment (#2).

Figure 51.   Soil Strength Gauge Output from Test #2
(Expanded time base)

93

4.7 DISCUSSION OF RESULTS

The measured load from the strength gauge's load cell may be related to the soil strength parameters through the bearing capacity equation for shallow footings (Durgunoglu and Mitchell, 1975 [24]),

$$q_f = cN_c\xi_c + \rho g \, B \, N\gamma_q \, \xi_{\gamma q} \tag{14}$$

where

q_f	= the resistance of the soil to penetration (the measured load),
c	= the apparent cohesive strength of the soil,
ρ	= the mass density of the soil,
g	= the acceleration of gravity,
B	= the width of the base of the cone tip,
$N_c, N_{\gamma g}$	= the bearing capacity factors that are functions of the angle of internal friction, depth of penetration, and the lateral earth pressure coefficient, K.
$\xi_c, \xi_{\gamma g}$	= the empirical shape factors for cones.

The lateral earth pressure coefficient, denoted by K, is a multiplicative constant used to describe the lateral stress on an unit volume of soil in terms of the vertical or normal stress. K can be related to the angle of internal friction, ϕ, for some materials.

The Durgunoglu and Mitchell (1975) [24] theory can be used to model the observed soil strength gauge record if the data are expressed as a function of the depth of penetration rather than as a function of time. The rate of penetration* was

$$V = 0.35 \text{ cm/sec.}$$

*This measurement was for the unloaded cone in the lab at the hydraulic fluid flow conditions used for the experiment.

94

Therefore, the resistance to penetration of the grout, q_f, as a function of the depth of penetration is given by

$$\frac{dq_f}{dx} = \frac{1}{V} \cdot \frac{dq_f}{dt} \ . \tag{15}$$

The fully retracted length of the soil strength gauge was $\sim$ 6 cm and the preliminary check resulted in a penetration depth of $\sim$ 3.4 cm; therefore, the initial depth of penetration prior to the experiment was approximately 9.4 cm.

The pre-shock data for the grout consist of the penetration resistance versus depth curve and the measured compressive strength. The concept of a Mohr diagram (Figure 52) provides an additional relation between the apparent cohesive strength c, the compressive strength σ_1 and the angle of internal friction ϕ (Scott, 1963) [26]

$$c = \frac{\sigma_1}{2} \ \frac{1-\sin\phi}{\cos\phi} \tag{16}$$

For normally consolidated soils, Durgunoglu and Mitchell (1975) [24] give the lateral earth pressure coefficient K as a function of the angle of internal friction ϕ,

$$K = 1 - \sin\phi \tag{17}$$

With these assumptions, the pre-shock data then establish values for c, ϕ and K. See Table II.

For the post-shock data, all three of these parameters were varied in an effort to match the measurements. One may not assume that equation (19) holds, because the shock compressed the grout. The lateral earth pressure coefficient may in fact exceed 1 in the shocked medium. One also expects that the shock reduced the apparent cohesive strength by breaking the bonds between the cemented "soil" (grout) particles and by increasing the pore pressure. The parameters listed in the

95
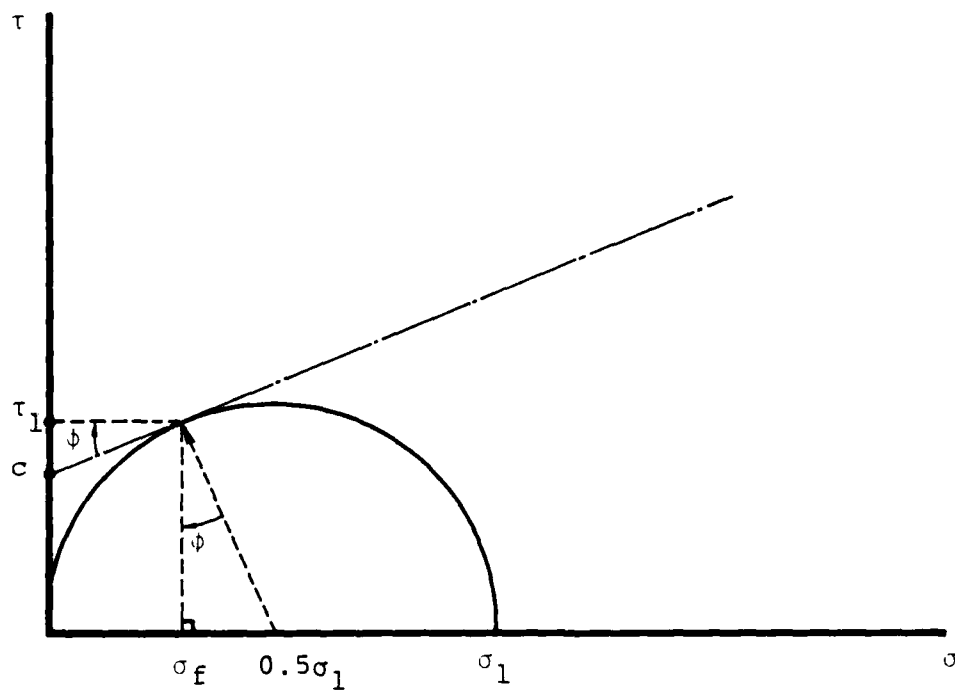
Figure 52. Mohr representation of the compressive
            strength.

σ_1 = The compressive strength

σ_f = The observed total stress at failure normal to the
    failure plane

ϕ = The angle of internal friction

c = The cohesive strength

τ_1 = The shear strength of the soil

TABLE II

THE PRE-SHOCK AND POST-SHOCK PARAMETER VALUES

	Pre-Shock	Post-Shock
ϕ (degrees)	39.2	40.0
Cohesive Strength (bars)	0.65	0.19
K	$1-\sin\phi = 0.37$	1.9

second column of Table II were found to be consistent with the late-time, post-shock data. Figure 53 shows the comparison between the observed data and the pre-shock and post-shock models.

The poor agreement between the model and the data in the immediate post-shock region may be a result of pore pressure effects causing a larger decrease in resistance to penetration than would be predicted, since the model does not take pore pressure into account.

This modeling exercise implies that the reduction in soil strength is due to the breaking of the bonds between the cemented soil particles in addition to pore pressure effects. This calculated decrease in the apparent cohesive strength is by a factor of 3.4. Minor effects are indicated in the apparent angle of internal friction and the lateral earth pressure coefficient. The experiment was, however, sufficient to suggest that the reduced soil strength due to an HE induced shock is a measurable effect, with the developed gauge able to withstand the environment of a simulated cratering event. In order to improve the characterization of the soil response to a stress pulse, the pore water pressure would have to be continuously measured during the experiment. Also, samples of the pre-shock and post-shock soil should be tested by the triaxial shear test to determine late time changes in the cohesive strength and the angle of internal friction.
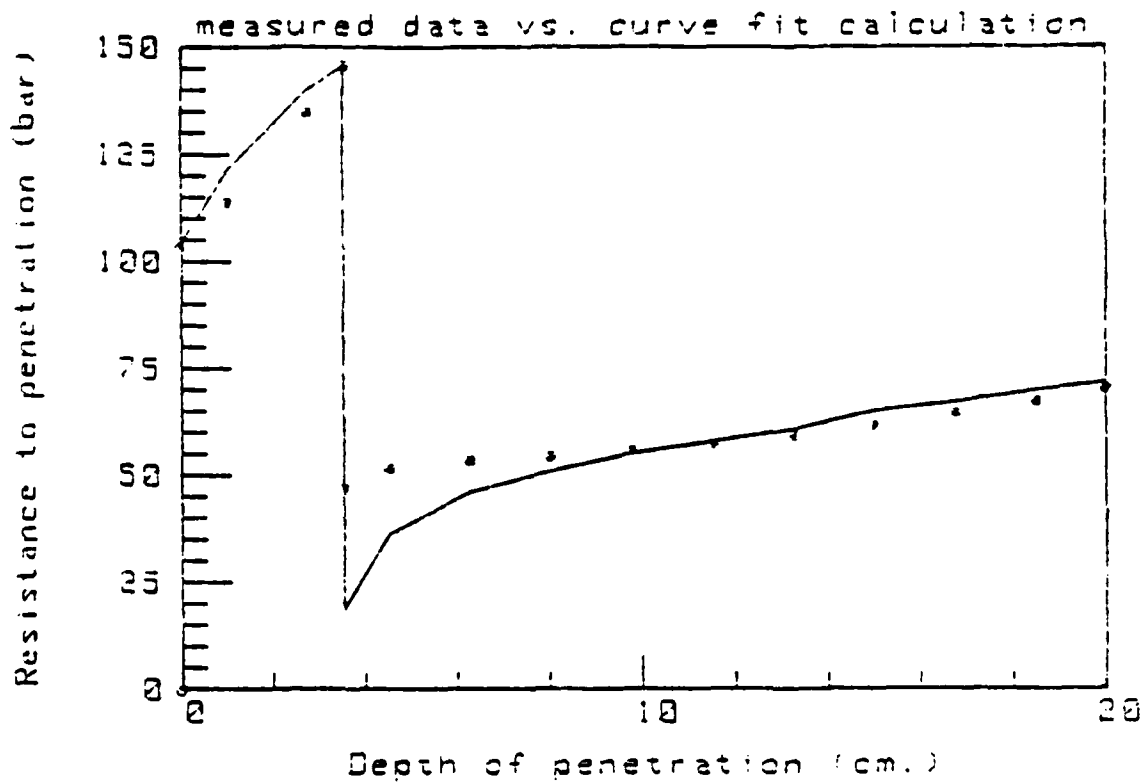
Figure 53. Comparison of Load Cell Output and Curve
Fit Points (The Solid Line is the Load
Cell Output and, ⊙, are the Model Points)

99

V. THERMAL SENSOR

The radiation sensor is a design used by H. Kratz for HYBLA FAIR (1975) [26] and other HE-driven shock applications. The front side of a metallic disk is exposed to a transient thermal source. By measuring the temperature of the back side (which is thermally insulated), one may derive the time history of the radiant energy flux incident on the instrument. See Figure 54. The magnitude of the flux, its duration and the desired time resolution of the instrument determine the material and dimensions of the disk and the choice of a temperature sensor. Two applications are of current interest. For one, a nuclear environment, the peak flux is of order 10^5 cal/(cm^{2}sec) [4×10^9 Watts/m^2] with a few microseconds (or less) risetime and durations up to several hundred microseconds. For the other situation, a thermal radiation simulator, the peak flux is roughly 10^7 Watts/m^2 with durations of about one hundred milliseconds and a desired sub-millisecond time resolution.

5.1 DESIGN CONSIDERATIONS FOR THE THERMAL RADIATION SENSOR

Consider a sheet of thickness a, density ρ (g/cm^3), specific heat capacity C_p (Joules/g°C), thermal conductivity K (Joule/(cm-sec-°C)), and melting temperature T_M. One surface is exposed to a mean flux F (Watts/cm^2) for a time interval Δ. The other surface is thermally insulated and its temperature is measured with, for example, a platinum resistance "thermometer." We wish to resolve changes in the flux on a time scale τ. To ensure a good signal-to-noise ratio, we want the thermometer to "see" a temperature change of δT during the measurement.

If the exposed surface is not to melt, we must have

$$\frac{F\Delta}{\rho C_p a} + \frac{Fa}{3K} < T_M \quad . \tag{18}$$

(Carslaw and Jaeger, 1959) [27]

100

Thermally
Conductive
Sheet

Electrical Insulator
as Needed

Thermometer

Incident

Flux, F

Cable

Non-
Reflective
Coating

Thermal
Insulator

a

b
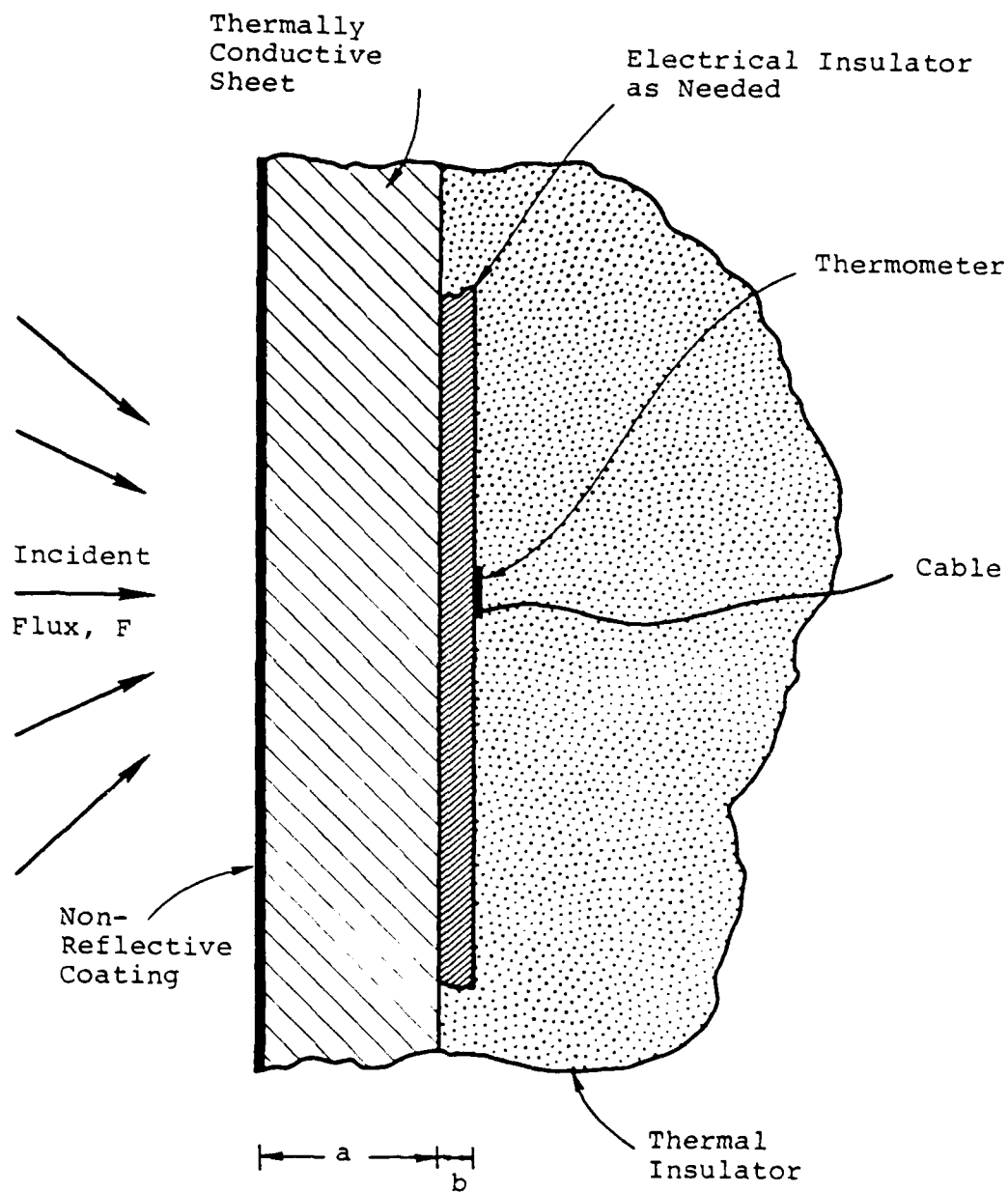
Figure 54. Schematic representation of the thermal
radiation sensor.

To achieve the desired response time, we must have

$$\frac{a^2 \rho C_p}{8K} \sim \tau \quad .$$

(19)

This constraint is based on the risetime of the thermometer signal in response to a delta function pulse of thermal energy deposited on the gauge's surface. The signal requirement means that

$$\frac{F\Delta}{\rho C_p a} - \frac{Fa}{6K} \geq \delta T \quad .$$

(20)

i.e., this is the temperature change at the thermometer due to the flux F. If the response time τ is small compared to the measurement interval Δ, equations ( ) and ( ) reduce to

$$\delta T \leq \frac{F\Delta}{\rho C_p a} < T_M \quad .$$

(21)

For a particular environment of interest (F and Δ) and a particular material, equations ( ) and ( ) yield an allowable range for the thickness a and the corresponding time resolution τ.

Table III lists the properties of several candidate materials along with values for the thickness a and a maximum energy deposition FΔ for response times of 1 μs and 1 ms based on the use of the equations above. The signal requirement, equation ( ), leads to minimum values of FΔ that are a few percent of the maximum values given, depending on the accuracy of the thermometer.

Rinehart and Kratz (1970)[28] describe a gauge of this type using 1 mil (2.5 x 10^{-3} cm) thick aluminum foil to get microsecond response. However, for a nuclear environment of 4 x 10^5 Watts/cm^2 lasting hundreds of microseconds, Table III. shows that no material can meet a FΔ product of 100 J/cm^2. The use of a

102

TABLE III. CANDIDATE MATERIALS FOR A THERMAL RADIATION SENSOR

Material	ρ (g/cm^3)	C_p^* (J/(g°C))	K^* (J/(cms°C))	T_M (°C)	If τ = 1 μs		If τ = 1 ms	
					a (cm)	max FΔ (J/cm^2)	a (cm)	max FΔ (J/cm^2)
Aluminum	2.8	0.95	2.3	660	2.6×10^{-3}	4.6	0.083	150
Copper	8.9	0.40	3.9	1080	3.0×10^{-3}	11.	0.094	360
Tungsten	19.3	0.14	1.7	3370	2.2×10^{-3}	20.	0.071	650
Tungsten-carbide	15.0	0.13	1.0	2870	2.0×10^{-3}	11.	0.064	360
Molybdenum	9.0	0.26	1.3	2620	2.1×10^{-3}	13.	0.067	410
Sapphire	4.0	0.75	0.35	~2000	1.0×10^{-3}	5.8	0.031	180
Silicon carbide	3.2	0.70	0.9	~2600	1.8×10^{-3}	10.	0.057	330
Niobium	8.4	0.27	0.53	2470	1.4×10^{-3}	7.7	0.043	240

*At room temperature, ~20°C.

grey filter (i.e., wavelength independent) in front of the instrument might reduce the actual flux incident on the foil by a factor of ten. Tungsten might also be a worthwhile choice for the gauge. Ultra-thin foils of tungsten are available in thicknesses as low as 7×10^{-4} cm, but because of the possibility of oxidation of the hot tungsten, it would have to be used in an inert atmosphere, in a vacuum, or with a protective over-coating of a suitable material like sapphire.

For the simulation environment of interest, τ is 1 milli-second, F is 10^3 Watts/cm^2, Δ is 0.1 second and FΔ is 100 J/cm^2. Kratz used an 0.1 cm copper disk in a gauge for the HYBLA FAIR event that would serve in this situation. However, the practical problem of electrically isolating the thermometer from the copper was severe. Table III suggests several alternatives. Again, tungsten is attractive and since it can be more highly polished than copper, it might work well. The electrical insulators sapphire and silicon carbide are also possibilities for the disk since they would eliminate the need for a separate insulator under the thermometer element. The extensive use of sapphire in the semiconductor, optical and laser industries has reduced its cost and increased its availability in a variety of shapes. However, the variation of specific heat C_p and thermal conductivity K with temperature for sapphire and silicon carbide is likely to complicate use of these materials; for example, between 0 and 100°C, the specific heat (and thus sensitivity of a gauge) of silicon carbide changes by a factor of 1.35. With a careful calibration of the gauge material, this problem could be handled. The net effect would be that the observed temperature signal would be a nonlinear function of the fluence, FΔ. Reduction of the data would probably require coordinated heat transport code calculations that incorporated a temperature-dependent specific heat.

If the thermometer must be electrically isolated from the gauge disk, several limitations should be met. The insulating layer must be thin enough that its thermal response time is small. Hence, we have

$$b^2 \gtrsim \frac{K'\tau}{\rho'C_p'}$$

where b is the thickness of the layer and K', ρ' and C_p' refer to its properties. This constraint is based on the time variation of temperature on the back surface of a layer subjected to a step function temperature change on its front surface. For example, with sapphire a 1 μs response requires a thickness of about 3×10^{-6} meters and 1 ms response requires b to be under 0.1 mm. If the insulating layer is too thin, dielectric breakdown is possible, especially in an underground test environment; also, parasitic capacitance between the resistance element and the disk could adversely affect the electrical response time of the gauge.

APPENDIX A

CALIBRATION OF BAR GAUGES

Before installation of a bar gauge into its protective housing, it is calibrated to confirm good coupling between the bars and the pressure transducer. The response function of the transducer is usually well known. For example, with X cut quartz, the output is 22 $nC/(kbar\text{-}cm^2)$. However edge effects and poor coupling to the bars can lead to reduced output levels. With properly constructed gauges, the response is typically at least 95% of the nominal value quoted above.

A simple way to test a bar gauge is to mount it vertically and drop a small steel ball onto its end from a known height H. It is easy to photograph the rebound of the sphere to a height H' ($H' \leq H$). If the gauge output voltage V(t) is recorded, then conservation of momentum gives

$$M(\sqrt{2gH} + \sqrt{2gH'}) = AK\int_0^T Vdt \qquad (A1)$$

where M is the mass of the ball, g is the acceleration due to gravity, A is the area of the bar, K is the desired gauge sensitivity in units of pressure per volt and the integral is taken over the duration T of the ball-bar impact. In principle, K can be calculated from the nominal response of X cut quartz, the area of the crystal and the loading capacitor across which the crystal's charge is dumped. Typically, for a steel sphere of mass 2.0 gm (3.9 mm radius) dropped from a height of 130 mm onto a steel bar, the impact duration is less than 30 µs and the rebound height is about 40 mm.

The top trace in Figure A1 shows the signal due to the drop of a 5.56 mm diameter steel bearing from about 180 mm height onto a 6.35 mm diameter steel bar. The actual impact is the pulse at about 0.1 ms. The relatively clean, flat baseline after the pulse is an indication of the good coupling

107
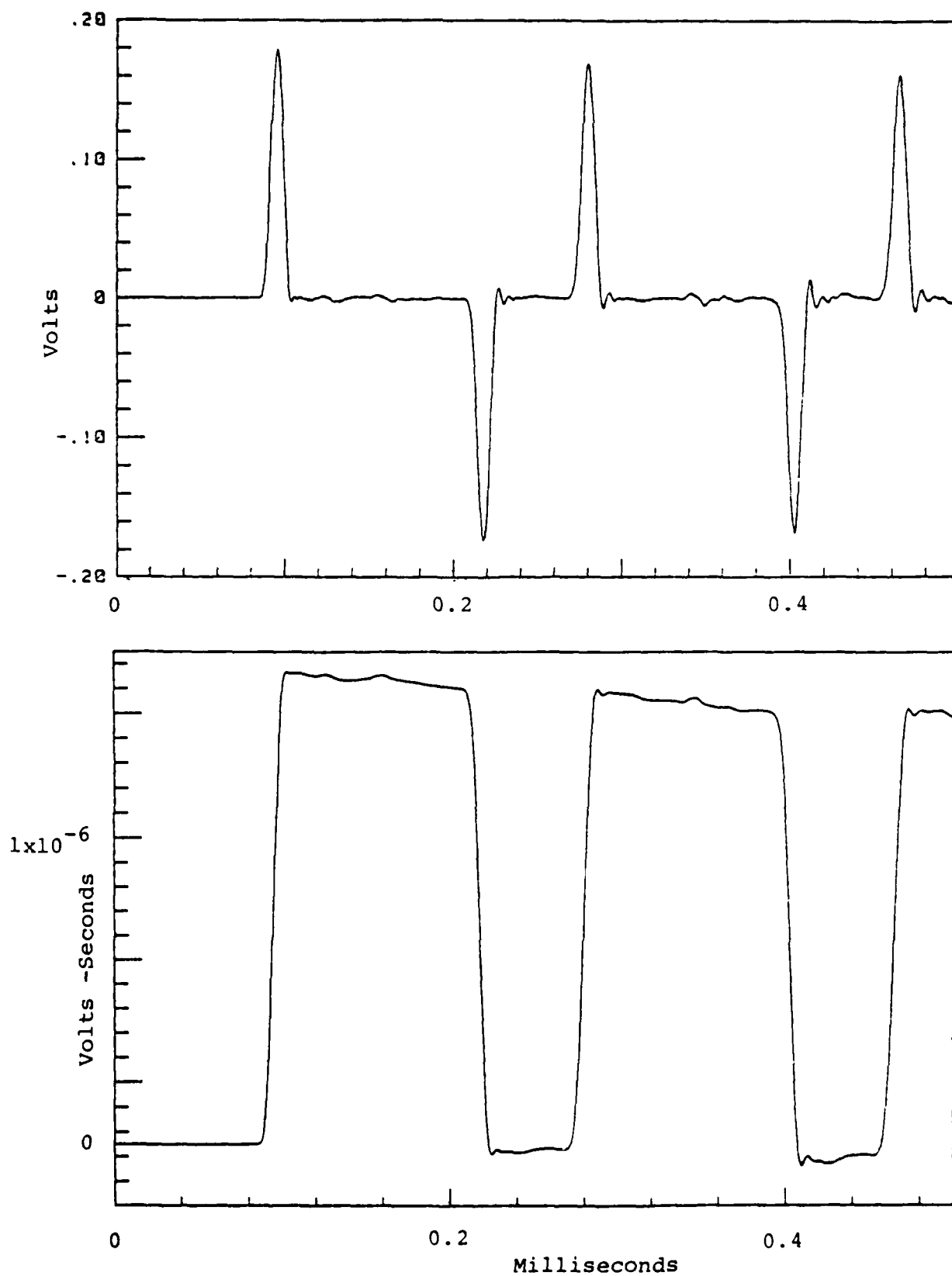
Figure Al.   Example of drop ball test of a bar gauge.   Upper
              trace-Raw signal.   Lower trace - Numerically inte-
              grated signal.   108

of the crystal to the bars and of the absence of constraints along the surface of the bars. The near mirror image quality of the dump bar reflection at about 0.2 ms is also a good indication of gauge performance. Subsequent pulses are due to reflections off the input bar's front end and alternately, dump bar reflections. The bottom trace of Figure A1 is the computer calculated integral of the gauge's signal. The square wave character of the integral is an equivalent measure of the bar's performance.

The Hertz theory of impacting spheres (see Section 2.3) may be used to estimate some details of the actual impact stress pulse. Treating the sensitive end of the bar as part of the surface of a sphere of infinite mass and radius (compared to the drop ball), we find that the peak stress at the ball-bar contact point is

$$\sigma_{max} \sim 2.3 \times 10^8 \; \rho v^{2/5} \tag{A2}$$

where σ_{max} is in Pascals, ρ is the density of the ball and bar (assumed equal, in g/cm^3), v is the impact velocity of the ball in m/s, and the numerical factor assumes a Poisson's ratio of 0.3 and sonic velocity of 5 mm/μs, typical of metals such as steel and aluminum. At the instant of peak stress, the area of contact between the ball and bar is

$$A_{max} \sim 8.5 \times 10^{-3} \; r^2 \; v^{4/5} \tag{A3}$$

where A_{max} is in mm^2 and the ball's radius r is in mm. Finally, the total duration of the collision is

$$\tau \sim 8 \; r/v^{1/5} \tag{A4}$$

where τ is in microseconds. Note that this duration is usually very long compared to the time required for a sound wave to traverse a distance of two sphere diameters, i.e., a time of about 0.8r (μs).

For example, a drop height of 130 mm leads to an impact velocity of 1.60 m/s. With a steel sphere of 3.9 mm radius (2.0 gram mass), the estimated impact duration is 28 μs, the peak stress is 2.2 GPa (22 kbar) and the mean stress over a 6.35 mm diameter bar is 13 MPa (130 bars). In practice, the observed pulse width is about 25 μs and the peak measured stress in the bar is 90 to 110 bars. One usually can see also a small dimple on the end surface of the bar due to the impact. This is consistent with the peak impact stress being large compared to the roughly 4 kbar strength of the steel and with the observed non-elastic rebound of the sphere.

If the duration of the impact is too short, the bar gauge signal will show significant ringing after the impact pulse; see, for example, the paper of Edwards, Davies and Lawrence 1964[29]. This is due to the high frequency content of the impact pulse coupled with the dispersive propagation for compressional waves of sufficiently high frequency. The impact duration should be large compared to the period of the ringing, i.e.,

$$\tau \gg 0.3 \; \ell^{1/3} \; R^{2/3} \; (\mu s) \tag{A5}$$

where ℓ is the length and R is the radius of the input bar (in millimeters); see Coleman (1979)[5].

APPENDIX B

INSTRUMENTATION SUMMARY FOR SOIL STRENGTH GAUGE TESTS

The soil strength gauge was constructed from a standard Dukes model WC 2512 hydraulic cylinder:

> Bore: 6.35 cm
>
> Stroke: 30.5 cm
>
> Diameter of rod: 2.86 cm
>
> Pressure rating: 34.0 MPa (5000 psi)
>
> (6.41 cm^2 cross sectional area)

The load cell was a standard PCB model 203a mounted in the hydraulic cylinder rod. The cell was preloaded to 4450 Newtons compressive force through a beryllium copper mounting stud. This was done to measure any tension exerted on the rod during withdrawal from the soil.

The soil strength gauge with load cell installed was calibrated by applying a known force to the cone tip. The resulting curve was linear with the following value:

> Calibration: 2.87 mv/bar ± 7 percent.

The stress gauge used was a standard PCB model 109A pressure transducer:

> Calibration: 1.086 mv/bar
>
> Range: 0 - 5.5 kbar

in the mounting shown in Figure B1; this configuration was used previously on the HARDPAN I-2B test series and the results were given in Kratz, et al (1978). [1]

111

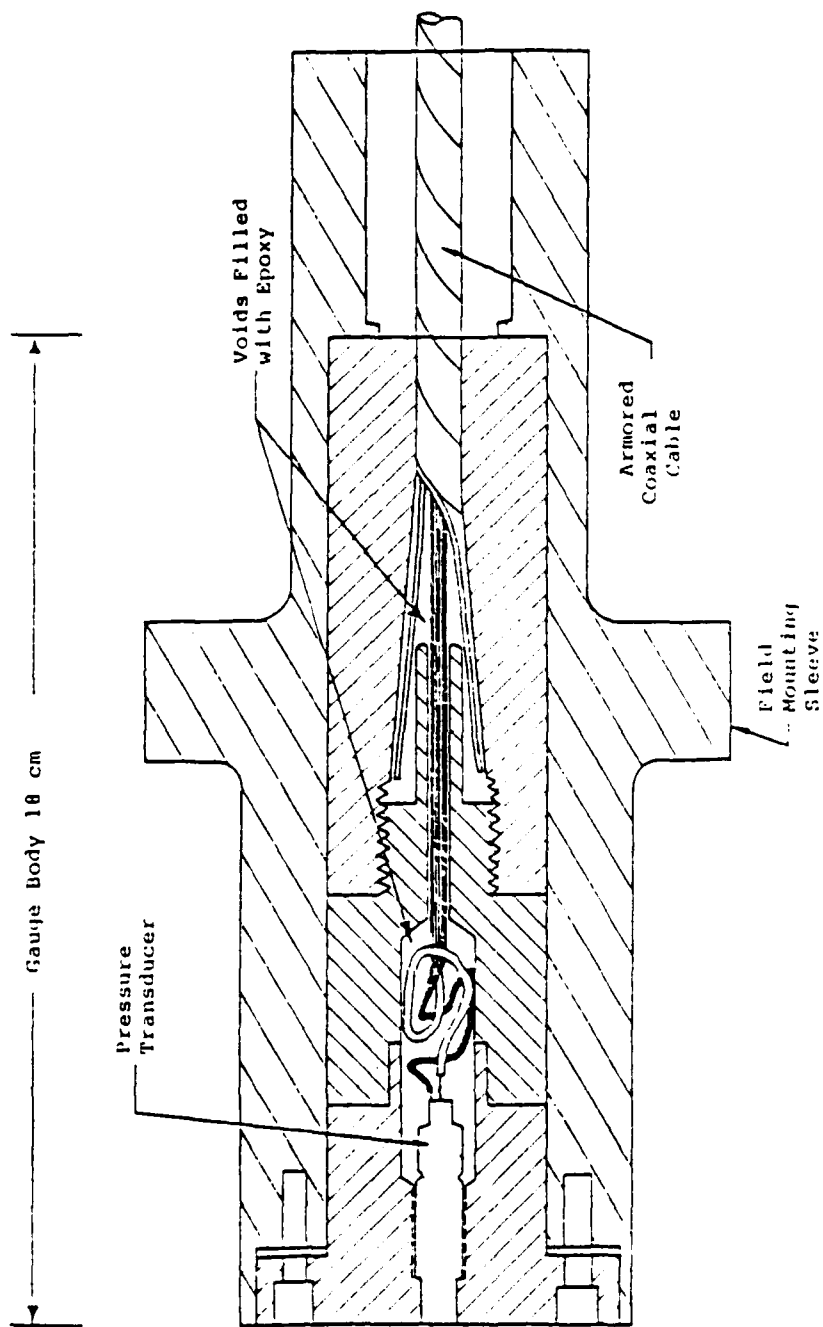Figure B1. Cross-section view of stress gauge.

The accelerometer was mounted into a tapped hole in the front casting of the hydraulic cylinder. It was a PCB model 305A02:

Calibration: 0.0849 mv/g

Resonant frequency: 64.0 kHz

Range: 0 - 50,000 g's

Two types of Time of Arrival (TOA) transducers were used, a shorting pin type and a PZT piezoelectric pressure sensing type.

REFERENCES

1. Kratz, H. R., P. L. Coleman and R. S. Wilson (1978), Development of Airblast and Thermal Radiation Instrumentation, DNA 4594F.

2. Blackstock, A. W., H. R. Kratz and M. B. Feeney (1964), Piezoelectric Gauges for Measuring Rapidly Varing Pressures up to Seven Kilobars," Review of Scientific Instruments 35, 105.

3. Gurney, R. W. (1943), "The initial velocities of fragments from bombs, shells and grenades," BRL Report 405.

4. Kennedy, J. E. (1972), "Explosive output for driving metal," Behavior and Utilization of Explosives in Engineering Design, 12th Annual Symposium ASME, p. 109.

5. Coleman, P. L. (1979), "Modified bar gauges for use in severe airblast measurements," Proceedings of the 25th International Instrumentation Symposium, p. 645.

6. Love, A. E. H. (1944), A Treatise on the Mathematical Theory of Elasticity, Fourth Edition, Dover.

7. Day, Don, Private communication, (1978).

8. Ungar, Eric E. and D. Kent Hatch (1961), "High-damping materials," Product Engineering, April 17, 1961 pp. 44-56.

9. Jones, David I. G. (1972) "Damping treatments for noise and vibration control," Sound and Vibration, July, 1972. pp. 25-31.

10. Ivey, Donald, G., B. A. Mrowca and Eugene Guth (1949), "Propagation of ultrasonic bulk waves in high polymers," Jnl. of Applied Physics 20, 486.

11. Auberger, Michel and John S. Rinehart (1961), "Ultrasonic attenuation of longitudinal waves in plastics," Jnl. of Applied Physics 32, 219.

12. Nakamura, Yosio (1963), "Absorption measurements of ultrasonic waves in plastic sheets," Jnl. of Applied Physics 34, p. 3288.

13. McSkimin, H. J. and P. Andreatch, Jr. (1971), "A water immersion technique for measuring attenuation and phase velocity of longitudinal waves in plastics," Jnl. of the Acoustical Society of America 49, p. 713.

REFERENCES (cont'd)

14.   Folds, D. L. (1972) "Experimental determination of
        ultrasonic wave velocity in plastics, elastomers
        syntactic foam as a function of temperature," Jnl. of
        the Acoustical Society of America 52, p. 426.

15.   Kaiser, J. F. and W. A. Reed (1977) "Data smoothing
        using loss-pass digital filters," Rev. Sci. Instruments
        48, p. 1447.

16.   Wright, J. K. (1961) Shock Tubes, Methuen and Co., Ltd.
        London.

17.   Bryson, A. E. and R. W. F. Gross (1960) "Diffraction of
        strong shocks by cones, cylinders ans spheres," Fluid
        Mechanics 10, #1.

18.   Coleman, P. L., E. S. Gaffney, W. G. Ginn, H. R. Kratz
        and C. F. Petersen (1976) Review and Development of
        Ground Motion and Airblast Instrumentation, DNA 4036F.

19.   Butler, Thomas Daniel, (1966), "Numerical calculations
        of the transient loading of blunt obstacles by shocks
        in air," AIAA Journal 4, p. 460.

20.   Coleman, P. L. and H. R. Kratz (1979), "HYBLA GOLD
        Measurements," POR 7010.

21.   Cherry, J. T., "Computer Calculations of Explosion-
        Produced Craters," Int. J. Rock Mech, Min. Sci., 4,
        1-22 (1967).

22.   Terhune, R., T. F. Stubbs, and J. T. Cherry, "Nuclear
        Cratering on a Digital Computer," Symposium on
        Engineering with Nuclear Explosives, Vol. 1, p. 344
        (1970).

23.   Mitchell, J. K., F. Guzikowski and W. C. B. Villet,
        "The Measurement of Soil Properties In-Situ, Present
        Methods: Their Applicability and Potential," Geoscience
        Research Program of the Lawrence Berkeley Laboratory,
        Report No. LBL-6363, March (1978).

24.   Durgunoglu, H. T., and J. K. Mitchell, "Static Penetra-
        tion Resistance of Soils," I and II, Conf. on In-Situ
        Measurements of Soil Properties, ASCE, 1, (1975).

25.   Middle Gust III Event at Shallow Depth, Proceedings of
        the Mixed Company/Middle Gust Results Meeting 13-15
        March 1973, Vol. 1 and Vol. 2, DNA 3151P1.

REFERENCES (cont'd)

26. Kratz, H. R. (1975) HYBLA FAIR EVENT, Diagnostic
     Measurements, POR 6844.

27. Carslaw, H. S. and J. C. Jaeger (1959) Conduction of
     Heat In Solids, second edition Oxford Press.

28. Rinehart, R. and H. Kratz, (1970) "A Microsecond-Re-
     sponce Bolometer for Measuring Thermal Fluxes in the
     10^5 w/cm^2 Range," ISA Transactions 9, #2 p. 104-112.

29. Edwards, D. H., L. Davies and T. R. Lawrence (1964),
     "The Application of a Piezoelectric Bar Gauge to
     Shock Tube Studies," Jnl. of Scientific Instruments
     41, 609.

DISTRIBUTION LIST

DEPARTMENT OF DEFENSE

Assistant to the Secretary of Defense
Atomic Energy
    ATTN: Executive Assistant

Defense Advanced Rsch Proj Agency
    ATTN: TIO

Defense Intelligence Agency
2 cy ATTN: DB-4N

Defense Nuclear Agency
2 cy ATTN: SPSS
4 cy ATTN: TITL

Defense Technical Information Center
12 cy ATTN: DD

Field Command
Defense Nuclear Agency
    ATTN: FCPR
    ATTN: FCPR, J. Hill

Field Command
Defense Nuclear Agency
Livermore Division
    ATTN: FCPRL

Interservice Nuclear Weapons School
    ATTN: TTV

Joint Strat Tgt Planning Staff
    ATTN: JLA
    ATTN: NRI-STINFO Library

NATO School, SHAPE
    ATTN: U.S. Documents Officer

Undersecretary of Def for Rsch & Engrg
    ATTN: Strategic & Space Systems (OS)

DEPARTMENT OF THE ARMY

Harry Diamond Laboratories
Department of the Army
    ATTN: DELHD-I-TL
    ATTN: DELHD-N-P

U.S. Army Ballistic Research Labs
    ATTN: DRDAR-TSB-S
    ATTN: J. Keefer

U.S. Army Communications Command
    ATTN: Technical Reference Division

U.S. Army Concepts Analysis Agency
    ATTN: MOCA-ADL

U.S. Army Engr Waterways Exper Station
    ATTN: Library
    ATTN: W. Flathau
    ATTN: G. Jackson

DEPARTMENT OF THE ARMY (Continued)

U.S. Army Material & Mechanics Rsch Ctr
    ATTN: Technical Library

U.S. Army Materiel Dev & Readiness Cmd
    ATTN: DRXAM-TL

U.S. Army Missile R & D Command
    ATTN: RSIC

U.S. Army Mobility Equip R & D Cmd
    ATTN: DRDME-WC

U.S. Army Nuclear & Chemical Agency
    ATTN: Library

U.S. Army War College
    ATTN: Library

DEPARTMENT OF THE NAVY

David Taylor Naval Ship R & D Ctr
    ATTN: Code 177, E. Palmer
    ATTN: Code 1740.5, B. Whang
    ATTN: Code L42-3

Naval Construction Battalion Center
    ATTN: Code L08A

Naval Facilities Engineering Command
    ATTN: Code 09M22C

Naval Postgraduate School
    ATTN: Code 0142, Library

Naval Research Laboratory
    ATTN: Code 2627

Naval Sea Systems Command
    ATTN: SEA-09G53

Naval Surface Weapons Center
    ATTN: Tech Library and Info Services Branch

Naval Weapons Center
    ATTN: Code 233

Naval Weapons Evaluation Facility
    ATTN: Code 10

Office of Naval Research
    ATTN: Code 715

Strategic Systems Project Office
Department of the Navy
    ATTN: NSP-43

DEPARTMENT OF THE AIR FORCE

Air Force Institute of Technology
    ATTN: Library

PRECEDING PAGE BLANK-NOT FILMED

DEPARTMENT OF THE AIR FORCE (Continued)

Air Force Weapons Laboratory
Air Force Systems Command
    ATTN: SUL
    ATTN: DYC
    ATTN: DED

Assistant Chief of Staff, Intelligence
Department of the Air Force
    ATTN: INT

Rome Air Development Center
Air Force Systems Command
    ATTN: TSLD

Strategic Air Command
Department of the Air Force
    ATTN: NRI-STINFO Library

DEPARTMENT OF ENERGY

Department of Energy
Albuquerque Operations Office
    ATTN: CTID

Department of Energy
Nevada Operations Office
    ATTN: Mail & Records for Technical Library

OTHER GOVERNMENT AGENCIES

Department of the Interior
Bureau of Mines
    ATTN: Technical Library

Federal Emergency Management Agency
    ATTN: Hazard Eval & Vul Red Div

DEPARTMENT OF ENERGY CONTRACTORS

Lawrence Livermore National Laboratory
    ATTN: Technical Information Dept Library

Sandia National Laboratories
Livermore Laboratory
    ATTN: Library & Security Classification Div

Sandia National Laboratories
    ATTN: 3141

DEPARTMENT OF DEFENSE CONTRACTORS

Aerospace Corp.
    ATTN: Technical Information Services

AVCO Research & Systems Group
    ATTN: Library A830

BDM Corp.
    ATTN: Corporate Library

Boeing Co.
    ATTN: Aerospace Library

Calspan Corp.
    ATTN: Library

University of Denver
    ATTN: Sec Officer for F. Venditti

DEPARTMENT OF DEFENSE CONTRACTORS (Continued)

EG&G Washington Analytical Services Center, Inc.
    ATTN: Library

General Electric Company-TEMPO
    ATTN: DASIAC

IIT Research Institute
    ATTN: Documents Library

Institute for Defense Analyses
    ATTN: Classified Library

Kaman AviDyne
    ATTN: Library

Kaman Sciences Corp.
    ATTN: Library

Lockheed Missiles & Space Co., Inc.
    ATTN: Technical Information Center

Lockheed Missiles & Space Co., Inc.
    ATTN: TIC-Library

Merritt CASES, Inc.
    ATTN: Library

Pacifica Technology
    ATTN: J. Kent

Physics International Co.
    ATTN: Technical Library

R & D Associates
    ATTN: J. Lewis
    ATTN: Technical Information Center
    ATTN: B. Port
    ATTN: P. Haas

Science Applications, Inc.
    ATTN: Technical Library

Stanford Research Institute International
    ATTN: P. DeCarli
    ATTN: D. Keough

Systems, Science & Software, Inc.
    ATTN: Library
    ATTN: P. Coleman
    ATTN: M. Groethe

Terra Tek, Inc.
    ATTN: Library

Tetra Tech. Inc.
    ATTN: Library

TRW Defense & Space Sys Group
    ATTN: Technical Information Center

Weidlinger Assoc., Consulting Engineers
    ATTN: D. Ranlet